2002 NNUN REU Research Accomplishments

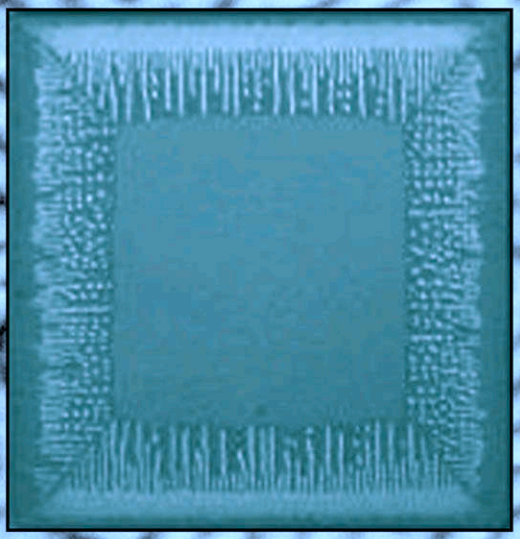

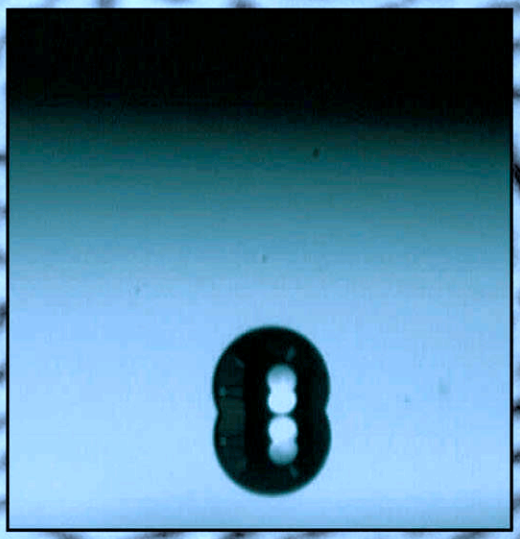

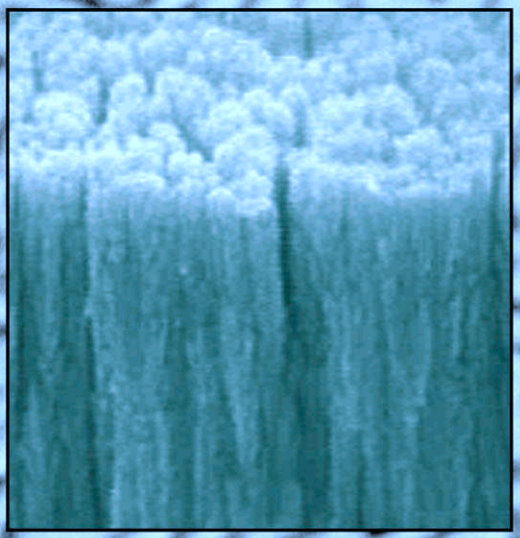

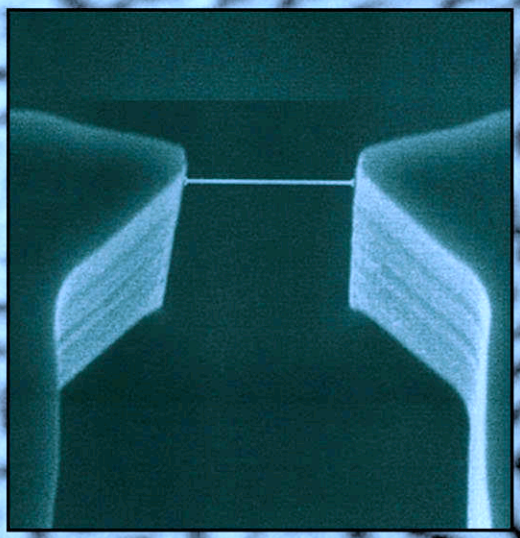

The 2002 NNUN Research Experience for Undergraduates Program

Table of Contents

The 2002 NNUN Research Experience for Undergraduates Program

2002 NNUN REU Interns

INTERN	School Affiliation	Field of Study	NNUN Site	Page #
Mr. Michael Adler	*SUNY Stony Brook*	*Physics / Math*	*UCSB*	*page 82*
Mr. Hani Aldhafari	*Contra Costa College*	*Electrical Engineering*	*UCSB*	*page 84*
Mr. Robert Caldwell	*Boston College*	*Physics*	*SNF*	*page 56*
Ms. Celia See-Ah Chan	*Cornell University*	*BioEngr*	*UCSB*	*page 86*
Ms. Diane Colello	*Rensselaer PolyTech*	*BioMedEngr*	*PSNF*	*page 42*
Ms. Amy Cosnowski	*University of Michigan*	*ChemEngr*	*SNF*	*page 58*
Ms. Janelle Crane	*UC Santa Cruz*	*BioChem*	*UCSB*	*page 88*
Ms. Rose Deeter	*Lehigh University*	*ChemEngr*	*PSNF*	*page 44*
Mr. Mark Elias	*The Ohio State University*	*MSE*	*SNF*	*page 60*
Mr. Robert Gagler	*University of Colorado Boulder*	*Physics/Chem*	*SNF*	*page 62*
Ms. Cara Govednik	*University of Texas at Austin*	*ChemEngr*	*CNF*	*page 6*
Mr. Thomas Graziano	*Cornell University*	*Electrical Engineering*	*UCSB*	*page 90*
Mr. Alexandar Hansen	*Carthage College*	*ACS Chemistry*	*CNF*	*page 8*
Ms. Eszter Horanyi	*University of Colorado Boulder*	*Physics/ChemEngr*	*SNF*	*page 64*
Ms. Karrie Houston	*Howard University*	*ChemEngr*	*Howard*	*page 32*
Mr. Scott Howard	*University of Notre Dame*	*Electrical Engineering*	*SNF*	*page 66*
Ms. Gizaida Irizarry	*University of PR Mayaguez*	*MechEngr*	*CNF*	*page 10*
Mr. Jacob Jordan	*Vanderbilt University*	*ChemEngr*	*CNF*	*page 12*
Mr. Michael Krause	*Wayne State University*	*Electrical Engineering*	*CNF*	*page 14*
Mr. Chun-Cheng Lin	*University of Southern California*	*Electrical Engineering*	*CNF*	*page 16*
Mr. John Liu	*UC Irvine*	*CompEngr*	*SNF*	*page 68*
Ms. Kelly McGroddy	*University of Pennsylvania*	*MSE*	*UCSB*	*page 92*
Mr. Curtis Mead	*University of Minnesota*	*Electrical Engineering*	*SNF*	*page 70*
Ms. Schuyler Mudge	*University of Washington*	*Physics*	*SNF*	*page 72*
Mr. Omar Negrete	*University of New Mexico*	*Electrical Engineering*	*CNF*	*page 18*
Ms. Trang Nguyen	*San Jose State University*	*Electrical Engineering*	*CNF*	*page 20*
Ms. Jennifer Park	*University of Colorado Boulder*	*ChemEngr*	*UCSB*	*page 94*
Mr. Matthew Pickett	*The Pennsylvania State University*	*EngrSci*	*PSNF*	*page 46*
Mr. Diego Rey	*UC Santa Barbara*	*Electrical Engineering*	*CNF*	*page 22*
Mr. Hector Luis Rodriguez	*University of PR Mayaguez*	*ChemEngr*	*PSNF*	*page 48*
Ms. Nicole Schilling	*Corning Community College*	*Physics*	*CNF*	*page 24*
Mr. Michael Shearn II	*Southern Methodist University*	*EE/Math/Physics*	*SNF*	*page 74*
Mr. Jason Smeltz	*Penn State Capital Campus*	*Electrical Engineering*	*Howard*	*page 34*
Ms. Mahmooda Sultana	*University of Southern California*	*ChemEngr*	*SNF*	*page 76*
Ms. Mamie Thant	*Harvard University*	*Chemistry*	*PSNF*	*page 50*
Ms. Veronica Valeriano	*University of Washington*	*Electrical Engineering*	*Howard*	*page 36*
Mr. Kenneth Vampola	*UC Santa Barbara*	*Electrical Engineering*	*CNF*	*page 26*
Ms. Kristen Van Horn	*Harvey Mudd College*	*Engr*	*UCSB*	*page 96*
Mr. William Whitaker	*Bakersfield College/UC Berkley*	*Computer Engr*	*Howard*	*page 38*
Ms. Kelly Wright	*Texas A&M University*	*BioMedical Engr*	*PSNF*	*page 52*
Ms. Sara Yazdi	*University of MA Amherst*	*ChemEngr*	*CNF*	*page 28*
Ms. Laura Zager	*Swarthmore College*	*Engr/Math*	*SNF*	*page 78*

The 2002 NNUN Research Experience for Undergraduates Program

Introduction

The 2002 NNUN REU Interns at the August network-wide convocation, Cornell University, Ithaca, NY

Welcome to the 2002 Research Accomplishments for the National Nanofabrication Users Network's Research Experience for Undergraduate Program.

Providing a focused experimental research experience in nanotechnology and its basic subjects in a 10 week period is a challenging task; this report demonstrates that with effort from staff, faculty, graduate students, and the participating students, not only can it be successfully achieved, but also it can lead to significant accomplishments by students who have just started on the path of technical education.

The NNUN partnership, through our complementary strengths, cross-fertilization, multi-site education, and use of each other's resources, provides exciting projects and the means to achieve them in a reasonable time. Each student in the NNUN REU completes an independent research project with strong technical support and faculty supervision, undergoes strong hands-on training and education (also available as streaming video at http://www.cnf.cornell.edu/nanocourses/nanocourse.html), and participates in a convocation at individual sites and at a common site to present their research efforts.

The focus on advanced research and knowledge, the strong mentoring and support, the strong exposure to a professional research environment, the strong expectations built into the research and presentations at convocations, the exposure to a wider variety of research conducted by peers and other users in diverse disciplines of science and engineering within the unifying facilities, and the strong scientific and social interactions across the network have been critical to the program's success. This year's participants also saw increased cross-site interactions through video-conferences and presentations, and hands-on experimentation.

I wish the participants the best wishes for future technical careers; NNUN hopes to see them build on this summer's experience. And my thanks to the staff, the graduate student mentors, and the faculty for their participation and involvement.

Sandip Tiwari, Director, NNUN

The NNUN REU Program

is made possible by National Science Foundation Grant # 9987915 and the following NNUN Partners and Corporate Sponsors

http://www.nnun.org/

Network Partners:

Cornell Nanofabrication Facility
Prof. Sandip Tiwari, Director
Cornell University
Knight Laboratory, CNF
Ithaca, New York 14853-5403
Voice: (607) 255-2329
Fax: (607) 255-8601
http://www.cnf.cornell.edu/

Materials Science Research Center for Excellence
Prof. Gary Harris, Director
Howard University School of Engineering
2300 Sixth St, NW
Washington, D.C. 20059
Voice: (202) 806-6618
Fax: (202) 806-5367
http://www.msrce.howard.edu/~nanonet/NNUN.HTM

Penn State Nanofabrication Facility
Stephen J. Fonash, Director
Kunkle Chair Professor of Engineering Sciences
189 Materials Research Institute
The Pennsylvania State University
University Park, PA 16802
Voice: (814) 865-4931
Fax: (814) 865-3018
http://www.nanofab.psu.edu/

Stanford Nanofabrication Facility
Yoshio Nishi, Director
Stanford University
Center for Integrated Systems, Room 103
Stanford, CA 94305-4070
Voice: 650-723-9508
FAX: 650-725-0991
http://snf.stanford.edu/

UCSB Nanofabrication Facility
Prof. Mark Rodwell, Director
Department of Electrical and Computer Engineering
University of California, Santa Barbara
Santa Barbara, CA 93106-9560
Voice: (805) 893-8174
Fax: (805) 893-3262
http://www.nanotech.ucsb.edu/

REU Program Corporate Sponsors:

Advanced Micro Devices
Agilent Technologies
AMP (Lytel)
Analog Devices
Applied Materials
Canon
Hewlett-Packard Company
Hitachi, Ltd
IBM Corporation
Infineon
Intel Corporation
Matsushita
National Semiconductor Corporation
Panasonic
Philips
Robert Bosch Corp.
Taiwan Semiconductor Manufacturing Company
Tektronix
Texas Instruments, Incorporated
Toshiba
Varian Semiconductor Equipment Associates
Xerox Incorporated

Cover Graphics:

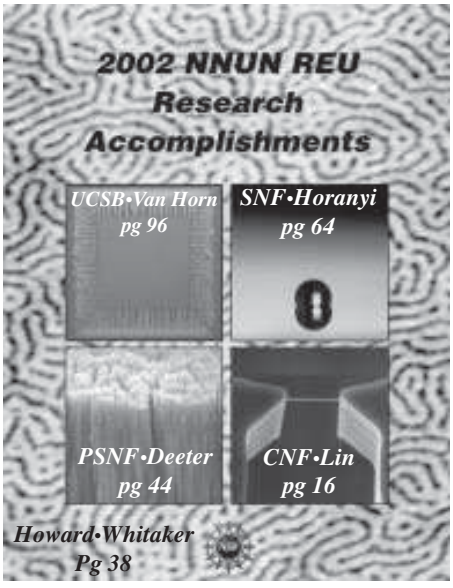

Cornell Nanofabrication Facility

Cornell University, Ithaca, NY

http://www.cnf.cornell.edu

2002 CNF REU Interns

NNUN REU Intern	School Affiliation	Principal Investigator
From Left to Right:		
Ms. Sara Yazdi	University of MA Amherst	Garry Bordonaro
Ms. Gizaida Irizarry	University of PR Mayaguez	Mandy Esch
Mr. Diego Rey	UC Santa Barbara	Michael Spencer
Mr. Alexandar Hansen	Carthage College	Christopher Ober
Ms. Trang Nguyen	San Jose State University	George Malliaras
Ms. Nicole Schilling	Corning Community College	Vincent Genova
Mr. Jacob Jordan	Vanderbilt University	Carl Batt
Mr. Chun-Cheng Lin	University of Southern California	James Engstrom
Ms. Cara Govednik	University of Texas at Austin	John Marohn
Mr. Omar Negrete	University of New Mexico	Alan Bleier
Mr. Kenneth Vampola	UC Santa Barbara	Edwin Kan
Mr. Michael Krause	Wayne State University	Dieter Ast
Dr. Sandip Tiwari	Cornell Nanofabrication Facility	NNUN Director

Fabrication of Xylophone Resonators

Cara Govednik, Chemical Engineering, The University of Texas at Austin

John Marohn, Neil Jenkins, Chemistry, Cornell University

cgovednik@hotmail.com, jam99@cornell.edu

Abstract:

We report on an initial attempt to fabricate xylophone resonators for use as force detectors in Magnetic Resonance Force Microscopy (MRFM). Xylophone resonators are expected to have higher quality factors than cantilevers and are also ideal for use in monolayer NMR experiments.

So far, we have attempted to fabricate xylophone resonators 300-1000 μm wide and 800-1500 μm long. We have found the xylophones to be too delicate to withstand the final step of the fabrication process. Alternative methods must be tested to successfully fabricate these xylophone resonators.

Introduction:

In MRFM [1], magnetic resonance is detected as a gradient-dipole force between the nuclear or electronic spins in a sample and a small magnetic particle near the sample using a nanofabricated oscillator. Xylophone resonators are being developed as a possible alternative to cantilevers, which are the predominant oscillators used in MRFM. Xylophone resonators are attached by four struts, which are made as narrow as possible to reduce the damping of the oscillator. Reduced damping gives higher quality factors and therefore allows a smaller force to be detected. Low spring constants, low temperatures and long, thin, narrow dimensions also obtain the smallest minimum detectable force.

The other key reason for the fabrication of xylophone resonators is the interest in monolayer samples in NMR experiments. In monolayer NMR experiments, the sample is deposited directly onto the oscillator. Xylophones are ideal for these experiments because they are larger in area than the cantilevers currently in use and the sample can be placed directly onto the surface of the xylophone by evaporation.

Fabrication of Xylophone Resonators:

The procedure begins by patterning a silicon-on-insulator (SOI) wafer with xylophone resonators, ranging from 300 to 1000 μm in width and 800 to 1500 μm in length. The xylophones are exposed using contact alignment and transferred to the top 340 nm layer of silicon using a dry SF_6 plasma etch. The frontside process successfully etched the 2 μm wide and 5 μm long struts which were placed at 22.4% of the xylophone length from each edge. To protect the front side etch during the rest of the procedure, a protective oxide layer, about 1 μm thick, is deposited over the wafer.

The backside process is similar to the patterning of the front side of the wafer. The backside consists of large rectangular flop-holes underneath the xylophones which provide space for the xylophones to oscillate. The backside layer consists of a 525 μm thick layer of silicon, which is etched down to the 400 nm oxide layer using a Bosch etch. The Bosch process is a dry etch which alternates between a polymer deposition and a plasma etch, allowing high aspect ratio features to be etched with approximately vertical sidewalls and a high selectivity for silicon with an etch rate of about 2 μm per minute. Finally, the xylophones are released immediately after the backside etch is complete by removing the oxide layers through wet etching in a Buffered Oxide Etch (BOE), 6:1 HF: NH_4F.

Results:

There were several problems that occurred during this fabrication procedure. First, the etch rate on the backside of the wafer was not consistent. The etch depths of the flop-holes on the same wafer could range

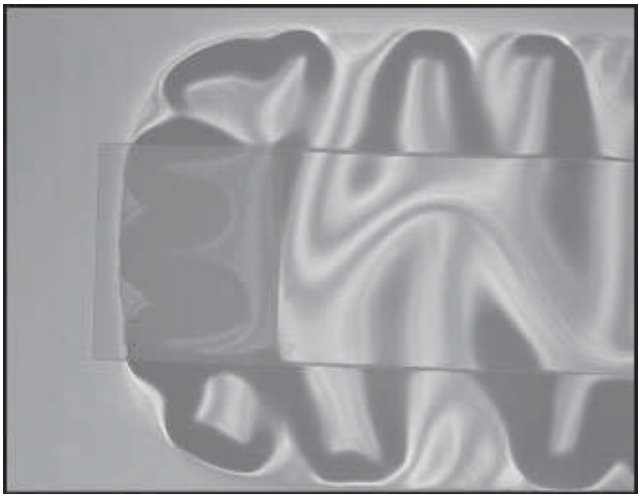

Figure 1: Over-etched xylophone resonator.

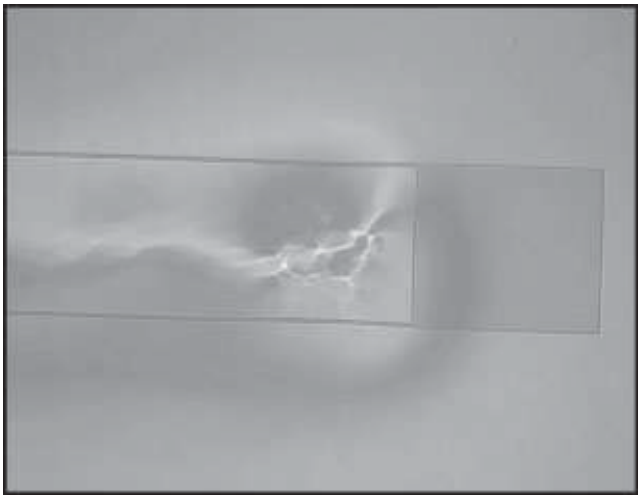

Figure 2: Under-etched xylophone.

from being over-etched and breaking through the oxide layer to being under-etched, only exposing a small portion of the oxide layer. This is easily explained by the difference in flop-hole sizes: larger holes etch at a faster rate than smaller holes on this scale as shown in Figures 1 and 2. To correct for this, the flop-holes were changed to only have 300 and 400 μm widths, but the etch depths continued to vary along the wafer. The non-uniform etching was attributed to machine error in the Unaxis 770 and was overcome by changing the width of each flop-hole to 1000 μm.

Another significant and unexpected problem that occurred was the low yield after oxide removal in the wet etch. Drying the xylophones in air strains them and causes them to warp and break away from the silicon base when the water evaporates. To avoid the phase change when drying, the xylophones were placed in a Critical Point Dryer after the oxide etch. The BOE was serially diluted in water, then methanol, which is replaced in the critical point dryer by carbon dioxide. The CO_2 is then heated and pressurized around its critical point to dry the sample. Unfortunately the influx of CO_2 into the chamber was too rough for the xylophones, causing them to break at the struts.

Conclusions:

This procedure proved unsuccessful in the fabrication of xylophone resonators. There are many possible alternatives to the fabrication process which could increase the yield of xylophones. To overcome the initial rush of CO_2 liquid into the chamber that destroys the xylophones, the strength of the struts needs to be increased. Bracing each strut with a nitride layer may make the xylophone sturdier and prevent breakage. Another alternative would be to enlarge the area surrounding the xylophones and increase the length of the struts to allow the liquid to flow past the xylophones more easily. Placing holes in the xylophones could also allow liquid to flow directly through the oscillators and relieve the pressure from the influx of CO_2.

The most promising option is to replace the BOE wet etch with a HF vapor etch which is more gentle on the silicon. This is very difficult to carry out because the temperature difference between the wafer and the HF must be held constant to avoid condensation, but we believe this would completely prevent the xylophones from breaking. Further time and investigation are needed to fabricate the xylophone resonators, which continue to be candidates for high force-sensitivity measurements.

References:

[1] J.A. Sidles, J. L. Garbini, et al, Reviews of Modern Physics, 67, 249-265, 1995.

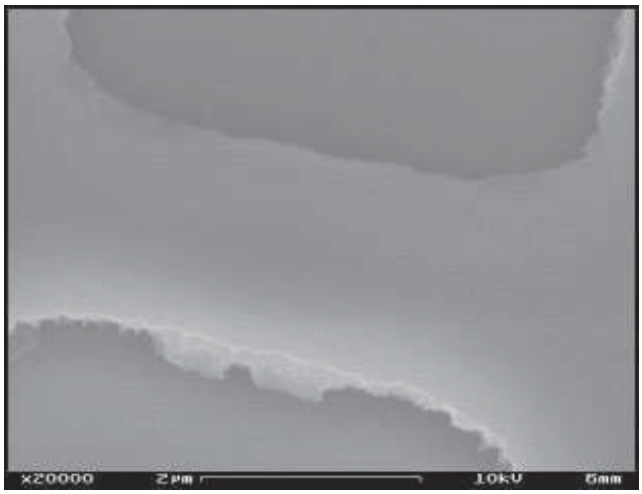

Figure 3: SEM micrograph of a 2 μm wide strut connecting the xylophone to the surrounding silicon.

Characterization of Random Copolymer Photoresists for Supercritical CO_2 Development Processes

Alexandar L. Hansen, ACS Chemistry Major, Carthage College

Dr. Christopher Ober, Victor Pham, MS&E Dept., Cornell University

viochemistry@iwon.com, cober@ccmr.cornell.edu, vqp2@cornell.edu

Abstract:

In this study, two random copolymers, *tert*-butyl methacrylate-r-1H, 1H-perfluoroctyl methacrylate (TBMA-F7MA) and tetrahydropyran methacrylate-r-1H,1H-perfluoroctyl methacrylate (THPMA-F7MA), were used for 248nm photolithography. Past studies using block copolymers achieved significant sub-micron feature resolution [1]. These polymers act as negative photoresists when in solution with photo acid generators (PAGs). Subsequently, reversal is necessary to be compatible with industry's positive-tone lithography standards. Using TBMA-F7MA, only 1 µm negative tone features could be achieved with little or no dark field resolution. The reversal process produced no results with TBMA-F7MA.

An IR study has shown that TBMA-F7MA is quite insensitive to the PAG. Two possible explanations for this are that the PAG and polymer do not interact well, as is indicated by an RBS study of the polymer, or the *tert*-butyl group is too stable to be cleaved by the PAG. Conversely, THPMA-F7MA was able to produce 0.5 µm negative tone lines and space, both bright and dark field, and 0.7 µm positive tone lines and spaces. However, flaws were noticed in the polymer film and are expected to be due to the polymer's low glass transition temperature and the necessary higher bake temperatures.

Introduction:

In recent years, much research has been directed towards the use of supercritical CO_2 ($SCCO_2$) in different applications due to its unique physical and chemical properties. Use of $SCCO_2$ as a developer in photolithography, in particular, has many advantages over aqueous and organic solvents commonly used in industry and research. Aqueous developmental processes have been found to cause pattern collapse due to capillary forces and surface tension [2-4]. $SCCO_2$ has no surface tension and can therefore remove resist without any pattern distortion. It also can readily remove fluorinated resists, which will be crucial for future 157nm DUV photolithography. Finally, and most importantly, it is environmentally friendly, as opposed to those organic solvents previously mentioned.

Previous research carried out by Pham *et al.* was done using block co-polymers of THPMA-F7MA and other polymers, which achieved significant results in e-beam patterning and 248nm photolithography. It is the purpose of this study, in part, to ascertain if the same results could be achieved using a random co-polymer.

Block copolymers are much more difficult to synthesize than random polymers, which makes them unattractive to industry. Another aspect of these polymers to consider is the fact that they act as negative tone resists. Once again, to be accepted in industry, these polymers need to be positive tone resists. For this reason a Diffusion Enhanced Silylated Resist (DESIRE) process is used to reverse the image. Characterization of the final patterned product is done using Scanning Electron Microscopy (SEM) and Atomic Force Microscopy (AFM).

Experimental Procedure:

The first step in the process is to spin coat a wafer with the photoresist. For TBMA-F7MA, a spin speed of 3500 rpm with a six second ramp produced nice, even films of about 0.4 µm. This is followed by a post-applied bake of 90°C for 60 sec. As for THPMA-F7MA, a higher spin speed of 4000 rpm is necessary, which produced reasonable 1 µm thick films. Post-applied bakes for THPMA-F7MA ranged from 70°C to 115°C, which will be explained later. The films are then exposed using a Nikon 248 with a standard Nikon dose test mask. A post-exposure bake of 90 or 115°C is

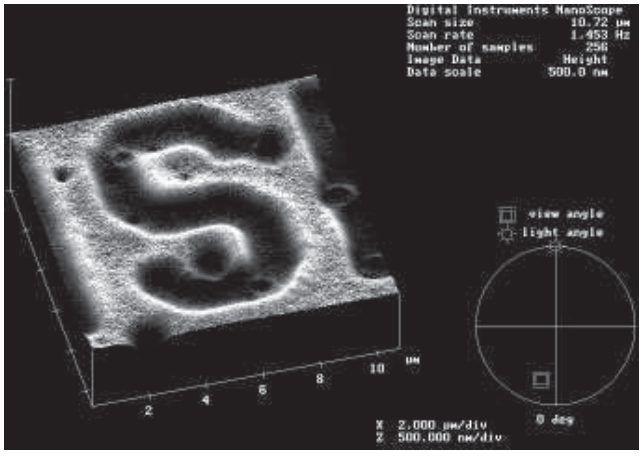

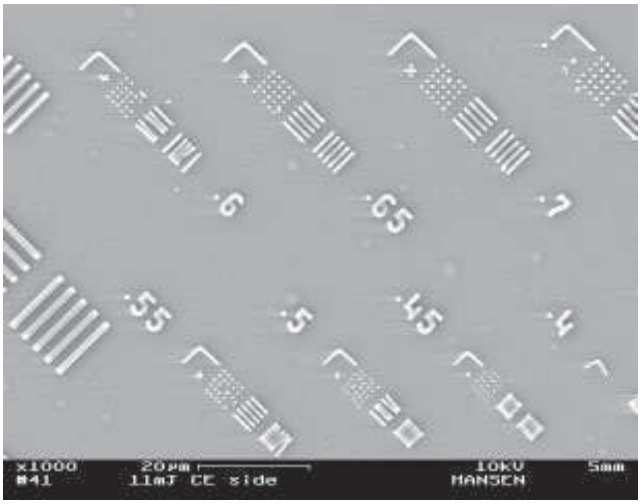

done to TBMA-F7MA samples while THPMA-F7MA samples are subjected to post-exposure bakes ranging from 70 to 115°C.

For a negative tone image, the patterns can be developed at this point. The patterns were processed with pressures ranging from 2000 PSI to 4500 PSI and a temperature between 40 and 50°C. The optimal pressure tends to be around 3000-3200 PSI. However, for image reversal the patterned film must be silylated with hexamethyldisilazane (HMDS). The coated wafer is placed on a hot plate at 100-120°C and HMDS is bubbled over it for 5, 10, or 20 min. Once silylated, the wafer must be flood exposed using an HTG contact aligner, followed again by a post-exposure bake. The reversed wafer can then be developed in the $SCCO_2$ developer.

Results and Conclusions:

Features obtained from the TBMA-F7MA samples were very disappointing. Dark field feature sizes were about 1 µm while little or no bright field features occurred. Reversal was virtually impossible with TBMA-F7MA. An IR study and RBS measurements were taken of these samples and it was found that the *tert*-butyl group was too stable and was not being cleaved by the PAGs. However, results from THPMA-F7MA were considerably better. Both bright and dark field resolutions were on the order of 0.5 µm for negative tone and 0.7 µm for positive tone. With more tweaking, it is possible that even better results are achievable.

One consistent problem that occurred was the presence of spots all over the wafer. It is suspected that these occur due to the high bake temperatures. The glass transition temperature of the polymer was measured to be between 60 and 65°C. This presents a problem since DESIRE must be done above 100°C. The lower post-applied and exposure bakes seemed to reduce the presence of the spots considerably, but all DESIRE runs had the spots. Future work should be focused on eliminating these spots, either by changing bake temperatures, revising the process, or making a polymer with a higher glass transition temperature.

References:

[1] Pham, VQ; Weibel, G; Hamad, AH; Ober, CK; Abstr. Pap.-Am. Chem. Soc., 2001, 221st PMSE-027.

[2] Namatsu, H.; Yamazaki, K.; Kurihara, K., Microelectron. Eng. (1999), 46(1-4), 129-132.

[3] Goldfarb, D.L.; de Pablo, J.J.; Neley, P.F.; Simons, J.P.; Moreau, W.M.; Angelopoulos, M., J. Vac. Sci. Tech. B, (2000), 18(6), 3313-3317.

[4] Tanaka, T.; Morigami, M.; Atoda, N., Jpn. J. Appl. Phys. Part 1, (1993), 32(12B), 6059-6064.

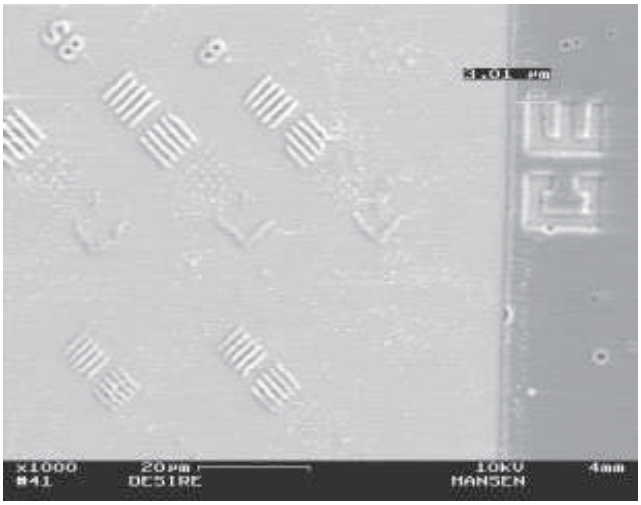

Fabrication and Characterization of Microfluidic Structures by Hot Embossing

Gizaida Irizarry, Mechanical Engineering, Univ. of Puerto Rico Mayagüez Campus

Drs. Mandy Esch, CNF, & Michael Shuler, Biomedical Engineering,
Sahil Kapur, Electrical & Computer Engineering, Cornell University
gizaida@hotmail.com, esch@cnf.cornell.edu, mls@cheme.cornell.edu

Abstract:

Hot embossing is a technique that provides an easy way to fabricate prototype microfluidic devices for use in research laboratories. The method is based on pressing a master which contains the negative image of the final structure into a polymer substrate that is heated up to above its glass transition temperature.

In this study, we used two methods to fabricate the embossing master: 1) we transfered the pattern onto a silicon wafer by standard photolitho-graphy methods and etched the silicon using deep reactive ion etching (DRIE), and 2) we used SU-8 processing on silicon wafers to create the same pattern as achieved with the DRIE process.

The fabricated masters were embossed into 2 mm thick sheets of polymethylmethacrylate (PMMA), poly (ethylene terephthalate) (PETG), and a polycarbonate-based plastic. After successful embossing, the channels were closed with sheets of PDMS, and the microfluidic flow was tested. Flow profiles indicate that the design of the channel entrance plays an important role for the flow speed at different points in the channels. By changing the entrance design and incorporating deflectors in the channels, the flow profile can be changed according to the needs of the application.

Introduction:

The fabrication of microfluidic devices by hot embossing is convenient and easy to accomplish because hot embossing can be performed with minimum requirements for equipment on inexpensive substrates such as sheet plastics. The masters needed for the embossing process can be fabricated using standard semiconductor and MEMS processes. Once a master is fabricated, it can be used numerous times to replicate the desired structures in plastic substrates.

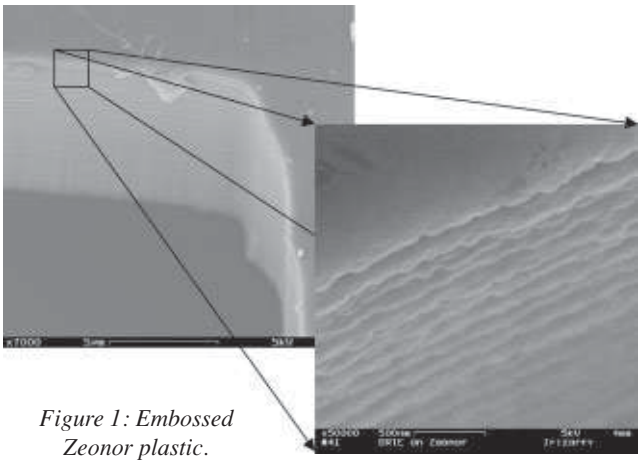

Figure 1: Embossed Zeonor plastic.

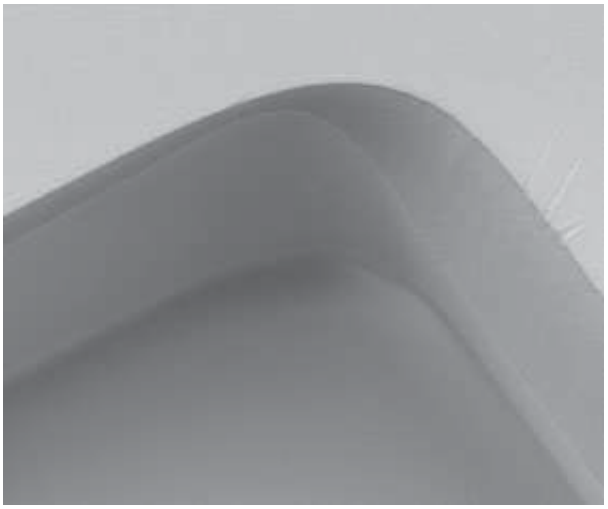

Figure 2: Zeonor plastic embossed from SU-8 template.

Applications of microfluidic devices fabricated by hot embossing include capillary electrophoresis [1], bio-sensors [2], and drug testing devices. The flow created in microfluidic devices is different from the flow in macrofluidic devices. Among other advantages such as cost effectiveness due to reduced reagent use and reduced size, the characteristics of the microfluidic flow account for some important advantages of microfluidic devices in comparison to large scale devices. These advantages are increased assay speed, and increased sensitivity in sensor applications [3].

In this study, we concentrated on a drug testing application. For this application, cells that mimic a specific organ of the human body, are cultured within the microfluidic network on the chip. The cells are then subjected to concentrations of a drug, and the reaction of the cells towards this drug is monitored. To receive reliable results from these experiments it is advantageous if all cells are subjected to the same amount of drug (e.g. microfluidic flow).

Procedure:

Masters for embossing were created by standard photolithography techniques. In the first case, deep reactive ion etching was performed on a UNAXIS 770. In the second case, SU-8 was processed as suggested by the manufacturer (MicroChem Corp., Newton, MA). The final depth of both masters was 20 µm. Embossing into PMMA, PETG, and a polycarbonate based plastic (Zeonor 1020R, Zeon Chemicals L.P., Louisville, KY) was performed at temperatures of 120°C (PMMA and Zeonor) and 90°C (PETG). The force applied to

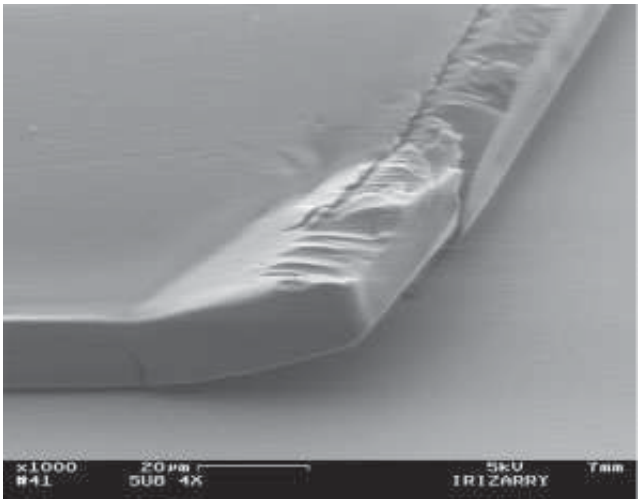

Figure 3: SU-8 Template used four times for embossing.

the 4" master and substrate was 7 kN or 20 kN. Bonding of plastic was attempted by heating sheets of plastics to temperatures between 80°C and 120°C and pressing the heated sheet against the embossed structures. Non-permanent sealing with poly (dimethyl siloxane) (PDMS) was achieved by clamping a flat PDMS sheet against the embossed structures. Holes were drilled to create the entrance and exit of each chamber. Dyed water was pumped through the chamber at a flow rate of 12 rpm and the flow behavior was recorded using a camera and tape recorder.

Results and Conclusions:

We first conducted embossing experiments using the silicon masters on which the negative of the final structures were created by DRIE. Embossing with these masters at optimum conditions as established previously was successful [4]. Figure 1 shows a corner of a microfluidic channel embossed into Zeonor. At a magnification of 50000x, it becomes visible that even the small ridge-like structures created on the sidewalls of the master by the DRIE process are transferred to the plastic. However, we often observed that the embossed structures exhibited uneven edges on one side of the microfluidic channels, and the number of embossing experiments conducted with one master seldom exceeded 2 to 3 experiments due to fracturing during the cooling phase of the process. Both of these results may in part be caused by the difference in thermal expansion of the silicon master and the plastic substrate during the embossing process.

More successful were experiments in which we used masters fabricated using SU-8 processing. Figure 2 shows a corner of a microfluidic structure embossed in Zeonor using an SU-8 master. Because the SU-8 master itself has smooth corners and sidewalls, the embossed structures also exhibit smooth sidewalls. The number of embossing experiments conducted with one master could be increased to at least 10 experiments. A disadvantage of SU-8 masters, however, is that the forces acting between the master and the substrate during the embossing process lead to deformation and destruction of the SU-8 as shown in figure 3.

To test the microfluidic flow in the channels, we sealed the channels with PDMS sheets. Although permanent sealing by bonding to a sheet of the same material as the embossed structure is more desirable, we found that sealing with PDMS was most successful, because it was repeatable. Structures sealed in this way did not leak during the experiments. The microfluidc profiles of the chambers are shown in figure 4a. These flow profiles can be changed by incorporating deflectors into the design (see figure 4b).

From this study, we concluded that the method chosen to fabricate the embossing master as well as the design of the structures on the master depends on the needs of the application. SU-8 masters were more durable than DRIE masters and could be used for up to 10 embossing experiments. However, the number of embossing experiments conducted with these masters is also limited because the SU-8 structures on the master are subject to deformation. The design of the entrance of the microchannels and the position of the deflectors inside the channels influenced the microfluidic flow. An important step during the fabrication of microfluidic channels is sealing the channels. More work needs to be done to establish reliable procedures with which this can be achieved.

Acknowledgments:

I would like to thank Dr. Mandy Esch, and Sahil Kapur for their unconditional help and understanding throughout my research. I'm also grateful to Prof. Michael Shuler, and Aaron Sin for their assistance and help in my research.

References:

[1] Wang, S. C., Morris, M. D., Analytical Chemistry, 2000, 72, 1448.

[2] Choi, J.-W.; Ding, Y.; Ahn, C. H.; Halsall, H. B.; Heineman, W.R.; Proc. 19th Annual Int'l Conference of the IEEE Engineering in Medicine and Biology Society. Magnificent Milestones and Emerging Opportunities in Medical Engineering (Cat. No. 97CH36136), IEEE, Piscataway, NJ, USA, 1997, vol. 5, 2264-3366.

[3] Ehrlich Daniel, J., Matsudaira, Paul, Trends in Biotechnology, 1999, 17, 315.

[4] Esch, M; Kapur, S.; Irizarry, G.; Genova, V.; Review of Embossing Master Fabrication Techniques and their Influence on the Quality of Embossing, in preparation.

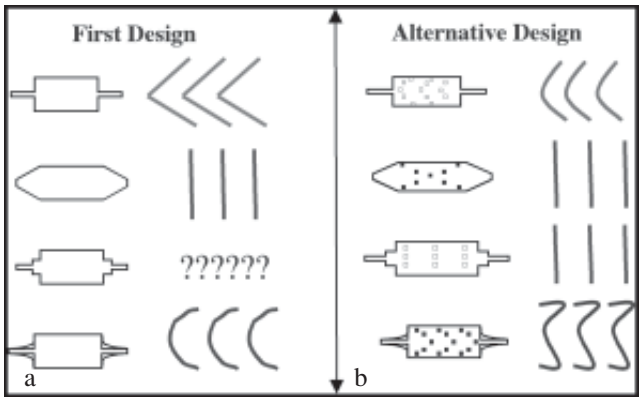

Figure 4: A drawing of the microfluidic flow inside the chambers.

T7 Immobilization to Gold-Patterned Silicon Wafers

Jacob L. Jordan, Chemical Engineering, Vanderbilt University
Carl A. Batt, Food Science, Christine Campagnolo, Microbiology, Cornell University
jacob.l.jordan@vanderbilt.edu, cab10@cornell.edu

Abstract:

Described herein are the studies performed to evaluate the binding activity between bacteriophage T7 and its putative target, streptavidin. Previously, bacteriophage T7 was genetically modified to incorporate a biotin-like HPQ sequence into the major coat protein (MCP) of the phage head.

Using a thiol-based surface chemistry, streptavidin was covalently immobilized to gold-patterned silicon surfaces. Experiments were then performed with the gold-patterned silicon surface under varying conditions to evaluate the binding and specificity of T7 to the immobilized streptavidin. To confirm binding of the bacteriophage and protein, fluorescence microscopy, surface plasmon resonance (SPR) and atomic force microscopy (AFM) experiments were performed.

The fluorescence and SPR experiments did not indicate the interaction of T7 with streptavidin, while the AFM experiments showed the presence of spherical particles with an average diameter of 63.9 nm, on the same size order as the phage. This data suggested T7 bound nonspecifically to both the silicon and gold surfaces, with no preference to the areas where streptavidin was know to be concentrated.

Introduction:

Bacteriophage (phage) are viruses that specifically infect bacterial strains. Previously, the major coat protein of bacteriophage T7 was genetically modified to incorporate a HPQ motif into the protein sequence.

This motif resembles biotin, a chemical known to bind with high affinity to the protein streptavidin. By first binding streptavidin to a gold patterned surface on a silicon substrate and then introducing T7, the binding of this system was evaluated by analytical instruments. Future applications of this system include its use in a biosensor that detects the presence of *E. coli* using optical diffraction [1].

Procedure:

Preparation of Gold-Patterned Surfaces:

The gold-patterned surfaces were designed in the form of I-beam patterns, with widths that ranged from 2 μm to 20 μm. A template mask was first created using the Mann 3600 pattern generator and then transferred to wafers using a 5x g-line stepper. Each wafer was prepared using P20 primer and Shipley 1813 photoresist. After development in MIF321, a 10Å layer of chrome was deposited, followed by a 200Å layer of gold using the CVC SC4500 e-beam evaporator. Lift-off was then performed in an acetone bath to remove unexposed photoresist and overlaying metal layers, leaving a gold-patterned silicon surface.

SPR Testing:

Using carboxyl-terminated chemistry, gold-patterned surfaces were activated with a solution of 0.2 M EDC and 0.05 M NHS in water. Streptavidin (250 μg/mL) was then immobilized on the surface, and then blocked with bovine serum albumin (BSA). T7 binding studies were performed in Tris-buffer saline (TBST; pH 7.5) containing 0.05% Tween 20.

Fluorescence Microscopy Testing:

Using carboxyl-terminated chemistry, gold-patterned surfaces were activated with a solution of 0.2 M EDC and 0.05 M NHS in water. Streptavidin (250 μg/mL) was then immobilized on the surface, after which the unreacted esters were hydrolyzed in a phosphate buffer (pH 8.6). T7 (10^8 pfu/mL) in TBST (pH 7.5) was then incubated on the surface.

Figure 1. Fluorescence microscopy image of immobilized streptavidin using a Nikon Labpont-2 microscope.

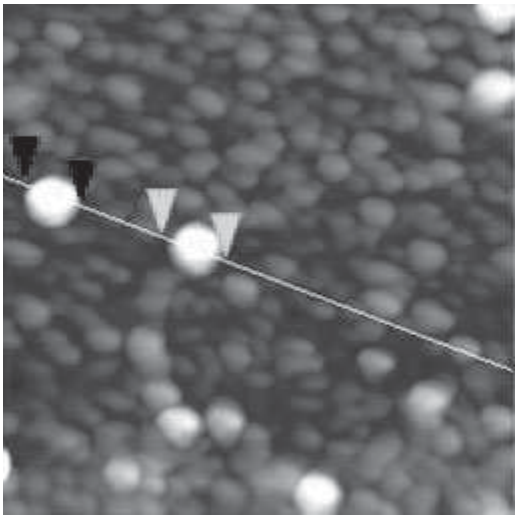

Figure 2. Surface images of slides incubated with T7 showing the presence of spherical dots greater than 30 nm in height with an average diameter of 63.9 nm on both the gold and silicon surfaces.

Next, anti-T7 (4 µg/mL) and a FITC-labeled goat anti-rabbit (100 µg/mL) antibody were the incubated in sequence. Fluorescence images were captured using a Nikon Labpont-2 microscope.

AFM Testing:

Surfaces were prepared with streptavidin as described in the previous section. T7 (10^8 pfu/mL) in TBST (pH 7.5; 0.05% Tween 20) was then incubated on the surface. A Digital Instruments AFM was used to acquire the images and Nanoscope III software was used for the analysis.

Results and Discussion:

SPR Testing:

Streptavidin was shown to bind to the activated surface chemistry with a change of 0.0532 deg. Blocking of the surface with BSA caused a change of 0.0152 deg. T7, however, showed no response, suggesting the surface binding was not detectable by this method. Experimental parameters such as buffer conditions and the flow rate should be tested in the future to optimize the parameters for the study.

Fluorescence Microscopy Testing:

Treated slides demonstrated the presence of streptavidin on the gold-patterned areas with high background, suggesting the conditions for streptavidin immobilization have yet to be optimized (Figure 1). T7 binding was not detectable. This could be attributed to the low concentration of anti-T7 antibody or other experimental parameters, such as pH and ionic strength.

AFM Testing:

Slides incubated with T7 showed the presence of spherical dots greater than 30 nm in height with an average diameter of 63.9 nm on both the gold and silicon surfaces (Figure 2). Inactivated slides having only the surface chemistry showed the presence of spherical features with an average diameter of 84.4 nm (Figure 3). This data suggests that T7 bound nonspecifically to both the silicon and gold sections.

Conclusion:

Immobilization of T7 may have been observed using atomic force microscopy. The results of surface plasmon resonance and fluorescence microscopy testing did not register the presence of T7, suggesting that modifications to the experimental conditions need to be further considered. Further testing will be performed to verify the results of AFM, as well as studies discussed previously.

Acknowledgements:

I would like to thank Christine Campagnolo and the entire Batt Lab, Professor Carl Batt, the Cornell Nanofabrication Facility, and the National Science Foundation.

References:

[1] Batt et. al. Diffraction-based cell detection using a microcontact printed antibody grating. Anal. Chem. 70, 1108 (1998).

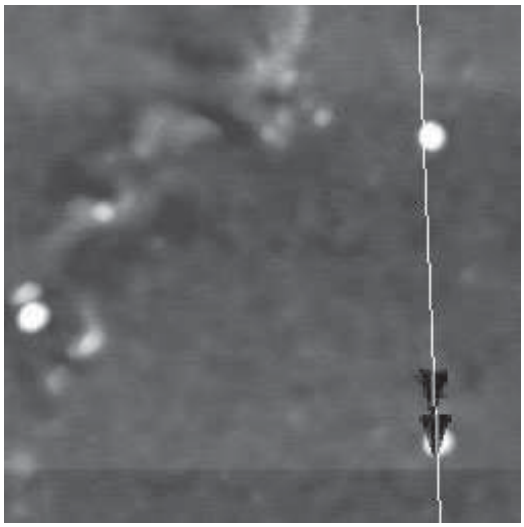

Figure 3. Surface images of inactivated slides showing the presence of spherical features with an average diameter of 84.4nm.

Micropatterning of Optical Gratings and Bulk Glass

Mr. Michael P. Krause, Electrical Engineering, Wayne State University

Dr. Dieter Ast, Lin-lin Wang, CCMR, Cornell University

ag7537@wayne.edu, dast@ccmr.cornell.edu

Abstract:

The goal of this project was to investigate the glass flow mechanisms at elevated temperatures in micron scale gratings. The Corning glass samples were comprised of alumina, calcia, and silica compositions with the silica composition varying from 25% to 75%. Uniform gratings were produced with feature sizes ranging from 20 µm to 2 µm at depths of 7000Å to 2000Å dependent upon the sample's percentage of SiO_2. These gratings were then subjected to temperatures 130°C above the strain point (TS) of the glass compositions. The data collected at three different annealing times were used to calculate the flow mechanism at work.

Introduction:

The rationale of this research is to examine the stability of fine features in glass substrates rather than traditional silicon for MEMS fabrication. The advantages of using glass vs. conventional silicon MEMS are due to the similar index of refraction (n) compared to optical fibers, the non-reactive properties in biological systems, and for the transparent characteristics for optical (visible spectrum) techniques in biology. Typically MEMS are subjected to elevated temperatures for long durations. At such elevated temperatures, glass begins to re-flow by two main mechanisms: Viscous Flow in the Bulk (micron scale features) and Surface Diffusion (feature sizes less than 1000Å).

To answer the question of stability, the flow mechanisms in the silica-calcia-alumina glass substrates need to be identified.

Procedure:

To confirm assumptions that the viscous flow mechanism was at work in micron scale feature sizes, various samples had to be produced. Twenty-one samples, three of each composition, of one-dimensional gratings were produced with spatial frequencies of 250, 500, 1000, 1250, 1667, and 2500.

Upon completion of a thorough cleaning, the samples were ready for the lithography process. This lithography process was accomplished by using Shipley 1813 photoresist in conventional lithography techniques on a 2500Å Chrome layer. A custom-designed mask was used to expose the patterns on the Karl Suss Contact Aligner. After development, the Chrome layer under the exposed regions of the resist was removed by a Cr-14 etchant. Once the remaining resist was removed, the samples were etched in groups of seven (one of each composition) in the Magnatron Enhanced Reactive Ion Etcher (MIE) for 20 minutes at a power of 1.03 kW using CF_4 as the reactant gas. The Chrome layer has an etch rate similar to that of the glass compositions, so it served as an acceptable etching mask. With the patterns etched into the glass substrates, the remaining chrome layer was removed, leaving behind the required gratings for further testing.

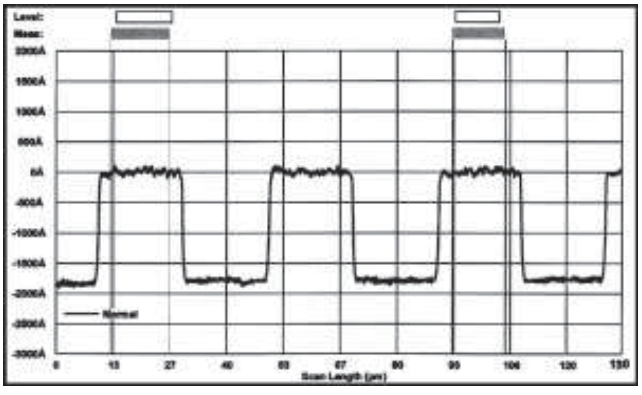

Figure 1. Resultant surface profile after MIE etching.

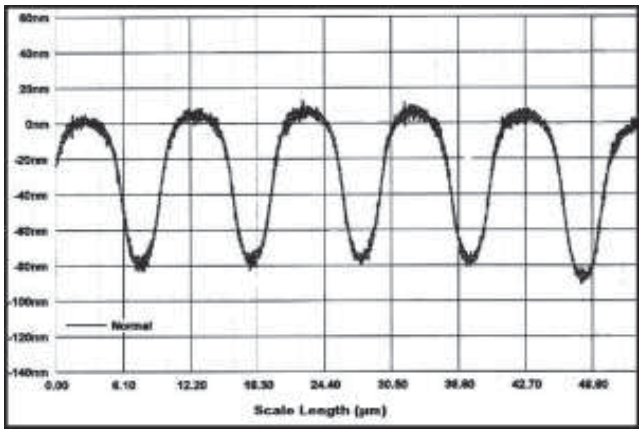

Figure 2. Relaxed surface profile after 30 min at 928°C.

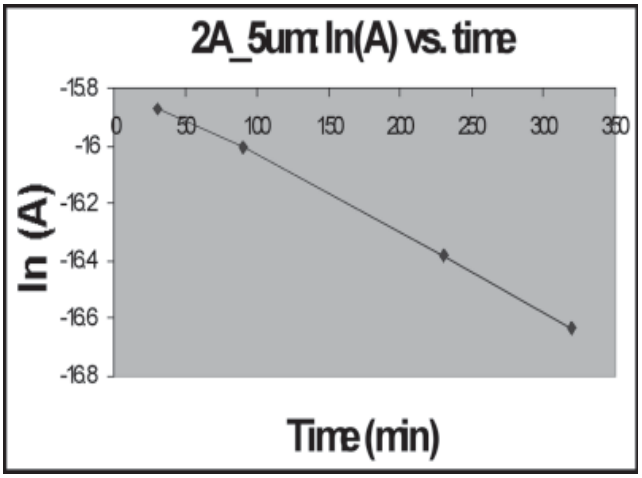

Figure 3. 33.4% SiO_2 relationship for special frequency of 1000.

Characterization of the resultant gratings was of paramount importance. The initial and all subsequent surface profiles were obtained in graphical form from the P-10 Surface Profiler. The etched surface profile, as seen in Figure 1, was rectangular in form due to the masking technique.

With the initial rectangular spacing and depths known, the annealing experiments began. Annealing is the process of rapidly heating and cooling the samples to temperatures 130°C in excess of their strain point (T_S = 800°C).

The desired results are to relax the surface profile to a simple sine wave as seen in figure 2. This annealed sample showed an amplitude reduction anywhere from 8 to 30%, which was dependent upon the percentage of silicon dioxide and the feature size in question. The relaxation shown in figure 2 was accomplished by 30 minutes at 928°C in a three zone furnace. This initial waveform was used as the basis of the data collection. Once the initial sine wave pattern was characterized, additional timed annealing runs were conducted at 60, 140, 220 minutes for glass compositions under 58.4% silicon dioxide SiO_2.

Results:

With the surface profiles charted, data processing ensued to calculate the flow mechanism. For the given glass compositions, four relationships of amplitude vs. time were known. The following data represents calculations done on the 33.4% SiO_2 sample. The natural logs of the amplitude vs. the annealing times were plotted for spatial frequencies of 500, 1000, and 1667. Figure 3 shows the aforementioned relationship for the spatial frequency of 1000 (5 µm feature sizes). Each of these graphs, for the given spatial frequency, has a respective tau or characteristic decay time, which is the slope of the line.

The characteristic decay times were -0.00097019, -0.00271371, and -0.000561297 respectively. The final numerical processing was to plot the characteristic decay time vs. the special frequency. If this relationship is linear, then the flow mechanism at work is viscous flow in the bulk. Figure 4 shows the experimental results. The relationship of the characteristic decay time vs. the special frequency is nearly linear; the minor inconsistency is due to the tolerances of the P-10 surface profiler. Based on the experimental data, we are able to conclude that the flow mechanism at work in micron scale feature sizes is viscous flow in the bulk.

Further research needs to be conducted to determine the flow mechanism at work for feature sizes less than 1000Å. It was experimentally proven that gratings with feature sizes of 300, 600, 900Å could be successfully produced in a PMMA resist on the glass substrates. These trials were conducted using the Leica VB6 e-beam lithography tool. The same aforementioned procedure is valid for determination of surface diffusion flow mechanism.

Acknowledgments:

I would like to thank Dr. Dieter Ast and Lin-lin Wang from the CCMR group at Cornell University for their support and knowledge.

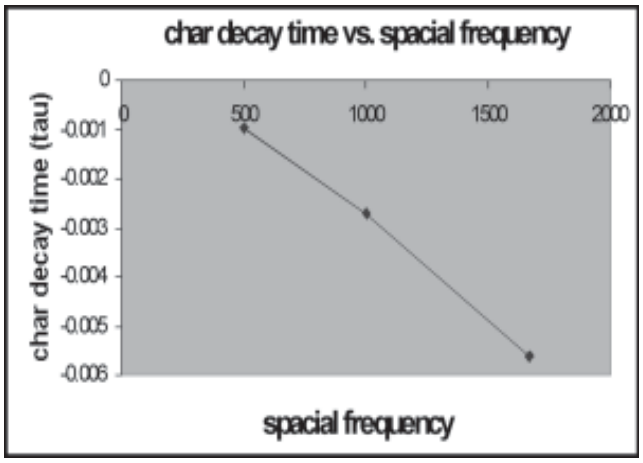

Figure 4. 33.4% SiO_2 relationship for determination of flow mechanism.

Fabrication and Characterization of Microfluidic Device for Emulsion Polymerization

Chun-Cheng Thomas Lin, Electrical Engineering, University of Southern California

Dr. James Engstrom, Chemical and Biomolecular Engineering, Dr. Tyler McQuade, Chemistry, Mr. Stephen Cypes, Chemical and Biomolecular Engr, Cornell University

chunchel@usc.edu, jre@cheme.cornell.edu, dtm25@cornell.edu

Abstract:

A microfluidic device was fabricated for the study of dynamic pattern formation by shearing one liquid into another immiscible liquid to create droplets, known as micelles, in order to continuously produce polymer fibers. This group of micelles is called an emulsion. It has been shown that micelles' size and shape vary with the width of the channels and the pressures of the immiscible liquids, therefore possibly affecting the properties of the resulting polymer fibers.

This project employed two different processes to build the device: (1) standard lithography processing resulting in trenches that defined the microchannels, and (2) image reversal resulting in a mold used for soft lithography with poly-dimethylsiloxane (PDMS). The fabrication processes included designing the channels using a CAD program, creating the masks, performing the necessary proximity photolithographic steps, and finally etching the microchannel formations using the Bosch etching technique. The resulting channels were 50 µm wide and 50 µm deep, as revealed by scanning electron microscope (SEM). The characterization of the device with respect to polymer fiber formation is currently being investigated.

Introduction:

The goal of my project was to fabricate and to characterize a microfluidic device suitable for emulsion polymerization using hydrodynamic focusing to create polymer nanofibers. An emulsion polymer-ization is a collection of stable polymer micelles formed from a monomer dispersed in an aqueous initiator phase.

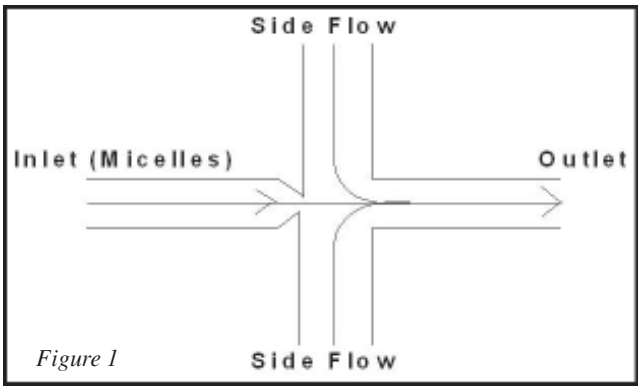

Figure 1

The micelles can have many patterns depending on flow characteristics. Under conditions where the aqueous flow rate is less than the monomer flow rate, separated micelles are formed. As both liquids flow at the same rate, micelles attach to each other to form a single continuous stream. When the aqueous stream flows faster than the monomer stream, complex patterns, such as a pearl necklace shape, begin to emerge in the channel.

After micelles are created, they then pass through a cross junction in our device, where the micelles flow from the inlet channel while two aqueous liquids squeeze these droplets from the side channels (known as hydrodynamic focusing), to produce an extremely thin focused inlet stream. Figure 1 shows that a nozzle was designed at this junction to increase the velocity of the inlet stream and to allow the side flow to come into the cross junction more easily. This technique will produce a polymer fiber with nanometer dimensions.

Process:

To fabricate the devices, we started with the pattern generator to create a mask. The masks were used with a contact aligner for pattern transfer to silicon wafers. We then used Bosch etching to form 50 µm micro-channels. In Figure 2, we can see the depth of the cross channel of the silicon wafer mold. Once the wafer mold was complete, we poured and cured poly(dimethylsiloxane) (PDMS) on top. PDMS was peeled off the wafer and sealed with another flat PDMS surface. Plastic tubing was sealed to openings in the PDMS using a PDMS pre-polymer mixture, and the tubing connected to a syringe pump.

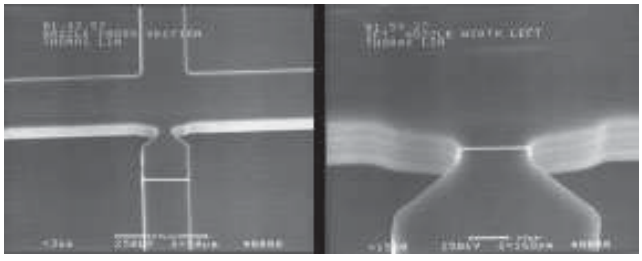

Figure 2

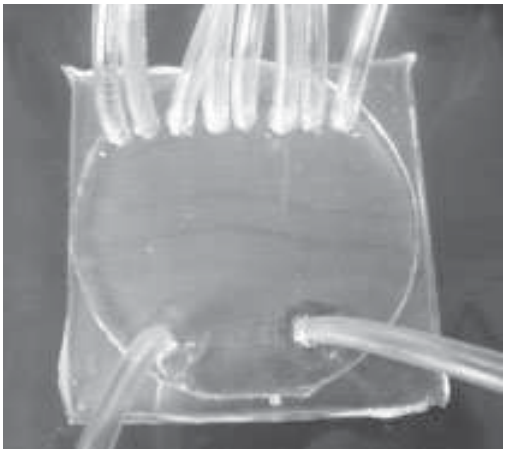

Figure 3

We can see this final product in Figure 3. For the second device in which the microchannels were defined directly in the silicon wafer, as shown in Figure 4, we used Bosch etching with back-side alignment to etch holes through the wafer in order to deliver fluids from a syringe pump into the channels.

For Bosch etching, we calculated the thickness of our etch masks, photoresist and PECVD oxide, based on their selectivity to silicon etching. The selectivity of silicon versus resist and oxide are approximately 70 to 1 and 150 to 1, respectively. Thus, we deposited 2 µm oxide on the front of the wafer, and 3.5 µm of oxide on the back of the wafer. After the wafer was etched, we striped all the oxide away using HF cleaning. Finally, we did an RCA clean to wipe out surfaces before anodically bonding to a pyrex wafer.

Results and Conclusions:

After both devices were made, we first characterized the emulsion polymerization system with the PDMS device. A syringe pump was used to deliver different flow rates of toluene and rhodamine-dyed water to the device to observe flow characteristics.

During the experiment, several problems were encountered. First, leaking occurred at the tubing connections due to poor sealing characteristics. Also, air trapped in the channels resulted in undesirable flow characteristics. Possible solutions to this problem are lowering the flow rates or adding surfactant to reduce surface tension. Due to the time constraint, we were unable to finish characterizing the system; however more work is currently being done.

Acknowledgement:

I would like to thank Professor James Engstrom and Stephen Cypes for all their help, as well as all the CNF staff for their assistance. Also, I want to thank Professor Tyler McQuade for letting me using his chemistry lab for my project.

References:

[1] T. Thorsen, R.W. Roberts, F.H. Arnold, and S.R. Quake, Dynamic Pattern Formation in a Vesicle-Generating Microfluidic Device, Physical Rev. Letters, Vol.86, No.18 (30 April 2001), 4163-4166.

[2] J.B. Knight, A. Vishwanath, J.P. Brody, and R.H. Austin, Hydrodynamic Focusing on a Silicon Chip: Mixing Nanoliters in Microseconds, Physical Review Letters, Vol.80, No.17 (27 April 1998), 3863-3866.

[3] M. Elwenspoek, and H. Jansen. Silicon Micro-machining. Cambridge Univ. Press, 1998.

[4] Rodriguez, F.; Principles of Polymer Systems, 4th ed. Taylor & Francis: 1996.

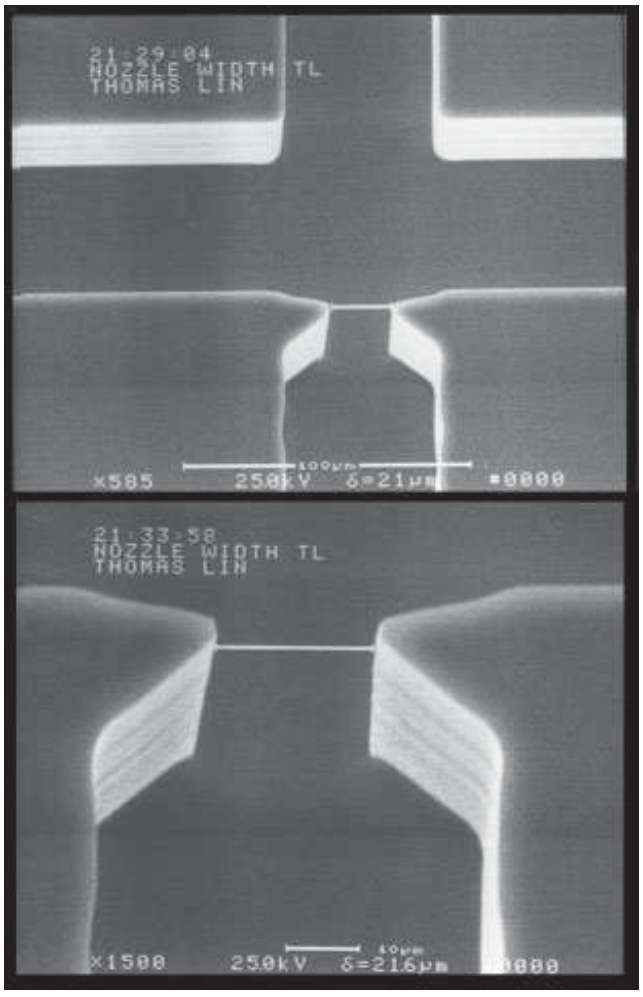

Figure 4

Fabrication of Variable-Thickness Structures with E-Beam Sensitive HSQ Resist

Omar David Negrete, Electrical Engineering, University of New Mexico

Alan Bleier, Cornell Nanofabrication Facility, Cornell University

nomar@unm.edu, bleier@cnf.cornell.edu

Abstract:

Hydrogen Silsesquioxane or HSQ is desirable in the electronics industry as an inter-level material because of its planarity and its low dielectric constant. We have investigated a use for this material; HSQ (Fox-17 Dow Corning Inc), for grayscale e-beam lithography to create optical devices. The Leica VB6 e-beam writer was our primary tool.

For preliminary data, we wrote several 4 x 16 arrays of 20 µm x 40 µm and 40 µm x 80 µm rectangles. To find the optimal contrast curve for grayscale, we varied exposure dose and development parameters. Each trial was measured by the Alphastep P-10 profilometer for resist height measurement. Profile information was gathered by AFM for analyzing proximity effects due to electron backscatter.

A structure with stepped dosing was also created in which AFM imaging revealed roughness across the height variations. If a process such as O_2 plasma etching can be used to smooth out the roughness, fabrication of an actual device can be further investigated.

Introduction:

Hydrogen Silsesquioxane (HSQ) is a low K, spin-on dielectric, used as an interlevel for integrated circuits. HSQ has been investigated for grayscale lithography and as an alternative for fabrication of variable-thickness structures, because of its sensitivity to electron beam irradiation and because of its controllable spin-on thickness. Most grayscale lithography has been demonstrated with PMMA to fabricate structures such as blazed gratings, Frensel lenses, phase-relief holograms and other optical devices [1]. As optical devices continue to decrease in size and increase in efficiency, the necessity to create grayscale devices at a high level of precision becomes more apparent. HSQ has been shown to have both the high contrast and the grayscale sensitivity necessary for the fabrication of such devices.

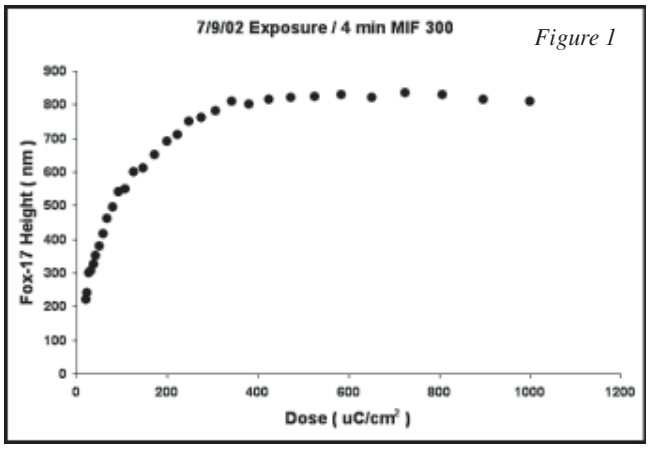

Figure 1

As with any e-beam lithographic process, electron backscatter was a concern. As varied dose-range information was gathered and assimilated into contrast curves, backscatter was also evaluated by mathematical modeling [2]. The results in modeling the backscatter effects, suggests that this analysis is viable for future backscatter compensation systems.

Variable thickness structures were created using information from contrast curves and shown to have nominal profile shape. However, surfaces appeared rough. Here we describe the procedure in characterizing HSQ for grayscale lithography, which include methods of exposure, development, and conclusions.

Procedure:

The HSQ examined was Dow Corning's Fox-17. In using this product, we found it to have a short shelf life (1-3 weeks) and it could not be stored in glass

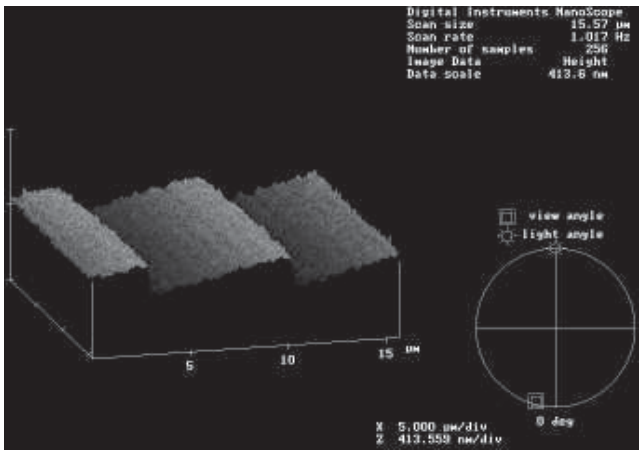

Figure 2

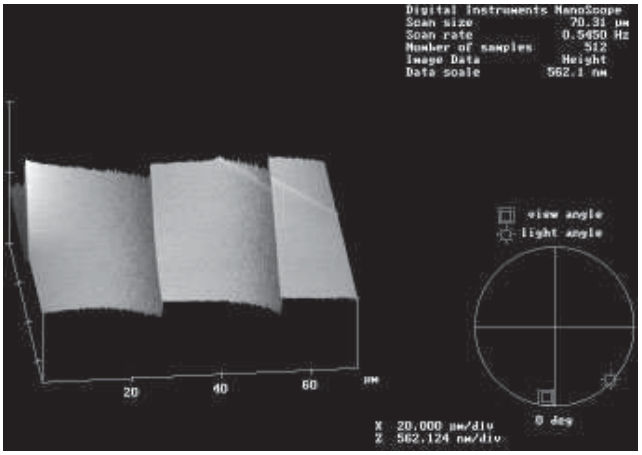

Figure 3

containers. In preparation for exposure, Fox-17 was spun on 6-inch silicon p type wafers <100> that were subject to solvent clean and 15 min. dehydration bake at 200°C. HMDS was used as a primer for the Fox-17 and was spun at 2K until visibly gone. Fox-17 was then spun at 2K for 60 s and then hard contact baked at 220°C, yielding 8000Å. The exposure tool was the Leica VB6 which ran at 100 kV emitting a 2nA current.

To seek the full spectra of e-beam sensitivity, a large dose matrix was implemented that ranged from 20 µC/cm^2 to 1000 µC/cm^2. Features were rectangular: 40 µm x 80 µm; this size was determined by the need for features large enough to permit measurement of backscatter but small enough to create uniform features. Four different types of development were carried out.

The first three were short solvent developments (5 s - 4 min) in MIBK (carrier solvent for Fox-17), MIBK: IPA (1:3), and acetone. The fourth and most promising was TMAH (MIF-300), which gave optimum dose vs. resist cross linked variance for a 4 min emersion development as shown in figure 1. Resist height was measured with an Alpha-step P-20 ellipsometer and compiled into a contrast curve as shown in figure 1. Finer details about surface roughness and profile information were gathered through Atomic Force Microscopy (Digital Instruments AFM). A variable thickness structure, similar to an 8 step blazed grating, was created. AFM imaging showed that the surfaces were rough; however the shape did match the nominal profile (see figure 2).

A 32 step blazed feature was also attempted (see figure 3). Its surface was also rough and its profile followed the contrast curve. Both structures followed the contrast curve (figure 1) closely but also showed to be heavily effected by backscatter. Creating optical devices with HSQ would require compensation of the backscatter effect, thus, mathematical modeling of the e-beam and its backscatter was investigated using Matlab.

The method was to model the electron beam with its backscatter with a 2-D Gaussian and interpolate it with the actual profile of one of the rectangular HSQ features, then fit the profile with the dose vs. height information of the contrast curve. The standard deviations in our fit match those of other similar work indicating that this process would be viable for a future proximity correction system (see figure 4) [2].

Conclusion:

Variable thickness structures were created with HSQ e-beam resist. A contrast curve was generated for HSQ and it shows potential for grayscale lithography with HSQ. Future work would include further analysis of the backscatter correction and smoothing of the surface of these features. Proposed solutions are O_2 plasma followed by annealing [3].

References:

[1] D. Wilson, P. Maker, R. Muller, P. Mouroulis, "Fabrication and performance of optical interconnect t analog phase holograms made by electron beam lithography," Optoelectronic Interconnects and Packaging 1996, SPIE Proceedings Vol. CR62, Feb. 1996.

[2] G.Owen, "Methods for proximity effect correction in electron lithography," J. Vac. Sci. Technol. B 8 (6), Nov/Dec 1990.

[3] D. M. Tanenbaum, A. Olkhovets, L. Sekaric, "Dual exposure glass layer suspended structures: A simplified fabrication process for suspended nanostructures on planar substrates," J. Vac. Sci. Technol. B 19(6), Nov/Dec 2001.

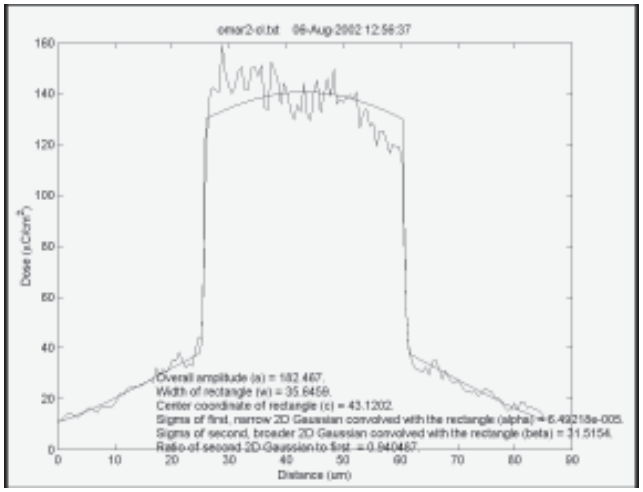

Figure 4

Developing Biosensors Based on Thin Film Transistors

Trang Nguyen, Electrical Engineering, San Jose State University

George Malliaras, Jeff Mason, MS&E, Cornell University

trangnguyen427@hotmail.com, george@ccmr.cornell.edu

Abstract:

Organic thin film transistors (OTFT's) have the potential of detecting the presence of DNA within aqueous solutions that flow between the source and drain. The goal of this research project was to fabricate and test the functionality of transistors while: a) varying the width between the transistor's source and drain; b) varying the microfluidic channel width of the aqueous solution traveling across the transistor and; c) varying the transistor's semiconductor material. Transistor patterns with varying widths between source and drain were designed on CAD and transferred to glass masks. Gold electrodes were then patterned onto silicon wafers using standard photolithographic techniques. Organic semiconductor materials were later deposited onto the transistors and aqueous solutions were flowed across them. The current and voltage across the transistor was measured while varying each parameter. These data points made it possible to create a set of current versus voltage curves.

Introduction:

Organic thin film transistor (OTFT) based biosensors have several advantages over conventional biosensors. Unlike inorganic TFT's, OTFT's allow biological molecules to be covalently bound directly to the organic semiconductor, which should lead to improved sensitivity. In addition, OTFT based biosensors are less expensive to fabricate because organic semiconductors can be easily deposited on transistors by spin-coating or thermal evaporation. These techniques allow for the organic transistors to be created on a variety of different substrates. OTFT's, thus, provide a means of improving the sensitivity and flexibility of biosensors while at the same time lowering the fabrication costs.

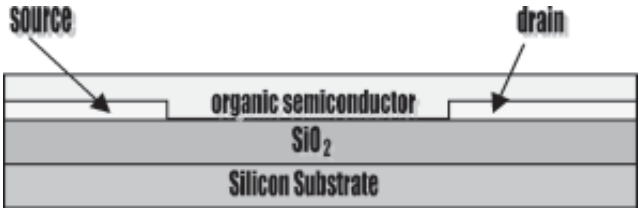

Figure 1: Structure of an organic thin film transistor.

Figure 1 shows the structure of our OTFT's. For an OTFT to function as a biosensor it must be able to detect DNA within aqueous solutions that flow between the source and drain of the transistor. This research project was, therefore, aimed at understanding how OTFT's function when in contact with aqueous solutions.

Procedures:

Transistor source-drain patterns shown in Figure 2, were designed on CAD and transferred onto four-inch glass masks via the Mann 3600 Pattern Generator. Each mask contained eight source patterns and thirty-two drain patterns. Several masks of the same general design were created, but the width between source and drain varied between 10 μm and 100 μm.

The patterns on these masks were transferred onto three-inch silicon wafers with 3000 Å of thermal oxide using standard photolithographic techniques. In the first part of this process, P-20 primer and Shipley 1813 photoresist were spun onto the surface. The HTG contact aligner was then used to transfer the mask design onto the thin layer of photoresist. An image reversal was performed followed by the emersion of the entire substrate in MF321 developer.

This process removed certain parts of the photoresist, exposing only the areas of the substrate

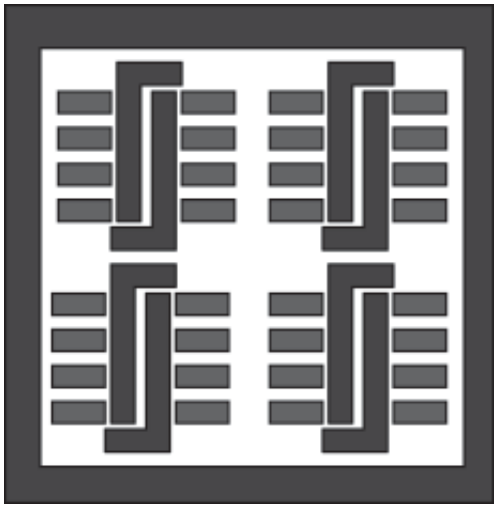

Figure 2: Source-drain patterns for OTFT.

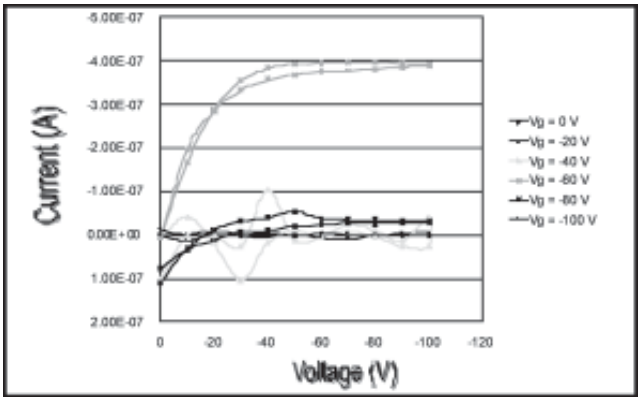

Figure 3: Plot of faulty transistor's I-V curves.

which corresponded to the initial source-drain pattern. The Plasma Therm 72 Reactive Ion Etcher was used to remove any remaining photoresist residue. 60 Å of chrome and 500 Å of gold were then evaporated onto the substrate via the CVC SC4500 Evaporator. The remaining photoresist was then lifted off with 1165 remover leaving the substrate with source-drain electrodes patterned in gold. Finally, 500 Å of pentacene was thermally evaporated onto the wafers.

Microfluidic channels were fabricated in much the same fashion. A mask was designed to create microfluidic molds varying between 20 µm to 80 µm. The mask pattern was transferred to a silicon wafer spun with SU-8 photoresist. After development, narrow ridges of SU-8 were left and used as a mold for poly (dimethyl siloxane) (PDMS). Liquid PDMS was poured onto the entire substrate and then cured at 60°C. When the PDMS had firmed, it was peeled off the mold and placed on top of the OTFT so that the microfluidic channel was centered between the source and drain.

Once all devices had been fabricated, they were tested using the Keithley I-V Measurement System. The source was grounded and the voltage of the drain was varied between 0 and 100V while the gate was kept constant. A family of I-V curves could then be graphed for each transistor for a series of gate voltages.

Results and Conclusions;

Testing the transistors produced unexpected I-V curves. Figure 3 shows a graph of the typical data that was collected for each transistor. The graph shows that the devices were not behaving as ideal transistors.

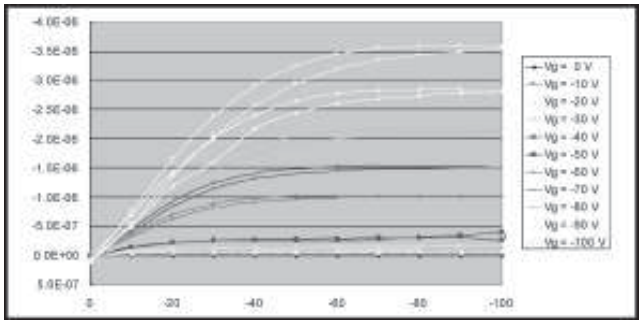

Figure 4: Plot of working transistor I-V curves.

In addition, high leakage current was measured between the gate and the source. When the devices were observed under a microscope, it was found that at high gate voltages, the gold areas touching the probe blew off and created large 200 µm craters. From these problems, we hypothesized that our transistors had been created on faulty oxide.

Oxide was, thus, grown on a whole new batch of wafers, and devices were fabricated on them. When these new devices were tested, we obtained data as shown in Figure 4. The data that was collected from the new batch of transistors were much better than the initial batch. This new data supported our hypothesis.

Due to problems with the oxide layer, the transistor's functionality could not be accurately determined when in contact with aqueous solutions. Further investigations will include creating new test devices with a reliable oxide layer. These new devices will then be tested when in contact with aqueous solutions. Once the transistors have been characterized, further investigation can be done on the transistor when changing the OTFT's organic semiconductor.

Acknowledgments:

I would like to thank the National Science Foundation for funding my research as well as the staff at Cornell Nanofabrication Facility. I am especially grateful to my Principal Investigator, George Malliaras for making sure that everything ran smoothly. Lastly I would like to thank my mentor, Jeff Mason for all his help, guidance, and constant encouragement throughout the summer.

Novel Filtration Geometry: Molecular Sieves

Diego Rey, Electrical Engineering, University of California Santa Barbara

Dr. Michael Spencer, Electrical & Computer Engr, Lori Lepak, Chemistry, Cornell Univ.

drey@umail.ucsb.edu, spencer@ece.cornell.edu

Abstract:

With the use of photolithographic and other micro-electronic manufacturing techniques, filters can be made with constrictions on the nanometer scale.

A thin silicon wafer with a layer of aluminum deposited on one side is etched vertically from the front and back up to the interface with the aluminum. The aluminum is then etched laterally producing a restrictive passage. The thickness of the aluminum layer can be accurately controlled and is in the order of 5-10 nm allowing for the fabrication of sieves that are specific to protein sizes. There are many possible uses for this technology including separating specific proteins from a mixture. Specifically, the capability of these sieves to separate DNA from hemoglobin will be tested. This new technology can also be implemented in a microscopic size making it possible to integrate the sieves into microchip-based devices.

Introduction:

These molecular sieves will be used in applications such as separating DNA from hemoglobin. A DNA strand has a diameter of 2.0 nm and hemoglobin is 5.5 nm in diameter and is globular. The sieves will separate the two proteins by taking advantage of their size difference. A DNA-hemoglobin solution will be passed through a sieve with nano-constrictions that only allow the smaller molecule, DNA, to pass through. This size specific method of separation can be used for separating various mixtures of proteins.

The average size of a protein is roughly 5-15 nm while the limit of standard lithographic techniques is roughly 20 nm. However, various materials can be deposited on a wafer with a thickness that is less than 5 nm. Such a layer can then be laterally etched using a wet chemical process producing a constriction in the nanometer scale. The thickness of a layer of material can be accurately controlled to make sieves that are specific to various sizes.

Figure 1: Fabrication Process

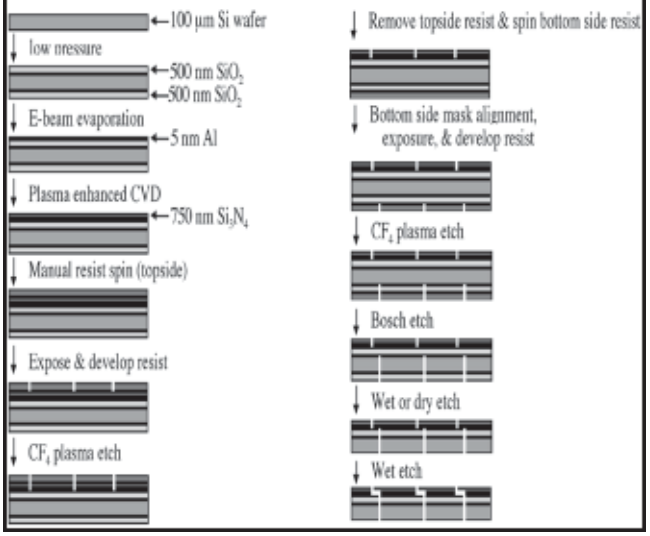

Applications:

Successful sieves can be used for separating proteins from a mixture according to size, e.g. DNA from hemoglobin. The microscopic size of the sieves allows for integration into chip-based devices, e.g. chips used for analyzing DNA: when analyzing DNA, a polymerase chain reaction (PCR) is first performed to amplify a DNA sample; however, hemoglobin inhibits the PCR process. The molecular sieves can be integrated in a DNA chip device to filter out hemoglobin before PCR is performed.

Procedure:

Figure 1 shows the process used to fabricate the sieves.

Results:

During the duration of the CNF REU program, we were able to complete the fabrication process up to the Bosch etch. Figure 2 is an SEM image of a cross-section of an etched wafer up to the Bosch etch step. The hole on the left is the bottom side hole. The Bosch process etched up to the SiO_2 layer and undercut the Si before the process was stopped. The smaller hole on the right is the topside hole and has reached the Al layer. Figure 3 is an image taken through an optical microscope of the topside of an etched wafer. The square on the left is the topside hole and the dark area on the right is the bottom side hole that can be seen through the Si_3N_4, Al, and SiO_2 layers.

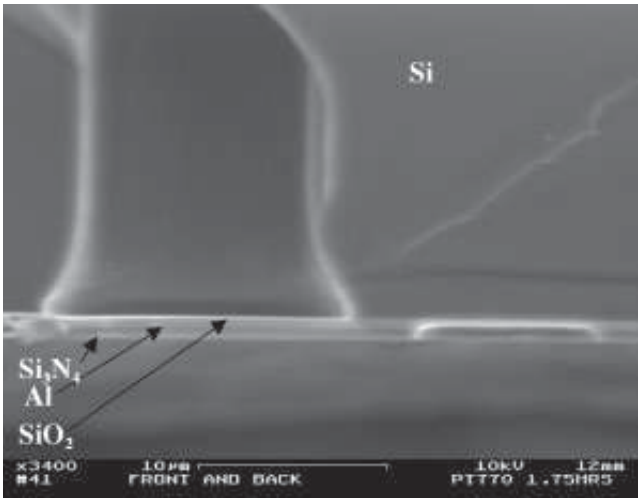

Figure 2: Top and bottom side etches (SEM).

Remaining Work for Fabrication:

In order to complete the fabrication of the sieves, the topside SiO_2 layer needs to be etched through vertically followed by a lateral etch of the Al layer. There are several approaches for accomplishing these last two steps of the fabrication process. One possibility is to use a wet etch process for both etches. To get through the SiO_2 layer, the chemical used must be highly selective to SiO_2 and not Si, Al, or Si_3N_4. To get through the Al layer, the chemical used must be highly selective to Al and not Si, SiO_2, or Si_3N_4. If these conditions are not met, the size of the nano-constriction produced by etching the Al layer cannot be well controlled. Another possibility is to use a dry etch process to etch through the SiO_2 layer. In this case, the selectivity issue would not be a problem for getting through the SiO_2 layer; however, using a dry etch process to etch at the bottom of such a relatively deep and narrow hole takes a substantial amount of time, making this option unpractical.

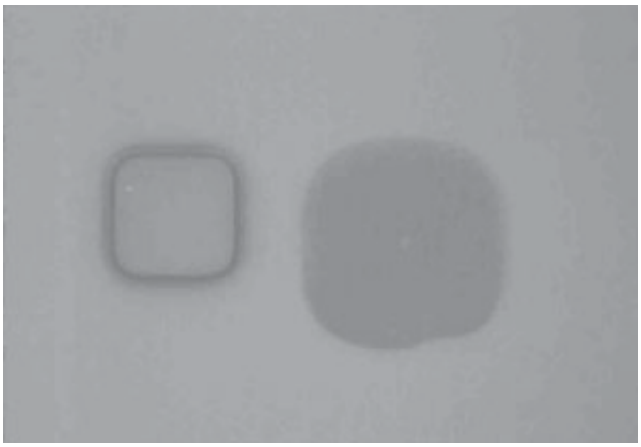

Figure 3: Top and bottom side etches (optical microscope).

Another possibility would be to eliminate the topside SiO_2 layer and replace the Si_3N_4 with SiO_2 (we need SiO_2 as a stopping layer for the Bosch process). However, this approach leaves Al exposed in the Bosch etch step and exposed metal in the Bosch etcher is not allowed at the CNF.

Further Developments: "Smart Sieves"

The silicon substrate will be grounded and metal electrodes will be inserted over each of the constriction paths of the sieves (Figure 4). These electrodes will be used to count the number of proteins passing through the sieves and also to exclude proteins of a certain polarity.

As a protein with a charge passes through the constriction path, a current is induced in the electrode. By detecting this current, proteins can be counted as they pass. Electrodes charged with a positive or negative potential can also be used to exclude correspondingly charged proteins.

Figure 4 shows a drawing of sieves that can separate negatively and positively charged proteins at the same time while simultaneously counting the number of proteins that pass.

Conclusion:

Although the REU program ended before completion of the sieves, work will continue on this project. After completion of the fabrication process, the sieves will be tested using filtration-testing techniques that have already been developed.

Acknowledgements:

Dr. Michael Spencer, Lori Lepak, Troy Richards, Nancy Guillen, the Spencer Group, CNF Staff, NBTC, NSF, and the 2002 CNF and NBTC REU Students.

References:

[1] Nelson, Cox. Lehninger Principles of Biochemistry, 3rd Edition. Worth Publishers, 2001.

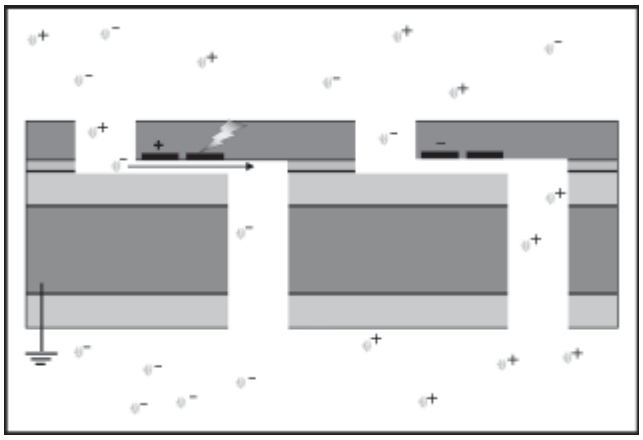

Figure 4: Smart Sieves.

Low Temperature Wafer Bonding and Bonding of Unconventional Materials

Nicole L. Schilling, Physics, Corning Community College

Vince Genova, Mandy Esch, Cornell Nanofabrication Facility, Cornell University

chipper_tink@hotmail.com, genova@cnf.cornell.edu, esch@cnf.cornell.edu

Abstract:

The main focus of this project was to bond wafers of materials previously considered nontraditional to the bonding process and to examine the effects of low annealing temperatures. The main strategies used in this study were direct bonding and anodic bonding.

Various trials were implemented involving unconventional materials such as Si_3N_4, GaAs and SiC as well as the more conventional Si and SiO_2. After bonding, these materials were subjected to low anneal temperatures and compared to more traditional anneal temperatures. Other variations in these trails included different chemical pre-treatments and plasma treatments. A comparison of bonding hydrophilic and hydrophobic surfaces was conducted to determine the effects of surface alterations caused by chemical and plasma treatments.

Following the bonding process, the total bonded area was analyzed to determine its effectiveness. Upon this qualitative analysis, a more quantitative approach was taken by using the blade insertion method to determine the surface energy and subsequently the bond strength.

The concept of wafer bonding is potentially useful in areas involving superconductivity, MEMs and various other fields. Bonding of unconventional materials at lower temperatures could thus open up a wide variety of possibilities regarding the application of wafer bonding.

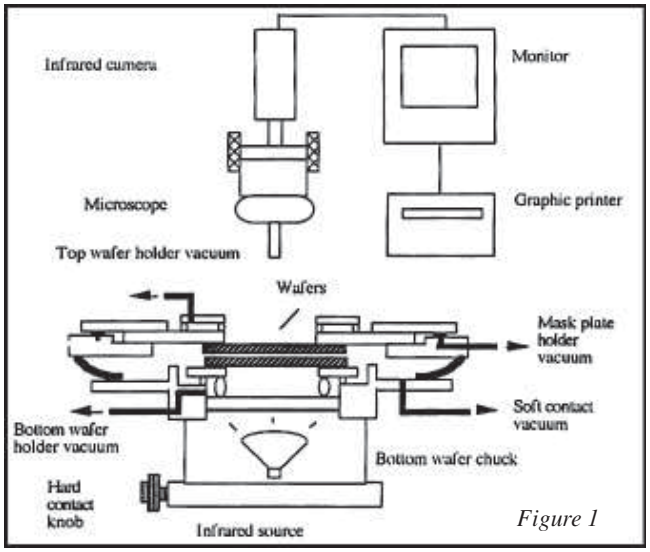

Figure 1

Introduction:

The main objective of this project was to analyze low annealing temperatures verses standard anneals of different bonded conventional and unusual materials. There were various comparisons of different chemically treated and oxygen plasma treated wafers, annealed at these lower temperatures as well as the standard temperatures. Surface alteration resulted from chemical treatments such as RCA 1 and HF dip as well as 75W, 100W, 150W and 350W power levels of plasma. The effectiveness of these variables was analyzed qualitatively by examining the post anneal bonded wafers and quantitatively using the blade insertion method to determine bond strength.

Procedure:

The first portion of this investigation involved the use of the EV-501 Bonder to perform direct bonding between a wide variety of materials. These materials incorporated the traditional Si and SiO_2, as well as more unconventional substances such as Si_3N_4, GaAs SiC, and oxide intermediate layers. Before the bonding process, each wafer was pretreated with oxygen plasma at power levels including 350W, 150W, 100W and 75W and chemically cleaned with an RCA 1. Most RCA chemical processes were a 1:1:5 NH_4OH, H_2O_2, and H_2O mixture performed at 65°C for approximately 10 minutes. However during some investigations, especially the Si_3N_4 and some GaAs trials, the mixture was a 1:1:20 ratio. The 1:1:20 ratio was implemented to minimize any induced surface roughening.

Periodically some wafers, excluding SiO_2, were dipped in HF before the RCA clean, resulting in a hydrophobic surface. Some wafers were also cleaned using Acetone and Isopropyl Alcohol as opposed to the RCA treatment. Furthermore, in one specific trial the chemical treatment was done before the plasma activation. Following chemical pre-treatment and thorough rinsing, the wafers were carefully dried using a nitrogen gun. Immediately before the bonding

process, the nitrogen gun was again used to remove any particulates.

The direct bonding procedure used a force of 1700N on the wafers for approximately 30 seconds. After this process, an IR lamp apparatus, similar to that shown in Figure 1 was used to show the bonded area. Once the bonded wafers were documented using the IR lamp, they were annealed. Almost every variation was performed twice in order to compare a standard one hour anneal at 1100°C, with a more unconventional 4 hour anneal at 350-450°C. The IR transmission method was used as shown by the apparatus to determine the effects of the anneal. The success of each trial was determined by estimating from the IR lamp pictures the bonded surface area and by the blade insertion method. A blade was inserted between the bonded wafers and the resulting fringe was measured to calculate bond strength as shown in Figure 2. From this, the success of each trial and variation would be able to be determined.

A similar procedure was used for the anodic process. The chemical and plasma pretreatments were performed as they had been in the direct process. Solvent cleans were used more frequently especially on glass. Materials such as Si, Si_3N_4, GaAs, SiC, and SiO_2 and Amorphous Si intermediate layers were bonded to glass. Various anodic parameters were set for each trial ranging from 150-350°C, 120N-1000N, and 150V-500V for 10 minutes. Following bonding, they were photographed using the IR apparatus and analyzed to determine the success of each trial.

Results:

Lower power levels of plasma tend to result in an increase in the percentage of bonded area when annealed at various temperatures for Si-Si direct bonds. This effect is less noticeable for Si-SiO_2 and even more so for the SiO_2-SiO_2 due to the increased amount of oxygen present at the bonding interface. Plasma activations after RCA cleans lead to decreased bond area and lower bond strengths for Si-Si and Si-SiO_2 bonds. High temperature anneals for short times are equivalent to low temperatures for long times for both hydrophilic and hydrophobic Si-Si direct bonds.

Regarding the anodic portion of the investigation, there is no apparent benefit from RCA cleans on glass. Plasma activation on Si and Si_3N_4 is as effective as an RCA for the Si-Glass and Si_3N_4-Glass trials. Plasma activation seems to be more effective than just the chemical treatment for the SiC-Glass series. In this case, plasma activation alone is better than the combination of plasma and chemical pre-treatments. For the Glass to Glass, with an intermediate layer of

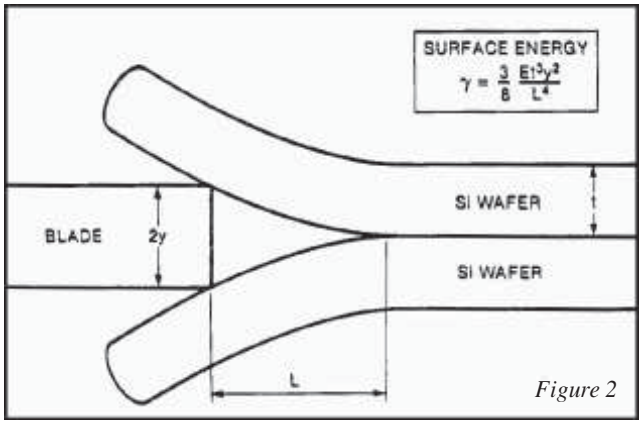

Figure 2

SiO_2, there is no apparent benefit from plasma treatment. For intermediate layers in general, there is concern regarding roughness, thickness, hydrogen concentration in the deposited layer and variations in anodic parameters.

Conclusions:

Based upon the results from this investigation, it can be concluded that thermal budgeting applies to direct bonds. The best direct bonds were achieved with Si and SiO_2. Plasma activation after an RCA clean is not favorable and should precede the chemical clean. The effectiveness of plasma activation depends upon the power level. Regarding the direct bonding of unconventional materials, Si_3N_4 bonded the best followed by GaAs and SiC. Regarding conclusions drawn from the anodic bonding trials, plasma activation works for SiC but not for the other materials. Furthermore, surface roughness plays a very important role especially for the intermediate layers.

Future work in this area might involve some of these same procedures used on patterned wafers. Also, further analysis of chemical treatments and annealing on rough intermediate layers may also be more thoroughly examined.

Acknowledgements:

I would like to formally acknowledge Vincent Genova, Mandy Esch, and John Triechler, as well as the CNF staff.

References:

[1] W. P. Maszara, G Goetz, A Gaviglia and J. B McKitterick, "Bonding of Silicon Wafers for Silicon-on-Insulator" J. Applied Physics 64(10) 15 Nov 1988.

[2] Q.-Y. Tong, U. Gosele, Semiconductor Wafer Bonding Science and Technology, John Wiley & Sons, Inc. 1999.

Growth and Characterization of Metal Nanocrystals

Kenneth Vampola, Electrical Engineering, University of California, Santa Barbara

Edwin C. Kan, Chungho Lee, Jami Meteer, Electrical & Computer Engr, Cornell University

kvampola@engr.ucsb.edu, kan@ece.cornell.edu

Abstract:

This report discusses the creation and characterization of metal nanocrystals. Metal nanocrystals are deposited on a film of thermal oxide grown on a silicon substrate. They are deposited by evaporating a layer of metal onto the oxide surface. The total energy of the film is reduced when the metal surface area is minimized by forming discrete, roughly spherical nanocrystals. Afterwards, the samples are annealed. The time and temperature of the annealing directly impacts the size and density of the nanocrystals. Longer annealing times and higher temperatures lead to the formation of larger but less numerous nanocrystals. The resulting nanocrystals were characterized by SEM imaging. Throughout this project, parameters such as the evaporated metal thickness, substrate doping type and level, annealing temperature and metal types were varied and the results compared. Finally, Calvin test structures were made to measure the contact resistance of an embedded metal nanocrystal structure.

Introduction:

Metal nanocrystals can be used in many applications. Their uses stem from their properties concerning tunneling and also taking advantage of the triple interface effect. In memory elements, a floating gate EEPROM device can be modified by replacing the floating gate with a layer of discrete nanocrystals. Because of their small size, tunneling into and out of the nanocrystals is made difficult according to the Colomb blockade effect. This will increase the memory retention time, allowing memory elements to become smaller.

It is obviously necessary to create a repeatable process for making nanocrystals and to be able to modify their size and distribution. In this research, variations on the processes were made and the resulting sizes and densities were recorded. In addition, various metals were used to make nanocrystals.

Another application of metal nanocrystals takes advantage of the triple interface effect. When a layer of nanocrystals is deposited on a surface and then surrounded by a metal, there is an area where all three materials come into contact with each other. At this point, the electric field lines are distorted. This should allow tunneling to occur from the metal layer into the surface with less of an applied bias. The effect is less contact resistance. However, since all the nanocrystals that have been measured have been roughly spherical, the area of the triple interface is limited to a single point at the bottom. To increase the triple interface area, a process was developed for creating nano-

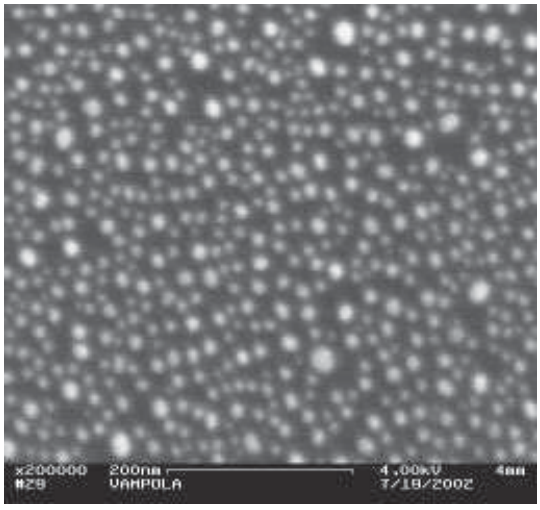

Figure 1: Gold nanocrystals annealed at 600°C with an initial thickness of 3nm viewed at 200,000X.

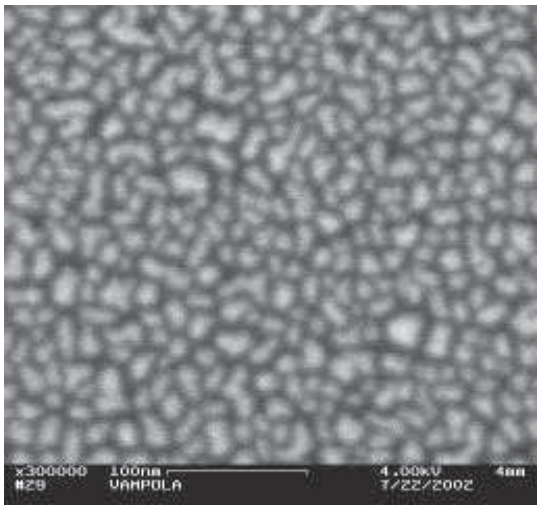

Figure 2: Wormy, gold nanocrystals un-annealed, with an initial thickness of 4nm viewed at 300,000X.

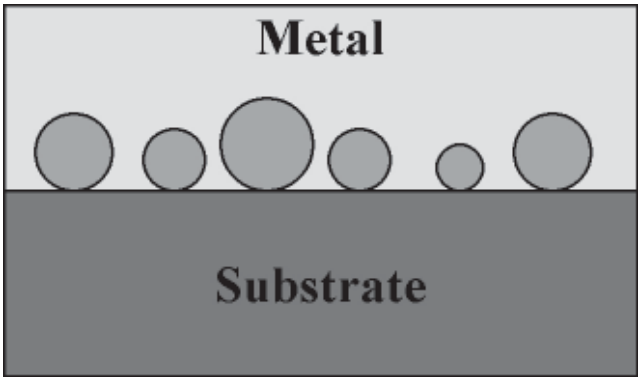

Figure 3: A contact resistance test structure cross-section showing the nanocrystals at the interface.

crystals that are wormy and not spherical in appearance. These nanocrystals should have more triple interface area. (See figure 2.) To test this theory, Calvin structures were made. (See figure 3.) These structures made a connection between a metal layer and the surface of a doped wafer. Nanocrystals were deposited at the interface of some of these structures. Also various batches used different metals and nanocrystals recipes.

Procedure:

The nanocrystals investigated here were metal and typically deposited on a thermal oxide on top of a silicon wafer. Initially, the wafers were un-doped, however, wafer doping was later introduced as a process variable. A thermal oxide was grown on the wafer. The oxide thickness was about 2 nm for a tunneling oxide and about 20 nm for an isolation oxide. Next, a thin layer of metal was deposited. The deposition was made by an electron beam evaporation. Either platinum or gold films were deposited on each wafer. The metal thickness ranged from 1.2 nm to 4 nm.

The samples which had a thicker deposited metal layer also had more numerous and larger nanocrystals than the samples with a thin layer of metal. However, if the initial layer was made too thick, nanocrystals formed a wormy layer (see figure 2), or did not form at all. Finally, the samples were annealed. Typical annealing temperatures were near the eutectic and the time was held constant at 10 seconds. The samples which were annealed at higher temperatures formed larger nanocrystals. Finally, the nanocrystals were observed with a SEM.

Results and Conclusions:

Metal nanocrystals were grown successfully in a repeatable fashion. Their sizes ranged from less than 5 nm to greater than 20 nm in diameter. The distribution of the sizes approximately fit a Gaussian curve. (See figure 4.) The process worked for gold and

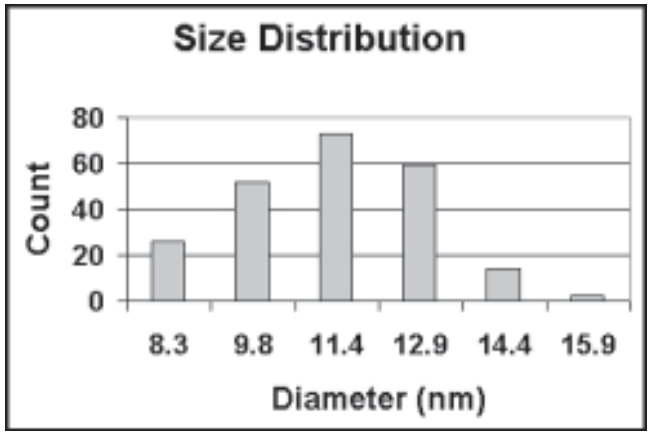

Figure 4: The size distribution of platinum nanocrystals annealed at 900°C with an initial thickness of 1.3 nm.

platinum. The thickness of the metal had a direct impact on the nanocrystal size, as did the anneal temperature. However, the effects of substrate doping were not represented by a strong trend and were inconclusive. More research is needed to determine the relationship between the substrate doping type/amount and the nanocrystal distribution created. Also, a procedure was developed for creating a wormy nanocrystal structure using thick layers of deposited gold. Finally, the resistance test structures were created and the contact resistance was observed to decrease by more than two orders of magnitude.

Acknowledgements:

Many thanks go to Edwin Kan, my principal investigator and to my mentors, Chungho Lee and Jami Meteer. My work was only possible by their help, patience and expertise.

References:

[1] Narayanan, Liu, Shen, Kim, Kan - in IEDM Tech. Digest pp 87-90 May 2000.

[2] V. Narayanan, Z. Liu, Y. N. Shen, M. Kim, and E. C. Kan, “Reduction of metal-semiconductor contact resistance by embedded nanocrystals”, IEDM, pp. 4.5.1-4.5.4, 2000.

[3] Z. Liu, M. Kim, V. Narayanan, and E. C. Kan, “Process and device characteristics of self-assembled metal nano-crystal EEPROM”, superlattices and microstructures, vol. 28, No. 5/6, pp. 393-399, 2000.

[4] Z. Liu, C. Lee, G. Pei, V. Narayanan and E. C. Kan, “Eluding metal contamination in CMOS front-end fabrication by nanocrystal formation process”, Mat. Res. Soc. Symp. Proc. Vol. 686, pp. A5.3.1-A5.3.6, 2002.

Characterization of Lift-off Material using Standard Photolithography Process

Sara Yazdi, Chemical Engineering, University of Massachusetts-Amherst

Garry Bordonaro, Michael Skvarla, Daniel Woodie, Cornell Nanofabrication Facility, Cornell University
syazdi@ecs.umass.edu, bordonaro@cnf.cornell.edu, skvarla@cnf.cornell.edu, woodie@cnf.cornell.edu

Abstract:

This project is intended to characterize the process performance of a lift-off material. Metal lift-off is a method used to generate conducting metal structures on a substrate. Conventional metal lift-off is done using a chlorobenzene dip or image reversal.

Chlorobenzene dip poses health and safety concerns because of the hazardous nature of the chemicals, and the image reversal method proves to be highly time consuming. This project does not rely on either method, and optimization of the proposed process provides a cost-effective and simpler alternative to the conventional techniques of metal lift-off.

In this process, four-inch silicon wafers are spun with lift-off material and coated with photoresist. The photoresist is exposed using a stepper; during the development step the lift-off material is dissolved away, resulting in an undercut profile and allowing successful metal lift-off. The resulting bi-layer is inspected using optical microscopy and scanning electron microscopy (SEM). Bake temperature/ duration, exposure sensitivity, adhesion and ease of removal are the critical factors considered in this project.

Introduction:

Metal-lift off has long been known as a method to generate metal patterns on a substrate. The conventional methods of metal lift-off include Chlorobenzene dip and the image reversal method. The Chlorobenzene dip method functions by hardening the top surface and causing the two layers to have two different dissolution rates. More specifically, the lower layer has a faster dissolution rate than the top, resulting in an undercut. Chlorobenzene use poses many health concerns. According to the Environmental Protection Agency, long exposures to Chlorobenzene can cause an adverse effect on the central nervous system, blood cells, bone marrow and liver tissues.

There are several proposed methods to perform image reversal, but amongst the most common ones are direct and indirect image reversal. In direct image reversal, an acid-catalyzed organic reaction results in creation of a three-dimensional insoluble polymer network, which ultimately causes a difference in dissolution rates. In contrast, the indirect image reversal is a base-catalyzed organic reaction in which the dissolution inhibitor turns into a dissolution enhancer [1].

Both above methods pose either health and safety concerns or they are highly time consuming with many parameters to control. The method discussed in this paper has the advantage of deposition of a discontinuous metal film, and provides a much safer approach to lift-off process.

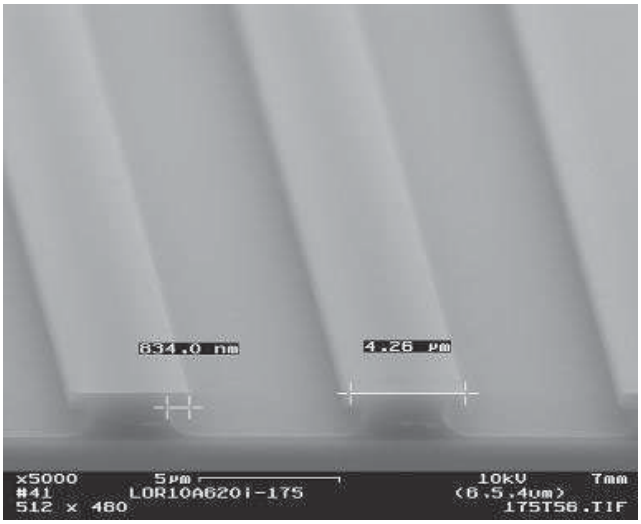

Figure 1, above: Significant undercut using LOR-10A, and 620-7i resist.

Figure 2, below: 3 µm structure, LOR-10A and 620-7i on top.

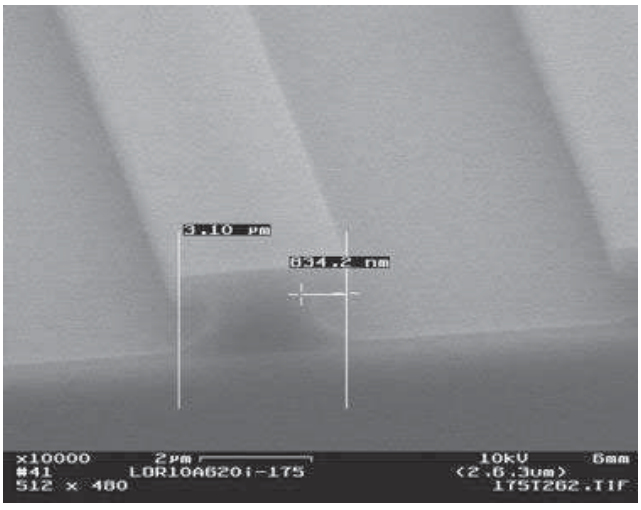

Procedure:

Lift-off resist is a new chemically modified PMGI (polydimethylglutarimide) resist with a glass transition temperature of 1900°C. There are two types of lift-off resist: LOR-A and LOR-B. LOR-A has a lower dissolution rate so it is ideal for thin film processing, whereas LOR-B has a higher dissolution rate so it is more suitable for thick film processing. Time limitations only allowed study of LOR-A series — more specifically, LOR-10A with a viscosity of 74.45 centistokes and solid content of 10.5%.

A layer of lift-off resist was deposited on four-inch silicon wafers using static dispense at a primary speed of 500 rpm for 3 seconds, then reaching a final drying speed of 3000 rpm for 45 seconds. Next, the wafers were baked on hot plate at 175°C for 5 minutes. In the next step, a layer of preferred resist is deposited. Depending on the chemical nature of the resist, the appropriate spin speed/duration was used. The exposure was done using the 10X-stepper with a minimum resolution less than 0.6 µm. For the purposes of this research, an i-line resist, 620-7i, was used. It was spun using static dispense at 3000 rpm for 45 seconds, and baked at 170°C for 60 seconds.

Exposed wafers were inspected using the optical microscope prior to using the scanning electron microscopy. SEM LEO 982 was used to inspect the resist profiles and the undercuts. Figure one is an image of the significant undercuts using LOR-10A.

Results and Conclusion:

Extensive evaluation of the line-width control was not possible in the time frame of this project. Studies showed that the amount of undercut is independent of the focus and exposure used, thus providing users with a large process window. Regardless of the focus and exposure, the undercut fluctuated around 1 µm, as can be seen in figures 2 and 3. In order to study the effects of temperature on LOR's bulk removal rate, several samples were prepared at a temperature range of 165-185°C. Each sample was prepared at nearly identical bake duration and conditions. The samples were developed using the 300 MIF-0.262 N in two steps of 30 seconds, each of which were followed by inspection using Filmetric measurements.

Collected data points (graph 1) showed an overall increasing rate of removal as the temperature decreased. Future characterization of LOR would include studying the variations in behavior due to changes in viscosity and its impact on the lowest attainable feature size. Also, the LOR's compatibility with different developers and photoresist should be explored.

Acknowledgments:

I would like to thank Garry Bordonaro, Michael Skvarla and Daniel Woodie for their dedication and guidance during the course of this project. I also would like to acknowledgle Melanie-Claire Mallison whose efforts made the program possible.

References:

[1] Dammel, Ralph. Diazonapthoquinone-based Resist. Washington: SPIE Optical Engineering Press, 1993.

[2] Environmental Protection Agency, OPPT Chemical Fact Sheets, Chlorobenzene CAS No.108-90-7, January 1995, http://www.epa.gov/opptintr/chemfact/chlor-fs.txt

[3] Microchem Corp. Lift-Off resist data sheet, Copyright 2002 http://www.microchem.com/products/pdf/lor_data_sheet.pdf

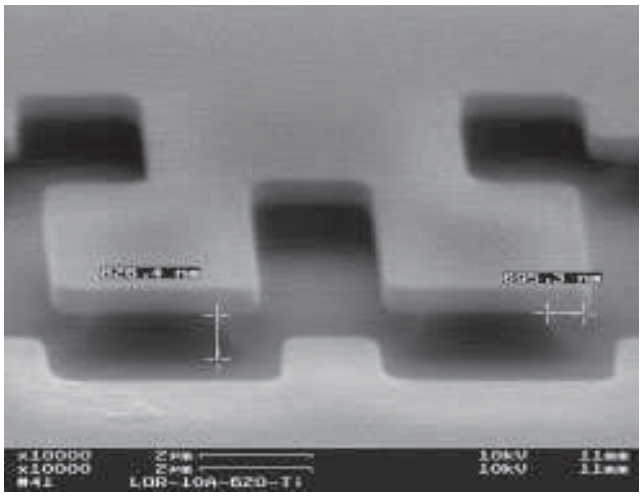

Figure 3: 4 µm structure, LOR-10A and 620-7i on top.

Graph 1: Dissolution rate vs. Temperature for LOR-10A, the bulk removal rate decreases as the temperature increases.

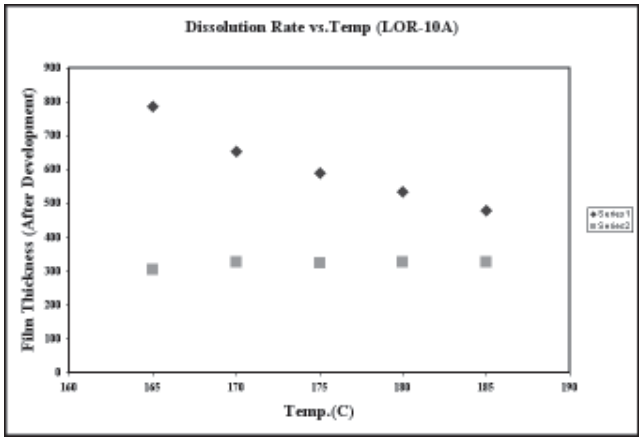

Materials Science Research Center of Excellence

Howard University, Washington, DC

http://www.msrce.howard.edu

2002 Howard REU Interns

NNUN REU Intern	School Affiliation	Principal Investigator
From Left to Right:		
Ms. Veronica Valeriano	University of Washington	James Griffin
Mr. William Rose	MSRCE, Howard University	REU Principal Investigator
Mr. Jason Smeltz	Penn State Capital Campus	Gary Harris
Ms. Yvette Williams	MSRCE, Howard University	REU Coordinator
Ms. Karrie Houston	Howard University	Kimberly Jones
Mr. James Griffin	MSRCE, Howard University	REU Principal Investigator
Mr. William Whitaker	Bakersfield College/UC Berkley	Juan White

Increasing Ion Rejection in Nanofiltration Membranes

Karrie D. Houston, Chemical Engineer, Howard University

Dr. Gary Harris, Dr. Kimberly Jones, Mr. James Griffin, MSRCE, Howard University

karriehouston@hotmail.com, gharris@msrce.howard.edu

Abstract:

A novel method for modifying polymeric membranes to render them less susceptible to fouling and flux decline involved increasing electrostatic interactions at the membrane surface. This electrostatic interaction was increased by using an ion implantation process. This technique transmits large doses of ions into the thin active layer of a nanoporous membrane. The energetic ions bombard and penetrate the nanofiltration membrane surface, interacting with the substrate atoms in the polymeric skin. As a result, a fixed permanent charge is induced on the surface, producing a static electric field within the pores. The interaction of charged particles with the resultant electric field should optimize flux and rejection by increasing electrostatic repulsion between co-ions.

This study was designed to investigate the effects of ion implantation and its ability to modify polymeric membranes to efficiently reject targeted ions while decreasing fouling.

Introduction:

Recently, nanoporous materials have gained remarkable attention for their significant advancement in membrane technology. A membrane is a thin layer of material that is capable of separating material as a function of physical or chemical properties when coupled with an applied driving force. This driving force may be in the form of pressure, electric potential, or difference in concentration. Nanofiltration membranes can be constructed of thin film composites of polymers, consisting of negatively charged chemical groups, with an average pore size of one nanometer.

Although nanofiltration membrane-based separations are efficient in the filtering process, they have been limited in application because of membrane fouling. Fouling is characterized as material deposited on the membrane surface or within the pores, thereby decreasing flux and membrane rejection. Consequently, industries incur additional expenses in an attempt to eradicate membrane fouling.

In an attempt to eliminate fouling and its effects, the process of ion implantation was incorporated. Ion implantation utilizes high energetic beams of ions to modify surface structure and chemistry. Through ion implantation, the charged density of the membrane is increased, which increases electrostatic repulsion of co-ions. Electroneutrality will subsequently ensure rejection of counterions.

This study attempted to use ion implantation of charged membranes to overcome the hindrances of membrane fouling and increase rejection of monovalent ions. The nanofiltration membranes were polyamide and cellulose acetate which were tested with sodium sulfate ($Na_2(SO)_4$), calcium chloride (CaCl), and sodium chloride (NaCl) solutions.

Theory:

The formula $R = 1 - (C_p/C_f)$ was used to calculate the rejection percentage. The C_p signifies the concentration of the permeate, which was achieved through Atomic Absorption Analysis. The term C_f signifies the concentration of the solution feed, which was 0.01M for all salt solutions.

Procedure:

The experiment was conducted in two segments. The first segment involved the testing of flux and rejection in the uncharged polyamide and cellulose acetate membranes. The second segment involved the same analysis, however, with the substitution of the ion implanted membranes (ion species: fluorine; ion energy 10keV; ion dose: 1×10^{10}). Each membrane received one experimental run for each of the three salt solutions ($Na_2(SO)_4$, $CaCl_2$, NaCl) at a pressure of 80 psi. All membranes were soaked in de-ionized water for two hours before experimental use.

A "pre-trial" run was completed to ensure the usefulness of each membrane. After the equipment was washed with de-ionized water, the experimental set-up was assembled and the reservoir was filled with ultra pure water. The flux was measured at thirty-minute intervals. At the end of two hours, the flux readings were compared. If the flux measurements were consistent, the membrane was considered undamaged and therefore suitable for testing.

All three salt solutions were prepared at 0.01M concentration. A selected membrane was cut in a 43 mm circle and placed at the bottom of the Amicon 8000 stirred cell module. The stirred cell holder was assembled and placed in the Amicon 8050 stirred cell holder, which mounted on a magnetic stirrer. The prepared salt solution was poured into the 6-liter stainless steel reservoir. The carrier gas (N_2) was connected through teflon tubing to the inlet of the reservoir. A second tube from the outlet of the reservoir was connected to the inlet of the stirred cell module. The magnetic stirrer was programmed for a setting of five to six to ensure uniformity.

Next, the valve of the carrier gas was opened, allowing the tank to expel nitrogen gas to the inlet of the reservoir. The solution entered the cell module, where it was filtered and collected. The flux rates were measured and recorded every thirty minutes. This procedure was repeated for all three salt solutions at the same pressure.

Results:

In figure 2, filtration of the unmodified cellulose acetate membrane produced the following rejections: sodium chloride, 50.86% (Na), 90.31% (Cl); calcium chloride, 84.02% (Ca) and 78.62%(Cl); sodium sulfate 99.08% (Na). The unmodified polyamide membrane produced the following results: sodium chloride, 66.90% (Na), 90.26% (Cl); calcium chloride, 47.94% (Ca), 50.10% (Cl); sodium sulfate 76.72% (Na).

In figure 1, filtration of the modified cellulose acetate membrane produced the following results: sodium chloride, 40.05% (Na), 30.85% (Cl); calcium chloride, 38.88% (Ca), 41.10%(Cl); sodium sulfate, 72.53%; The modified polyamide membrane results were: 41.62% (Na), 31.85% (Cl); 73.78% (Ca), 73.36% (Cl); sodium sulfate, 97.26% (Na).

References:

[1] Spire Biomedical - Technology Overview - Ion Implantation. http://www.spirebiomedical.com/Biomedical/ionimpl.html

[2] Koros, WJ, Ma, YH, Shimidzu, Y., "Terminology for Membranes and Membrane Processes", IUPAC, 1996.

[3] Merry, Alan. "The Right Membrane for the Job." PCI Membranes; Laverstoke Mill, Whitchurch, Hampshire, RG28 7NR, UK. Jan/Feb 2001.

[4] Raman, L.P., Cheryan, M., Rajagopalan, N. "Consider Nanofiltration for Membrane Separations" Chemical Engineering Progress. March 1994.

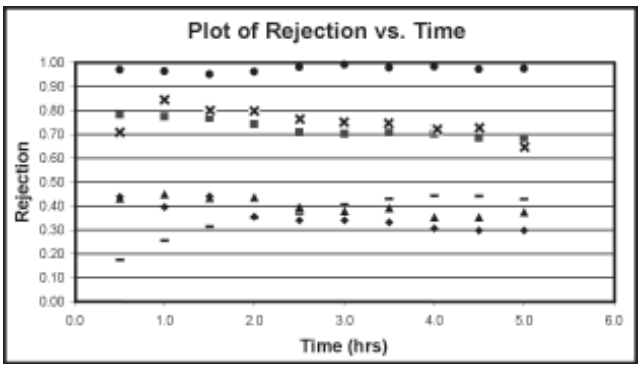

Figure 1: Rejection rates for modified membranes.

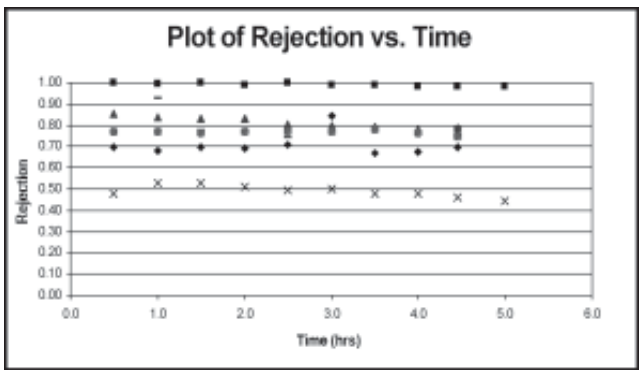

Figure 2: Rejection rates for unmodified membranes.

Design and Creation of a SiC High-Temperature pH Sensor

Jason Smeltz, Electrical Engineering Technology, Penn State

William Rose, EE & Materials Science Research Center of Excellence, Howard University

jes354@psu.edu, rose@msrce.howard.edu

Abstract:

The creation of a silicon carbide (SiC) pH sensor for operation in harsh environments has been investigated. Silicon pH sensors which are currently used in industry have two main drawbacks. They are; low temperature operation and inability to withstand harsh environments. Silicon pH sensors are not accurate over 150°C. Silicon will not resist corrosive conditions without failing.

We grew a silicon dioxide layer onto both silicon and silicon carbide substrates and characterized them. The layers were characterized using both current-voltage (I-V) and capacitance-voltage (C-V) and ellipsometry.

MOS capacitors created on the SiC carbide exhibited good behavior, indicating their potential usefulness as a ion sensitive field effect transistor (ISFET).

Introduction:

Measurement of pH, also known as the "power of hydrogen" is the measure of the acidity or alkalinity of a solution. It is defined as:

$$pH = - \log [H^+]$$

Currently there are two different ways of measuring pH. The most common is with test strips. These are pieces of paper with chemicals on them that change to a certain color depending on the level of the pH in the solution under test. The current measuring device uses a metal oxide semiconductor field effect transistor (MOSFET) on a silicon sample to measure the pH level. This device is much more expensive than the strip method but is also reusable. The problem with this device is that at temperatures of 150°C the device will fail due to the fact that it is built on silicon. Silicon also will not hold up when exposed to harsh environments such as strong acids and bases.

SiC was the chosen material for a pH sensor for three main reasons. First, SiC is a wide band gap material. This allows it to withstand high temperatures. Second, it is physically hard and third, it is chemically inert. Therefore, in situations where pH has to be measured in high temperature or harsh environments, a SiC pH meter would be particularly useful.

An ion sensitive field effect transistor (ISFET) is a MOSFET in which the channel is controlled by the ions in the solution under test. The ion concentration in the solution is directly related to the pH of the solution. An example of a typical MOSFET and ISFET can be seen in Figure 1. Note that the channel of the MOSFET is regulated by voltage while the channel of the ISFET is regulated by the ions in the solution being measured.

A picture of what an ISFET on silicon carbide in a liquid solution would look like can be seen in Fig 2.

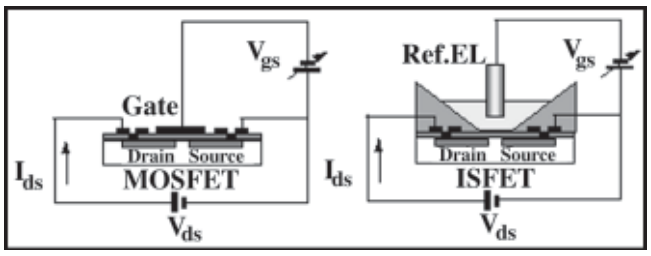

Figure 1: Normal MOSFET compared to ISFET.

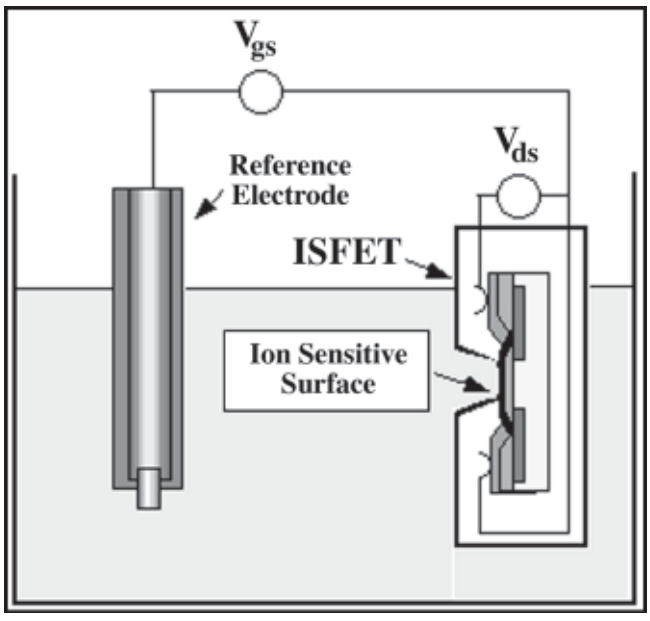

Figure 2: Schematic representation of an ISFET pH measuring system.

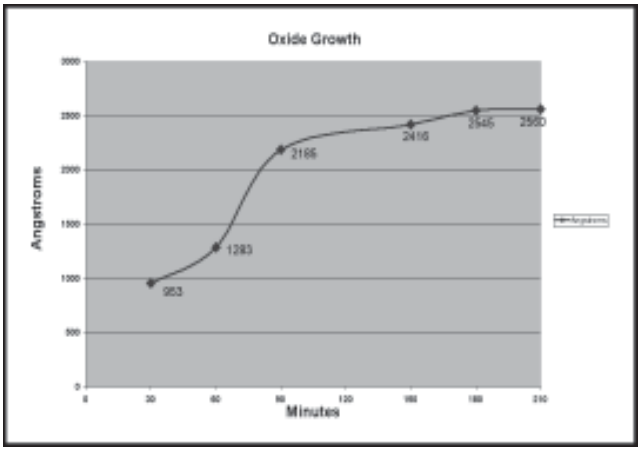

Figure 3

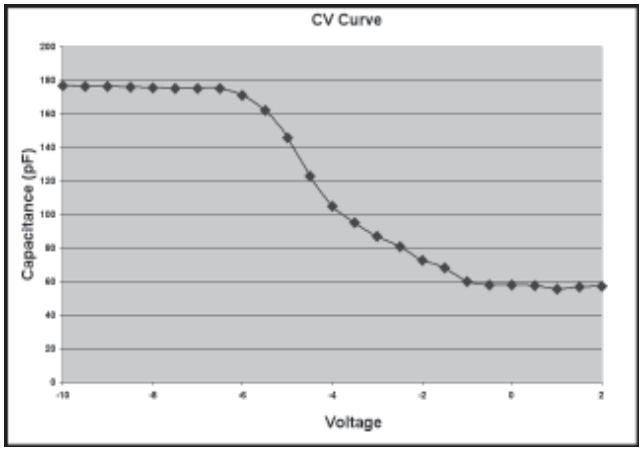

Figure 4

Experiment:

The first step of the process was to clean each piece of silicon carbide and silicon. This was done using a standard RCA cleaning procedure. This ensured that the surface was completely clean going into the furnace for oxide growth. Oxides were grown on silicon for different time periods to determine oxide growth rates. The temperature at which the oxides were grown was 1100°C. The thickness of the oxides were determined by comparing their color to the growth chart, and then verified by ellipsometry. The growth rate can be seen in Figure 3.

The next step was to create a MOS device. A MOS capacitor was made by evaporating 2000 µm of aluminum dots, using a metal mask, onto the oxide surface. We also tried making them with a mixture of aluminum and silicon. The backside of the wafer was then fully covered with 2000 µm of aluminum. Before characterizing the devices, we annealed the samples to create ohmic contacts to the back surface.

To characterize the samples, we used a HP characterizing system. From this, we were able to plot the capacitance verses voltage. This chart can be seen in Figure 4. By examining the chart we can conclude that the device went through accumulation, depletion and inversion.

Results and Conclusion:

The first key step of the design of a high temperature pH sensor is to become familiar with the growth of oxide. To do this, many runs on the furnace were required to know the rate of growth. When charting the capacitance versus the voltage, we found that the smaller oxide levels seemed to repeatedly have the best C-V curve. The most conclusive information from the C-V chart was that the MOS capacitor on the silicon carbide sample went through accumulation, depletion and inversion. This proves that silicon carbide samples can be used to create an ISFET. Unfortunately, due to time restraints this summer, an actual ISFET was not fabricated on silicon carbide. However, from the data that we collected, the creation of an ISFET on silicon carbide for use as a high temperature pH sensor is feasible.

Acknowledgements:

Thank you to the Howard MSRCE, especially William Rose and Crawford Taylor for their contributions to my research, the funding provided by the NNUN and NSF, and everyone else who was a part of one of my most unforgettable summers.

References:

[1] Sentron Europe BV.
[2] Myron L Company.

Characterization of GaAsN and InGaAsN

Veronica Valeriano, Electrical Engineering, University of Washington

Gary L. Harris, Ph.D, Mr. James Griffin, MSRCE, Howard University

gharris@msrce.howard.edu, griffin@msrce.howard.edu

Abstract:

The addition of 1-2% nitrogen to gallium arsenide (GaAs) and indium gallium arsenide (InGaAs) significantly reduces the materials' bandgap, and this discovery is of great interest for opto-electronics and solar cell applications. Test samples of gallium arsenide nitride (GaAsN) and indium gallium arsenide nitride (InGaAsN) alloys have been grown using molecular beam epitaxy (MBE) with different doping types and concentrations. The dopants used in this study were silicon for n-type and beryllium for p-type. The characterization process involved the use of Van der Pauw Hall measurements. Hall measurements were taken at various temperatures over the range of 77K to 473K to determine the activation energies of the dopants. The activation energies were calculated from the slope of the carrier concentration versus the temperature curve.

Introduction:

GaAsN and InGaAsN have been the focus of semiconductor research in recent years due to their remarkable properties. These alloys demonstrate large bowing in the band gap energy with the incorporation of only a few percent of nitrogen. For example, when 2% nitrogen is added to GaAs, the material's bandgap decreases from 1.43eV to about 0.4eV [1, 2]. Furthermore, InGaAsN alloys can be lattice matched to GaAs by varying the nitrogen content.

This research investigates the electrical characteristics of the two alloys under different temperatures, ranging from 77K to 473K. This process is governed by the Hall effect and uses the Van der Pauw technique in performing the measurements. The Hall effect is based on the Lorentz force, which is induced when current is passed thru a conducting material and a magnetic field is applied perpendicular to both the surface of the material and the direction of current flow. A voltage difference (Hall voltage) is produced across the material, which is described by the equation: $V_H = \frac{IB}{ned}$

The following equations are used to calculate the corresponding electrical properties:

$$\text{Mobility} \quad \mu = [\overline{\Delta v}/\overline{V}]*[\ln 2 * 10^8/\pi B(gauss)] \qquad cm^2/V-s$$

$$\text{Sheet Resistance} \quad \rho_s = [\pi/\ln 2]*[\overline{V}(volts)/I(amperes)] \qquad \Omega/square$$

$$\text{Resistivity} \quad \rho = \rho_s * d(cm) \qquad \Omega - cm$$

$$\text{Carrier Concentraiton} \quad n = 1/[q*\mu*\rho] \qquad 1/cm^3$$

where $\overline{\Delta v}$ is the average measured hall voltages and $\overline{V}$ is the average measured hall voltages after applying a magnetic field, d is the thickness of the conducting layer, and q is the electron charge. Here, the carrier concentration is what we ultimately need to calculate the activation energies.

GaAsN			InGaAsN		
Sample Name	Thickness	Carrier	Sample Name	Thickness	Carrier
M1910	.45mm	$n=2x10^{-17}$	M1929	.66mm	$n=8x10^{-18}$
M1911	.45mm	$n=6x10^{-18}$	M1930	.625mm	$n=4x10^{-17}$
M1912	.45mm	$p=9x10^{-17}$	M1931	.64mm	$p=8x10^{-18}$
M1913	.75mm	$p=2x10^{-18}$	M1932	.59mm	$p=5x10^{-17}$

Table 1

Experiment:

MBE was used to grow eight samples on GaAs substrates, four for each of the two alloys. Silicon was used as the dopant for the n-type samples and beryllium was used for the p-type samples. The thickness, carrier concentrations and the approximated depletion layers are shown in Table 1. Square pieces with side lengths of about 0.375″ were cleaved from the samples. A clover leaf mask and sand-blaster were then used to pattern the Hall samples, and metal contacts were placed on the periphery of the four leaves by evaporation. For the n-type samples, the contacts were made of Ge/Au/Ni with thickness 200Å/3000Å/200Å and the substrates were annealed at 450°C for 1 min. The p-type contacts were made of Cr/Au with thickness 200Å/2000Å and annealed at 430°C for also 1 min. A curve tracer was used to test the linearity of the contacts to ensure ohmicity.

Hall Measurements:

The Hall measurement apparatus consists of the following (shown in figure 1): electromagnet, current source, digital multimeter, digital thermometer, switch (used to switch the direction of current), calculator (programmed), and printer.

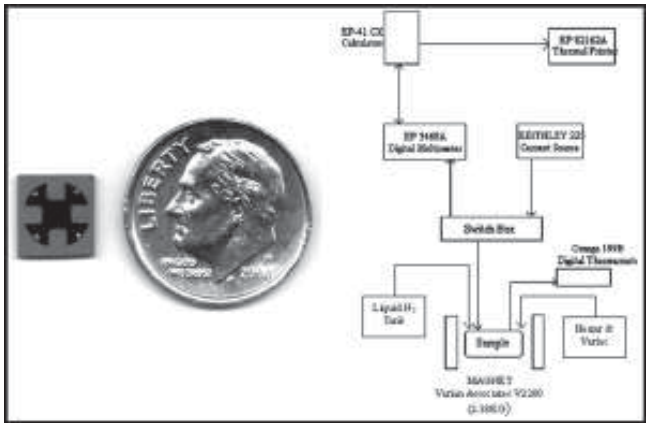

Figure 1: Hall sample and measurement apparatus.

A sample was positioned on the probe so that there was good contact, which was indicated by a value near zero read by the multimeter. The probe was then set in a tube between the magnet, making sure that the face of the sample was perpendicular to the magnetic field. The calculator program was executed. The data obtained is given in Table 1.

Results:

Calculation of Activation Energy:

$$n \cup \frac{1}{\sqrt{2}}(N_D N_C)^{\frac{1}{2}} \exp(-\frac{E_D}{2kT})$$

convert to the form $y = mx + b$

let $A = \frac{1}{\sqrt{2}}(N_D N_C)^{\frac{1}{2}}$

then

$$\ln(\frac{n}{A}) = \log_e(\frac{n}{A}) = -\frac{E_D}{2kT}$$

$$\log_e(n) - \log_e(A) = -\frac{E_D}{2kT}$$

$$\frac{1}{\log_{10} e}[\log_{10} n - \log_{10} A] = -\frac{E_D}{2kT}$$

$$[\log_{10} n - \log_{10} A] = .434(-\frac{E_D}{2kT})$$

$$x = \frac{1}{T}, m = .434(-\frac{E_D}{2k})$$

$$E_D = 2mk(\frac{1}{.434})$$

At liquid nitrogen temperatures and below, carriers are said to freeze out or to be in their lower energy levels. As the temperature rises, energy is imparted to the carriers causing them to make transitions to higher energy levels. Our aim is to freeze out the carriers and measure the concentration as the temperature rises. From these values, we will be able to calculate and determine the activation energy for the carriers of the dopants. On the left is the derivation of the equation used to calculate the activation energy. Using this equation, the activation energies were plotted vs. 1000/T as shown below.

Discussion:

Freeze out of the dopant carriers occurs in the lower temperature range. Thus, only values from 8 to 12 were used to calculate the activation energies. Best-fit lines were used to calculate the slopes of the graphs. For GaAsN, the ionization energies are E_d = 0.0018 eV for silicon in GaAsN (n-type) and E_a = 0.0094 eV for beryllium in GaAsN (p-type).

Due to a the shortage of time, the InGaAsN was not tested. Future works on this material are photoluminescence and the fabrication of high mobility transistors to investigate the possibility of detecting a 2-dimensional electron gas between AlGaAs/GaAsN and AlGaAs/InGaAsN layers.

Acknowledgements:

Thanks to the Howard Materials Science Research Center of Excellence especially to James Griffin, Juan White, Dr. Harris, and Crawford Taylor and the rest of the Howard crew (you know who you are) for the support, guidance and a mind-tickling, unforgettable summer. Funding was provided by NNUN and NSF.

References:

[1] Buyanova, I.A., W.M. Chen, and B. Monemar. "Electronic properties of Ga(In)AsN alloys." MRS Internet Journal of Nitride Semiconductor Research. Volume 6, Article 2. July 2002 <http://nsr.mij.mrs.org/6/2/complete.mac.html>

[2] "InGaAsN Looks Promising As Very Efficient Photovoltaic Power Source." Electronic Design 17 Apr. 2000: 25-26.

[3] Semiconductor Electronic Division, EEL Technical Activities. National Institutes of Standards and Technology. July 2002 <http://www.eeel.nist.gov/812/hall.html>

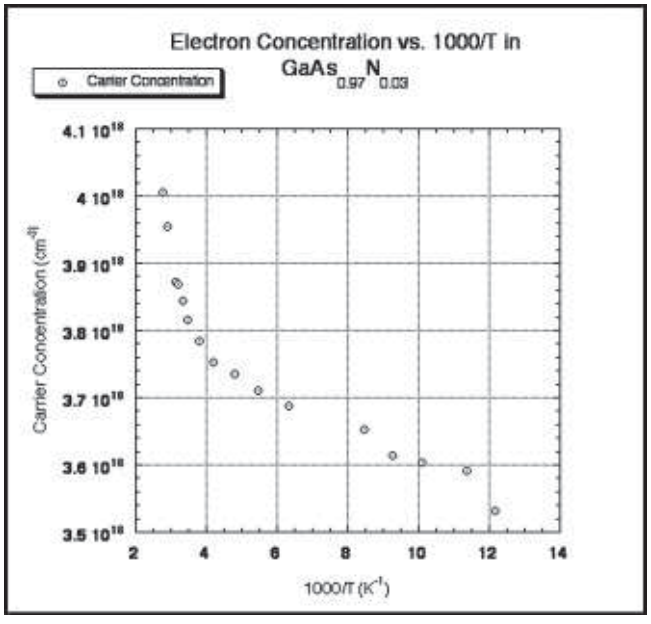

n-type sample

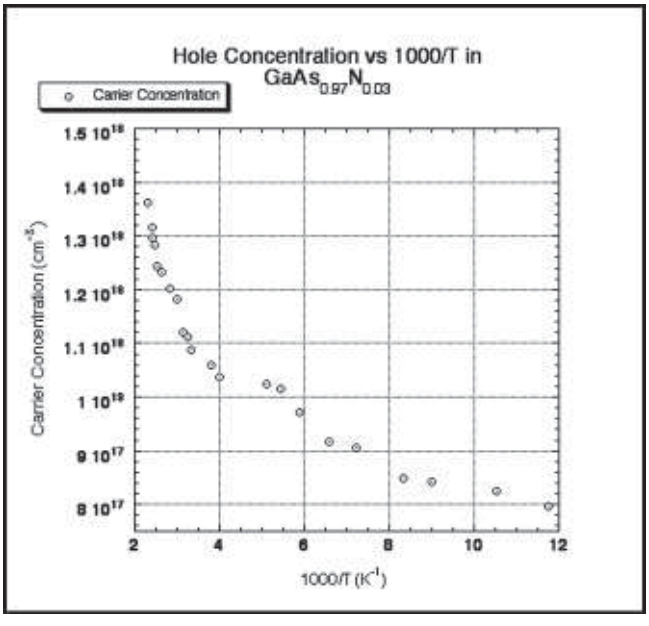

p-type sample

Self-Assembling Diblock Copolymers as Masks for Reactive Ion Etching

William Whitaker, Computer Engineering, Bakersfield College

Gary Harris, Director, James Griffin, Senior Research Associate, MSRCE, Howard Univ

billwww@pacbell.net, gharris@msrce.howard.edu, jagriffin@howard.edu

Abstract:

Certain diblock copolymers, when applied as thin films, can be induced to "self-assemble" into films containing uniform geometric shapes on the mesoscale. These thin films provide a means of creating masks with structures smaller than the limits of current lithography techniques.

The project objective concerned the formation of a copolymer mask, containing a uniform dot array, adhered to a silicon substrate. A diblock copolymer composed of polystyrene and polymethylmethacrylate (PS/PMMA) was annealed on a silicon substrate. By varying parameters (deposition spin speed, anneal times, and substrate surface treatments), a process for inducing self-assembly in PS/PMMA with M_w= 67 kDa was determined. The diblock copolymer formed cylindrical columns of polymethylmethacrylate ~ 20 nm in diameter with a spacing of ~ 45 nm in a field of polystyrene. The PMMA columns were selectively removed leaving a polystyrene mask with uniformly spaced holes or a "dot array." The same technique was then employed to place a diblock copolymer mask on the surface of a silicon carbide substrate.

Introduction:

The key to obtaining self-assembling morphology in diblock copolymers is controlling surface interactions. Two surface interfaces exist for the diblock, one at the substrate/polymer interface and one at the polymer/air interface. Both blocks of copolymer must not experience a propensity to move preferentially to either surface interface. If one end of the diblock chain experiences a greater affinity for either of the surface interfaces, a layering effect may manifest as the copolymer system moves toward a minimum energy state. Additionally, contact angles must be relatively equal for both copolymers at the substrate interface, where each block of the diblock copolymer experiences the same relative affinity for the surface. These surface interactions can be controlled with surface treatments applied to the substrate. With the surface interactions equalized, the deposited diblock copolymer, when heated well above the glass transition temperature, self-assembles into mesoscopic domains.

Experimental Procedures:

All substrates used were cleaned by the following method: 15 second brush w/detergent, 3 minute ultrasound in trichloroethylene, 3 minute ultrasound in acetone, and 3 minute ultrasound in methanol.

Two methods of surface treatments were used for surface passivation. Both methods have been described by Thomas Russell at the University of Massachusetts.

The first method was an endeavor to passivate the surface of a <100> silicon substrate by removing the native SiO_x layer. Oxide removal was accomplished by submerging substrates in hydrofluoric acid. Several concentrations of HF were used ranging from 5-50%. Additionally, submersion durations varied from 30 sec to 30 min. PS-b-PMMA (70:30, M_w = 67 kDa, with a polydispersity index [PI] of 1.09) was spin cast on to the substrates at angular velocities ranging from 2000-7000 rpm for 60 seconds. Anneal times at 170°C varied from 1-16 hours. After annealing, the coated substrates were exposed to 25 J of blanket ultra violet radiation to cross link the polystyrene and degrade the PMMA. The PMMA was removed by submersion in acetic acid with times that varied from 5 min to 1 hour. The success of this method of surface passivation produced limited results. The majority of PMMA columns aligned parallel to the surface rather than perpendicular to the surface (figure 1). The dark wormlike structures on the surface exhibit this parallel alignment.

The second method of surface passivation involved the grafting of OH-end functionalized PS/PMMA random copolymer brushes onto the native oxide layer of <100> silicon substrates. PS-r-PMMA-OH (M_w = 13.1 kDa, PI = 1.47) was spin cast at 700 rpm onto substrates and annealed at 140°C for times ranging from 15-48 hours. The prepared surfaces were rinsed numerous times with toluene to remove the excess random copolymer. The diblock copolymer was then applied with the same methods described above. The success of this method of surface passivation was dramatically better than the HF surface treatment. The great majority of PMMA columns aligned perpendicular to the surface (figure 2). The substrates were etched by reactive ion etching (RIE) using SF_6, confirming column penetration to the surface.

With the procedure described above, the diblock copolymer mask was then successfully applied to the surface of a 6H silicon carbide substrate. A SiO_x layer was thermally grown on a SiC (6H) substrate. The substrate was placed in an oxidizing furnace at 1100°C with an O_2 flow of 50 cm^3/min for 30 minutes. After cooling, the random copolymer brush treatment was applied to the surface, followed by the application of the diblock mask. Although the image quality is poor due to a failing AFM tip, figure 3 shows the definite formation of perpendicular PMMA columns.

Conclusions:

The application of PS/PMMA masks on silicon substrates has been well documented. However, due to variations in diblock and random copolymer synthesis, specific procedures that result in self-assembling morphology vary greatly. A procedure has been established for attaining mesoscale dot array masks using the specific diblock and random copolymers described above. The establishment of this procedure enabled the successful placement of a diblock copolymer mask with mesoscale holes on a silicon carbide substrate. The implications are far reaching. The silicon carbide can be etched using RIE with SF_6 chemistry yielding a porous surface on the mesoscopic scale. These porous wafers can then be used for mesoscale filtration in corrosive environments, substrates with enhanced lattice constant compatibility in material growth procedures, and the formation high-density capacitor arrays.

Acknowledgements

Howard MSRCE:

James Griffin, Tony Gomez, Gary Harris, William Rose, Crawford Taylor, Juan White, and Yvette Williams

Bakersfield College:

Sonya Christian

Cornell Nanofabrication Facility:

Melanie-Claire Mallison

University of Massachusetts-Amherst:

Thomas Russell and Ting Xu

National Science Foundation

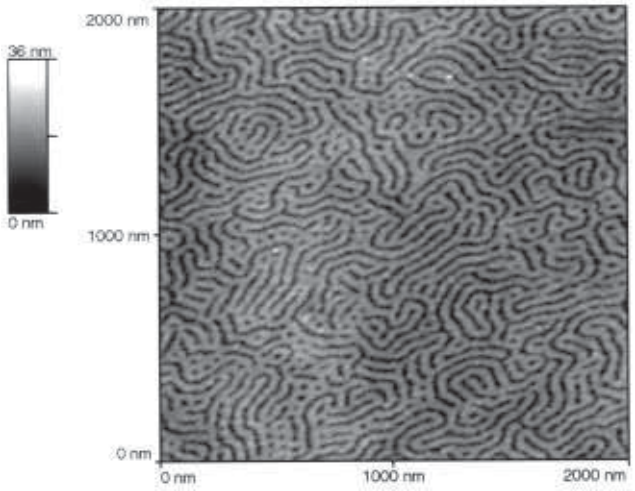

Figure 1. PS/PMMA deposited at 2700 rpm, annealed 12 hours at 170°C on Si.

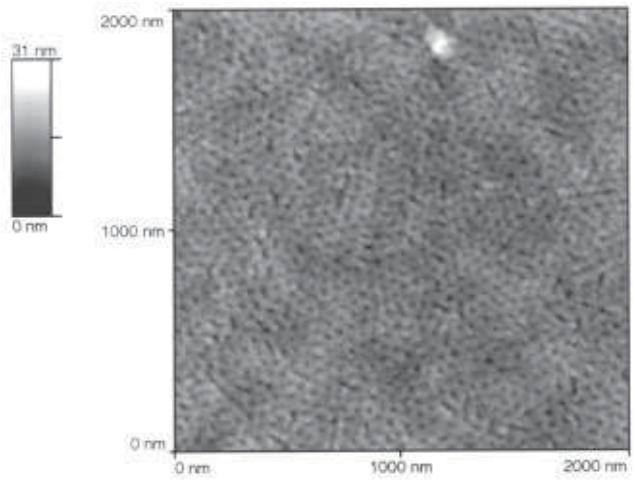

Figure 2. PS/PMMA deposited at 2900 rpm, annealed 14 hours at 170°C on Si.

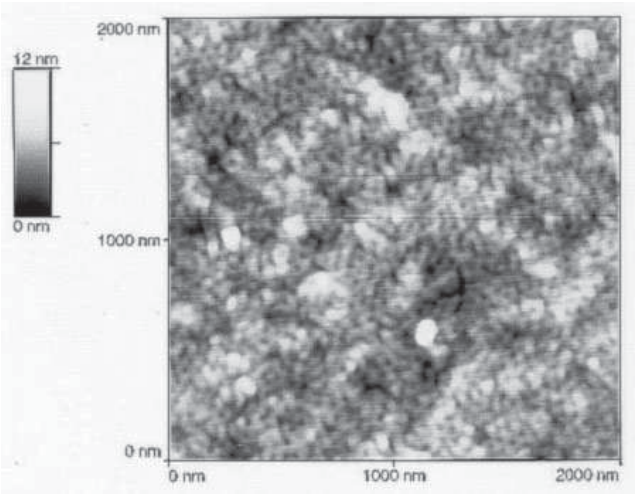

Figure 3. PS/PMMA deposited at 2800 rpm, annealed 14 hours at 170°C on SiC substrate.

Penn State Nanofabrication Facility

The Pennsylvania State University, University Park, PA

http://www.nanofab.psu.edu

2002 PSNF REU Interns

NNUN REU Intern	School Affiliation	Principal Investigator
From Left to Right:		
Ms. Rose Deeter	Lehigh University	Stephen Fonash & A. Brunner
Mr. Hector Luis Rodriguez	University of PR Mayaguez	Stephen Fonash & A. Kaan Kalkan
Ms. Diane Colello	Rensselaer PolyTech	Carlo Pantano
Mr. Matthew Pickett	The Pennsylvania State University	Jeff Catchmark
Ms. Kelly Wright	Texas A&M University	Greg McCarty
Ms. Lisa Daub	PSNF, Pennsylvania State University	REU Coordinator
Ms. Mamie Thant	Harvard University	David Allara & Tad Daniel
Mr. Greg McCarty	PSNF, Pennsylvania State University	REU Principal Investigator

Patterned Hybrid Sol-Gels for DNA Transport and Immobilization

Diane Colello, Biomedical Engineering, Rensselaer Polytechnic Institute

Carlo G. Pantano, Amy Barnes, Caner Durucan, MSE, The Pennsylvania State University

coleld@rpi.edu, pantano@ems.psu.edu

Abstract:

The sol-gel process yields an amorphous bonded silica network at low temperatures by hydrolysis — condensation reactions using suitable monomers. This statement defines the process used to synthesize our base material, hybrid sol-gels. Hybrid sol-gels differ from ordinary sol-gels by embedding organic groups in the silica network for chemical and/or functional modification.

The objective of this project was to synthesize and analyze the physical and chemical properties of a hybrid sol-gel for stamping patterns on a substrate. These gels were intended to interact with biomolecules such as DNA. The main objective for making particular hybrid sol-gels is their positively charged amine groups that are then able to attach to the negatively charged phosphate groups in the DNA strands.

Introduction:

The last decade has seen a revolution in the area of sol-gel derived materials since the demonstration that these materials can be used to encapsulate biological species such as enzymes, antibodies and other proteins in a functional state. The interactions between the biomolecule and hybrid nanocomposite material determines the degree to which the biomolecule retains its native properties, and such interactions can be tuned to provide optimized biomaterials that are suitable for a variety of applications including unique matrices for biophysical studies.

The use of biological species, such as DNA, has typically relied in large part on the successful immobilization of the intact biological reagent onto or within a suitable surface. Typical approaches to immobilize biomolecules onto inorganic, organic or polymeric surfaces have been based on covalent binding to surfaces, entrapment in semi-permeable membranes and microencapsulation into polymer microspheres and hydrogels.

Sol-gel chemistry is based on the polymerization of molecular precursors such as metal alkoxides $M(OR)_n$. The low temperature characteristic offered by the sol-gel process allows the introduction of organic molecules inside an inorganic network. The first reaction is a hydrolysis, which induces the condensation of silanol (Si-OH) groups forming siloxane (Si-O-Si) bonds, which lead to the silica network formation. The inorganic and organic components can be mixed at the molecular scale, in virtually any ratio leading to the hybrid organic-inorganic nanocomposites. These hybrids are extremely versatile in their chemical and mechanical properties, composition and processing.

One of the major advantages of sol-gel derived silicate materials for immobilization of proteins is that they have a tunable pore-size distribution which allows selected molecules and ions to diffuse while large biomolecules remain trapped in the pores, allowing size-dependent bioanalysis. Other major advantages of sol-gel derived biocomposites include the ease with which such materials can be used to make coatings, to be modified to improve analytical performance, and to interface with a large variety of different environments. Sol-gel derived materials can be produced using a wide range of compositions and can be used to entrap a large number of different biomolecules.

Procedure:

Many different hybrid sol-gels were made and analyzed. The main precursors included amino-propylsilane (APS) and tetraehtylorthosilicate (TEOS). The sol-gel samples were selected using many different factors including how long the sol-gel sample was aged, and its viscosity. Among the samples we have made, we present only two samples in this report; a base catalyzed silica sol-gel and a hybrid sol-gel.

After the sol-gel samples were made, we needed to decide on a method for applying this solution to the glass slides. Some methods of patterning include using a micropen, micromolding or stamping. For our purposes, we chose the micromolding method which includes using a stamp for printing. In order to make our stamp, we transferred a pattern onto a silicon wafer using photolithography and then made that pattern into a stamp. It was first necessary to coat the glass samples with the base catalyzed silica solution. Then, we dipped the stamps into the solutions and applied them to the catalyzed glass slides and heated

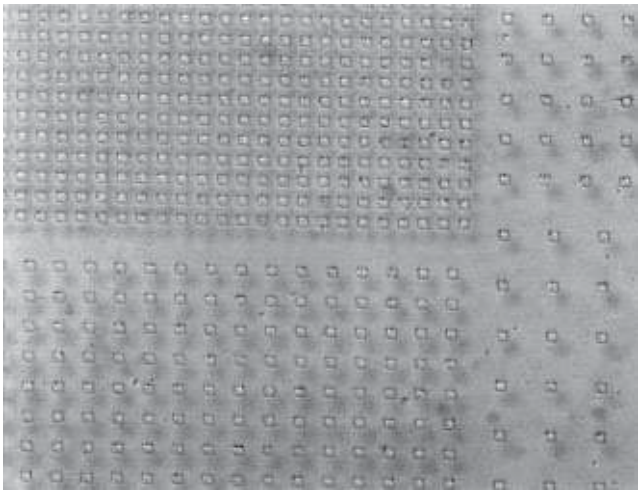

Figure 1. Optical microscope image for a hybrid sol-gel stamped onto a base catalyzed silica substrate.

them at 66°C for 15 minutes. We analyzed these patterns using optical microscopy as well as atomic force microscopy (AFM), illustrated in Figures 1 and 2 respectively.

Results and Conclusions:

Although stamping of sol-gels can create topographically distinct regions, it still needs to be improved for selective coverage in distinct regions. When analyzed with the AFM, we discovered much of the solution used to stamp was not only deposited in distinct regions for selective coverage but also on the surrounding substrate.

Because of this, we experimented using another similar technique known as micromolding in capillaries (MIMIC). This time, we placed the stamp in the center of the substrate forming a network of interconnected channels. The solution to be patterned filled these channels by capillary action. After the material in the fluid had deposited and gelled onto the surface of the substrate, the stamp was removed. This process was not fully successful because the sol-gel solution penetrated only a small distance from the edge of the stamp leaving the center region unstamped. However, with some modifications this process may prove to work.

Acknowledgements:

I would like to thank The Pennsylvania State University, Penn State Nanofabrication Facility, Rensselaer Polytechnic Institute, NNUN REU Program and participants especially Kelly Wright, Dr. Carlo Pantano and his research group especially Amy Barnes, Caner Durucan and Justin Wood.

References:

[1] Jin, Wen and John D. Brennan. "Properties and applications of proteins encapsulated within sol-gel derived materials." Analytica Chimica Acta 461 (2002): 36 pp. 18 July 2002. <http://www.chemistry.mcmaster.ca/faculty/brennan>.

[2] Kim, Enoch, Younan Xia and George M. Whitesides. "Micromolding in Capillaries: Applications in Materials Science." American Chemical Society 118 (1996): 9 pp.

[3] Phalippou, Jean. "Sol-Gel: A low temperature process for the materials of the new millennium." The Sol-gel Gateway. 22 July 2002. <http://www.solgel.com/articles/June00/phalip/introsolgel.htm>.

[4] Sanchez, Clement Dr. "What are Hybrids?" The Sol-Gel Gateway. 22 July 2002. <http://www.solgel.com/hybrids/hybrids.htm>.

[5] Sol-Gel Technologies. <http://www.sol-gel.com/chemi.htm>.

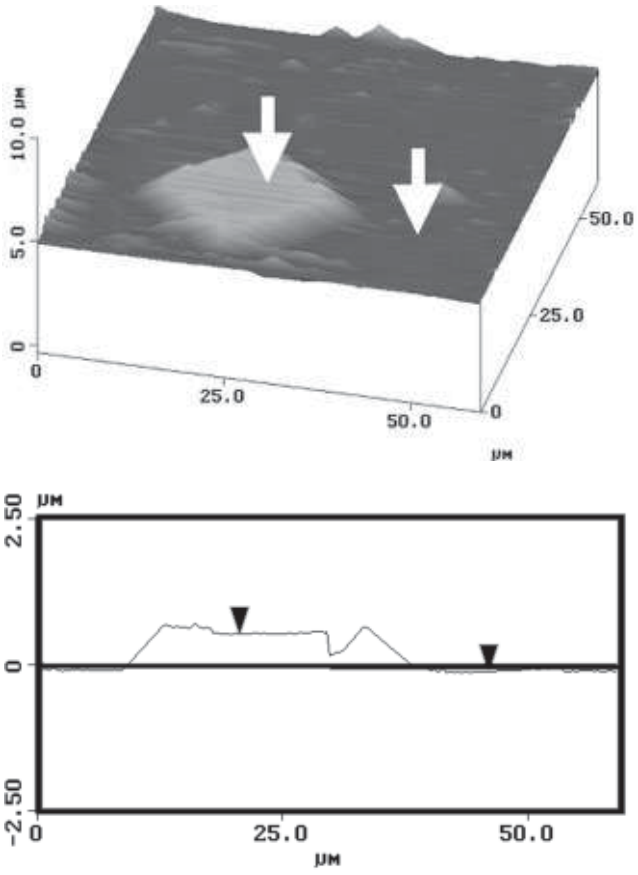

Figure 2a & b. AFM image of an individual 20 µm pad.

The Use of Nanostructured Thin Films to Control Cell Adhesion on Patterned Surfaces

Rose M. Deeter, Chemical Engineering, Lehigh University

Dr. Stephen Fonash, Director, Penn State Nanofabrication Facility,
Amy Brunner, Engineering Science, Pennsylvania State University
rmd7@lehigh.edu, sfonash@psu.edu

Abstract:

A study of the effect on prolonged annealing of column-void silicon films was performed. A number of samples were annealed for various time points ranging from zero to 24 hours. Each of these samples was submerged in nutrient media for time intervals ranging again from zero to 24 hours. Concurrently, a cell adhesion selectivity study was completed using some of these films that had been annealed for different time periods. The films were then exposed to a hepatocyte cell suspension for either forty minutes or one hour and forty minutes. The results indicate that the annealed column-void silicon films are more durable than those of the non-annealed, but the non-annealed samples displayed greater cell adhesion selectivity over glass substrates.

Introduction:

Currently many on-going research projects are investigating the manipulation and interrogation of isolated cells in uniquely controllable environments. This study focuses attention on increasing the chemical stability of column-void silicon films to maximize cell adhesion and stability, with the ultimate goal being the production of a cell-based biosensor. The chemical stability of the column-void silicon films is increased during the annealing process, which takes at elevated temperature in a controlled atmosphere furnace. Hepatocyte cells are deposited on the column-void silicon films, where cell adhesion and film stability are measured. This is can be done using an optical as well as a scanning electron microscope. Cell adhesion selectivity is determined only after the films have been exposed to a number of PBS washes to remove poorly adhered cells.

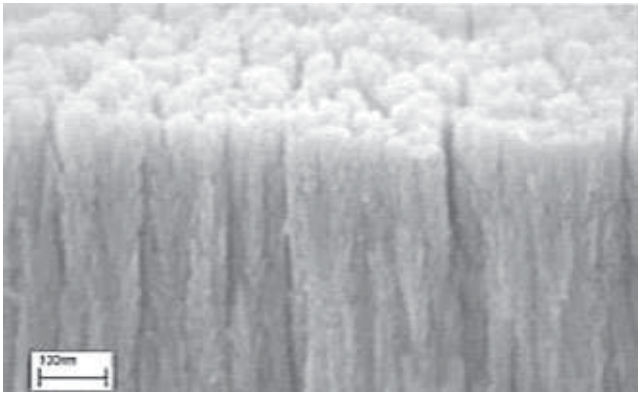

Figure 1: Column-void silicon network film.

Past experiments have lead to the hypothesis that long-term furnace treatments cause column-void silicon films to display less cell adhesion selectivity. The exact reason for this phenomenon was unknown, but the assumption was that the morphology of the columns of silicon was affected by the prolonged exposure to heat. Also, there was reason to believe that the cell nutrient media itself was degrading the column-void silicon films while the cells were trying to grow atop the slides. Since this assumption had surfaced, there was not a great deal of data regarding the time frame in which this degradation took place.

Procedure:

Column-void silicon films were prepared by depositing silicon onto a glass substrate by plasma enhanced chemical vapor deposition (PECVD) through the use of an ECR high-density plasma source.

Experimental Procedure:

In this experiment, columns of silicon were deposited onto forty-six 1 inch x 1/2 inch 1737 Corning glass slides. Since one of the goals of this study was to determine the effect of long-term annealing on column-void silicon films, the first part of the study needed thirty-two slides. Each set of seven slides was annealed at zero, four, fourteen or twenty-four hours at 400˚C in a furnace. Within each of those annealing time points, one of the samples was exposed to cell nutrient media for zero, one-half, two, four, eight, twenty-four, or forty-eight hours. By setting up a large matrix, it was possible to determine when and at what rate the column-void silicon films were being degraded.

Another target for this project dealt with understanding the effect of long-term annealing on the cell adhesion selectivity for the said films. Due to the volume of the anneal study itself, the cell adhesion selectivity study had fewer samples. Two column-void silicon slides were annealed at each zero, four, fourteen, and twenty-four hours.

A cell solution including nutrient media was pipetted onto the prepared slides for either forty minutes or one hour and forty minutes and rinsed with PBS solution. One of the zero hour annealed samples was exposed to this cell solution for forty minutes, while the other zero hour annealed sample was exposed to the solution for one hour and forty minutes, and likewise with the remaining six column-void silicon slides from the four, fourteen, and twenty-four hour anneals.

Results:

As seen in Figure 2, the non-annealed samples had a maximum lifespan of 8-10 hours in nutrient media before most of the column-void silicon had been etched away. Results of the four, fourteen, and twenty-four hour etch study showed a definite increase in the durability of the film as the anneal time increased. However, by the 24-hour submersion in nutrient media all of the column-void silicon had been etched away from all of the samples. The cell adhesion study produced three samples with prominent cell adhesion selectivity: 0 hour anneal, 40 minute submersion in cell solution; 0 hour anneal, 1 hour and 40 minute submersion in cell solution: and 4 hour anneal, 1 hour and 40 minute submersion in cell solution.

Conclusions:

The annealed column-void silicon films showed an increased durability when submerged in the nutrient media. FESEM pictures also confirmed that morphology of the columns of silicon were structurally unaffected by the long-term annealing. Previous hypothesis that the column-void silicon films oxidize and expand after prolonged annealing were incorrect, rather, something else is happening to the films during the furnace treatment that is affecting the cell adhesion selectivity. This is evident in the results of the cell adhesion selectivity study where the most obvious cell adhesion selectivity occurred on the zero or four hour annealed samples.

It is possible that the annealing process drives off hydrogen and causes crystallization of the silicon, or perhaps the samples are oxidizing on the surface when they are removed from the hot furnace environment to the ambient air. Either way, it is apparent that there is a chemical change on the surface of the column-void silicon films that is affecting the effectiveness of cell adhesion selectivity.

Acknowledgements:

Samples and pictures were provided by Amy Brunner and Daniel Hayes of Dr. Stephen Fonash's research group at the Pennsylvania State University.

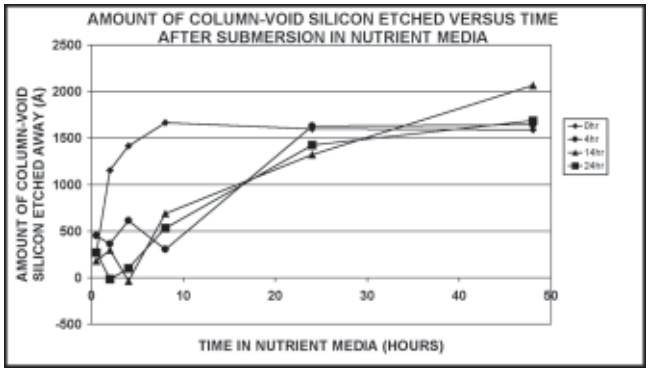

Figure 2: Results of the column-void silicon stability study.

Novel Materials and Processes for Electron Beam Lithography: Cyclotene™

Matthew Pickett, Engineering Science, The Pennsylvania State University

Jeffrey Catchmark, Guy Lavallee, Engineering Science, Penn State University

mdp181@psu.edu, jcatchmark@engr.psu.edu

Abstract:

Bisbenzocyclobutene (BCB) is a photosensitive directly-patternable dielectric that is currently being used in industry. There are a variety of different advantages to BCB including its low dielectric constant and its spin-on processing ability. It was recently discovered that, in addition to its photosensitive properties, BCB is sensitive to electron exposure. The focus of this project was to determine a process that yields the best results for the electron beam lithography of BCB. The procedure to accomplish this goal involved the evaluation of wafers fabricated with different processing parameters.

Introduction:

In semiconductor processing, it is common to encounter a procedure involving many steps in order to achieve a single patterned layer. Resist photolithography combined with various additive or subtractive techniques can be costly and time consuming but is an effective way of achieving the desired layer pattern. In dielectric patterning, however, there is a unique photosensitive spin-on material that can simplify processing because it is directly patternable. This material, bisbenzocyclobutene (BCB), is trademarked by Dow as Cyclotene and is currently used by a variety of companies in the semiconductor industry.

Recently an interesting discovery was made by Jeffrey Catchmark and Guy Lavallee at the Penn State Nanofab; BCB can be exposed by a beam of electrons as well as by UV light. Since electron beam lithography can be much more accurate than photolithography, this exciting discovery opened the door for a multitude of different questions and research possibilities.

The goal of this particular research effort was to determine the best process for the electron beam lithography of BCB. In order to determine the optimal process parameters, many sample wafers were fabricated and characterized to see which techniques led to the most desirable results. After data from characterization was obtained and analyzed, the process parameters were refined and retested. Ultimately, the process which yielded the best results was chosen as the candidate for future studies on the e-beam lithography of BCB.

Procedure:

The first part of the project was to design the pattern to be written on the wafer. This pattern was devised with the intent to test the resolution capabilities of BCB with various different feature sizes and shapes. The final mask was created with a CAD software package named L-Edit and was prepared for the e-beam writer.

After the completion of the pattern, the actual fabrication and testing of the e-beam process for BCB had to be planned and executed. As a starting point, the steps and parameters for the photolithographic processing of BCB were examined. From there, an initial process for e-beam lithography was established. In that process, there were three major steps: application, exposure, and development. Throughout the entire project only four parameters were modified while the rest were held constant. They were the post exposure bake time and temperature, the BCB solution ratio, and the dose.

In the application step, the wafer was first given a dehydration bake at 180°C for 5 minutes. AP3000, an adhesion promoter, was then spun dry onto the wafer. The BCB, which was diluted in T1100 solvent, was then spun on under two steps. It was applied and immediately spun at 500 rpm for 10 seconds ramped at 250 rpm s^{-1}. Without delay the rpm was then ramped up to 5000 rpm at 500 rpm s-1 and stayed there for 40 more seconds. After the BCB was spun on, the wafer was given a post application bake at 70°C for 60 seconds.

In the exposure step, the wafer was directly written by the e-beam writer at the PSU Nanofab, a Leica EBPG-HR5. The CAD pattern designed in the first phase of the project was written multiple times on the same wafer with different doses. Throughout the project, doses of 10-300 μC cm^{-2} were examined.

After exposure, the development step was carried out. The first part of the development step was a post exposure bake which was the most extensively studied parameter. In the course of the study, it was varied from 25-130°C with times of 30-180 seconds. After

the post exposure bake, the wafer was puddle developed in a spinner with DS2100. The first part of the puddle development was to puddle the developer right on the surface of the wafer for 80 seconds. Just afterwards, the wafer was spun at 500 rpm for 10 seconds with a 250 rpm s^{-1} ramp. The spinner was then ramped up to 3500 rpm for 40 seconds at 500 rpm s^{-1}. During the first spin stage, DS2100 was continuously squirted on the wafer to assist in particulate removal.

After the fabrication of the wafers, they were characterized with a Leica 1530 FESEM. Analysis of characterizations were then used to determine which process parameters yielded the best results. From there the parameters were refined and the entire procedure was repeated in order to further improve the product.

Results and Discussion:

The results of the study indicated that, of the samples tested, the best results came from the wafer with a 4:1 T1100:BCB solution, a post exposure bake of 70°C for 90 seconds, and a dose of 28 μC cm^{-2}.

An FESEM micrograph of BCB features with a minimum width of 100 nm that were fabricated under those parameters can be seen in figure 1.

Although these results are not quite indicative of the ultimate capabilities of electron beam lithography, they clearly demonstrate that BCB has potential as a spin-on low k dielectric e-beam material.

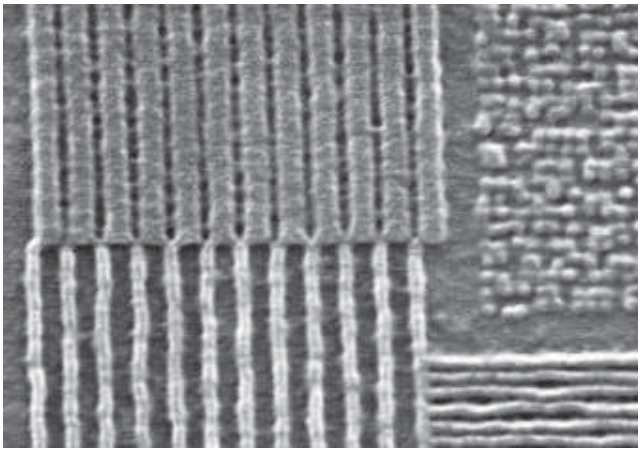

Figure 1: 4:1 BCB solution processed with a 70°C post exposure bake for 90 seconds with a dose of 28 μC cm^{-2}. FESEM micrograph: 50000X.

Electroless-Ag-Coated Nanostructured Si Films for Surface Enhanced Raman Spectroscopy

Hector Luis Rodriguez, Chemical Engineering, University of PR Mayaguez

Stephen J. Fonash, Kaan Kalkan, PSNF, The Pennsylvania State University

doogie_hl@hotmail.com, sfonash@psu.edu

Abstract:

Nanostructured Si films were coated with Ag nanospheres using solution chemistry. The Ag nanoparticles attached to the Si film were found to yield strong surface plasmon optical absorption and surface enhanced Raman scattering.

Introduction:

Molecular detection and identification is of great interest in various disciplines such as analytical chemistry, molecular biology, pharmacology, nanotechnology, and environmental science. In recent years, surface-enhanced Raman spectroscopy (SERS) has emerged as one of the most sensitive spectroscopic tools available for the detection of a wide range of adsorbate molecules down to the single molecule detection limit [1]. SERS involves spectral measurement of the inelasticly scattered light from an analyte material (e.g., molecules) adsorbed on noble metal nanoparticles of subwavelength dimensions.

Once the surface plasmon modes (collective oscillations of free electrons) in a metal nanoparticle are in resonance with the impinging electromagnetic field such as an impinging laser beam, high oscillating dipoles are induced in the nanoparticle that in turn develop strong local electric fields in their vicinity. This amplification in the local electric field is for both the incident light and Raman scattered light.

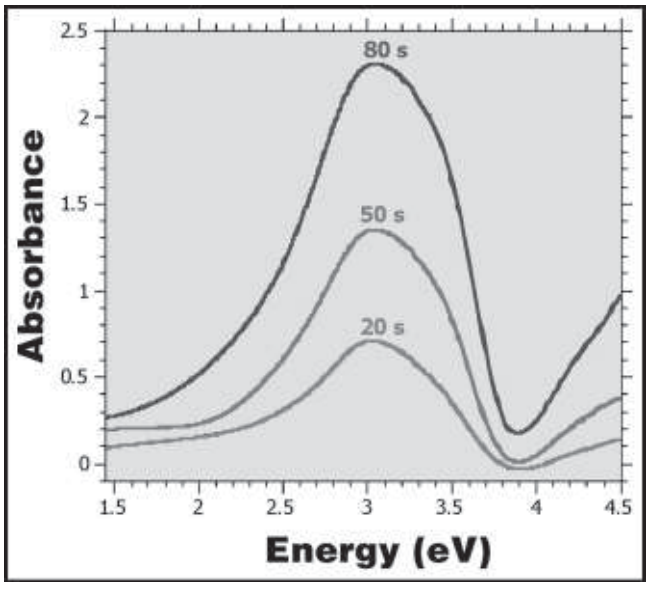

Figure 1: Surface plasmon absorbance spectra of Ag nanospheres.

As a result, enormous gains are possible in the intensity of the SERS signal which is the fingerprint of the adsorbed molecule. SERS has been conventionally practiced with metal nanoparticles synthesized by vapor deposition, electrochemical roughening of metal surfaces, colloidal chemistry or patterning of continuous metal films by electron beam lithography [2]. In this study, a novel method is introduced where metal particles were produced directly on a nanostructured Si film using solution chemistry.

Experimental Procedure:

Our solution-based Ag nanoparticle coating process was carried out in a 400 ml beaker by simply immersing the nanostructured Si films. Once the films were immersed in solution, a gradual increase in optical absorption was observed while the transmitted color continuously turned from lighter to darker brown. The film surface was observed to develop a shiny metallic-like reflectance for immersion durations above ~100 seconds, indicative of formation of bulk-like Ag. Accordingly, the samples for study were prepared with immersion times between 20 to 90 seconds.

Following the immersion, the samples were rinsed in de-ionized water. Unless the samples were characterized, they were stored in a N_2 glove box to prevent deterioration of the Ag. Optical absorption was measured with a Perkin-Elmer Lambda 9 spectrometer. A Leo 1530 FE-SEM was employed to study the microstructure. Raman scattering spectra was obtained by an ISA U-1000 Raman spectrometer using 515 nm Ar laser excitation of 30 mW.

Results and Conclusions:

Figure 1 depicts time evolution of optical absorbance by Ag nanoparticles synthesized on Si films (2000 Å thick) immersed for 20, 50, and 80 s. Absorbance by the Ag nanoparticles was derived by

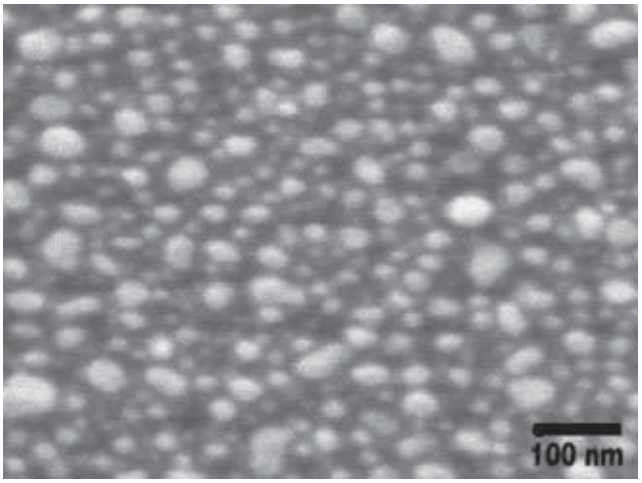

Figure 2: Ag nanoparticles coated on the surface of a nanostructured Si film.

subtracting the absorbance of unexposed film from that of exposed (immersed) film. A systematic increase in absorption with time in the violet-blue region is seen. The absorption band peaking at ~3.0 eV is characteristic of surface plasmon resonance associated with Ag nanospheres. A top surface micrograph of the 90 s exposed sample is shown in Figure 2, which confirms the presence of spherically shaped Ag nanoparticles.

Figure 3 demonstrates the SERS effect. No signal was detected without the presence of the Ag nanoparticles (0 s). On the other hand, for films coated with nanoparticles (for 50 and 90 s), the characteristic amorphous/nanocrystalline Si band is clearly seen.

Therefore Ag nanoparticles enhance Raman scattering for the Si film material they coat.

Acknowledgments:

Support of Penn State Nanofab, especially of Bill Drawl and Ed Basgall, in Raman spectroscopy and SEM, respectively, is gratefully acknowledged.

References:

[1] S. Nie and S.R. Emory, Science v275, 1102 (1997).

[2] K. Kneipp, H. Kneipp, I. Itzkan, R.R. Dasari, and M.S. Feld, Chem. Rev. v99, 2957 (1999).

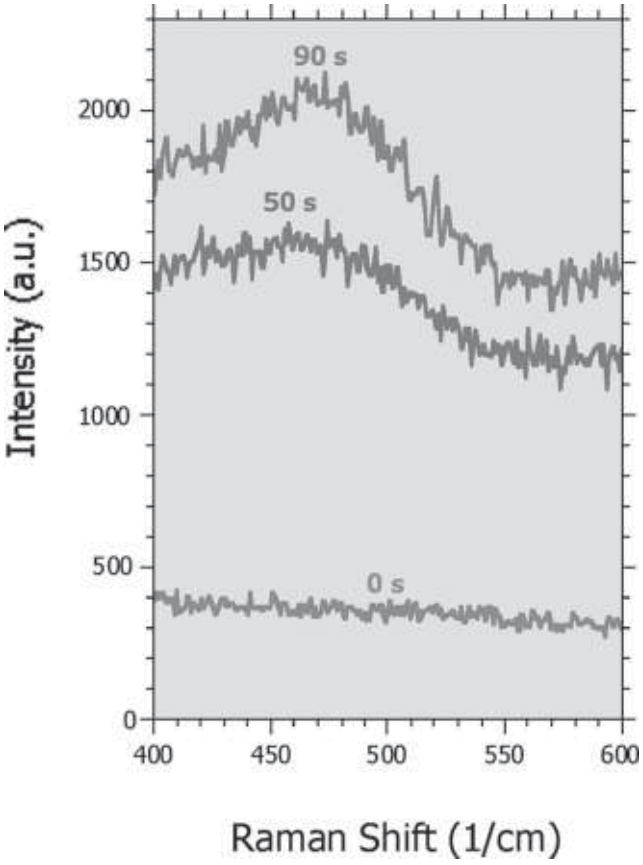

Figure 3: Demonstration of the SERS effect.

Nanometer-Thickness Oxide and Organic Gate Film Evaluation

Mamie Thant, Chemistry, Harvard University

David Allara, Tad Daniel, Chemistry, The Pennsylvania State University

thant@fas.harvard.edu, dla3@psu.edu

Abstract:

Silicon oxide is used as a dielectric for molecular-scale electronic devices because of its ability to be spun into nanometer-thin films. The goal of this project was to characterize SiO_2 films created by various kinds of argon ion sputtering, as well as tetraethyl ethoxy silane (TEOS)-based sol-gels, both electrically and optically. Furthermore, techniques for depositing small amounts of metal to create micron - scale metal-insulator-metal test electrodes on the sputtered SiO_2 films were explored. This provides a basis for making ever-smaller electronic devices.

Procedure:

2" Si wafers were cleaned in Piranha, then rinsed with ethanol, and UV-ozoned. They were then dc sputter-coated with platinum — used because of its low roughness — to a thickness of approximately 100-200 nm. Null ellipsometry was taken at three points on each wafer to note the roughness of the Pt.

Dr. Mark Horn then sputter-coated the Pt samples with SiO_2 of different thicknesses by three different methods: rf (radio frequency), rf/dc (radio frequency/direct current), and pulsed dc currents. The newly SiO_2-coated wafers were again subjected to null ellipsometry to measure thickness and film uniformity.

To apply sol-gel to additional Pt samples, the wafers were first cleaned with ethanol, n-hexane, and acetone, dried with compressed N_2, then UV-ozoned for 7 minutes with a light flow of N_2. They were then covered with approximately 3 mL of 30% H_2O_2 (enough to cover the surface) which sat for 5 minutes before being spun off at 7.5 V (about 3000 rpm) until the H_2O_2 was no longer visible. The H_2O_2 oxidized the Pt surface, facilitating sol-gel adhesion.

Approximately 3 mL of a sol-gel solution, prepared from TEOS and ethanol and adjusted to a pH of 3 with dilute HCl, was applied to the Pt and spun off immediately at 7.5 V. The spinning was done at different times, ranging from 20 to 70 seconds—this, along with varying the volumetric ratio of TEOS to ethanol, helped create variety in the sol-gel film thicknesses.

Tapping mode AFM was performed on both sputtered and sol-gel films at 3 points per wafer, to find the new surface roughnesses and compare them to the roughnesses of bare Pt samples. All SiO_2 films were then analyzed by reflection FT-IR.

For conductance tests on the sputtered SiO_2 films, a large stencil mask with circular holes of 1.125 mm, 839.5 µm, 625 µm, 380 µm, and 291.5 µm was used initially to create the test electrodes. The stencil mask was placed over top of the SiO_2/Pt samples, and first chromium, then gold were sputtered through the mask's holes to create top metal layer pads.

The actual conductance tests involved two probes and an optical microscope: one probe was placed on an area of bare Pt, while the other was placed on top of a Cr/Au pad. A range of voltages was placed across the two probes, and current between them was measured.

For conductance tests to be done in the future, a stencil mask with smaller holes was developed. Because of the difficulty of creating a mask with small holes by conventional methods, we used a crystallographic etch through the Si wafer with TMAH (tetramethylammonium hydroxide) to create the small holes by taking advantage of tapering sidewalls.

Double-side polished 3" diameter silicon wafers 250 µm thick were coated on both sides with approximately 2000 Å of silicon nitride. These wafers were then patterned with photolithography, using a mask with an array of square holes ranging from 0.5 mm to 0.1 mm on a side. After developing, MERIE (Magnetically Enhanced Reactive Ion Etch) removed the nitride in exposed regions, then a 10% TMAH solution at 80°C with ammonium peroxidisulfate was used to etch along the 1-0-0 plane of the Si [1].

Results and Conclusion:

AFM images showed that bare Pt samples had RMS roughnesses ranging from 5 to 10 Å. Both types of SiO_2 films deposited—sputtered and sol-gel—were remarkably smooth, with RMS roughnesses ranging from 4 to 12 Å for the sputtered films and 4 to 10 Å for the sol gels (the 10 Å roughness being the result of a 12 Å roughness Pt substrate).

SAMPLE	RMS Average Roughnesses (nm) (1 μm scans)	RMS Average Roughnesses (nm) (5 μm scans)
RFDC50	1.172	1.224
RFDC100	0.666	0.555
RFDC200	0.513	0.610
RF50	0.731	0.799
RF100	0.519	0.521
RF200	0.624	0.767
Pulsed DC 50	0.945	0.698
Pulsed DC 100	0.674	0.556
Pulsed DC 200	0.573	0.549
Pt Substrate 1	0.611	0.992
Pt Substrate 2	4.351	9.573
Pt Substrate 1 + Sol-Gel	0.736	0.763
Pt Substrate 2 + Sol-Gel	0.807	1.097

Figure 1: "Typical" bare Pt roughnesses can be inferred from platinum substrate 1.

The sputtered films had a roughness similar to the bare Pt substrate; sol-gel films either had roughnesses similar to the original substrate or, in the case of very rough initial substrates, they planarized the surface (figure 1). The different types of sputtering produced films of comparable roughness for the same thickness.

The FT-IR spectra (figure 2) revealed that the peak with highest absorbance occurred around 1240 cm^{-1}, as had been previously shown for sol-gel [2]. This peak is attributed to the longitudinal optical (LO) vibration mode of Si-O bond stretching. A shoulder at around 1135 cm^{-1} was also seen, attributed to another form of LO vibration mode Si-O stretching. This shoulder was much more pronounced in the sol-gel spectra, possibly because of differences in the Si-O matrix structure.

Conduction probe measurements on the metal pads made with the larger stencil mask indicated that the film had resistor-like qualities, contrary to expectations. Possible explanations include tiny defects in the film that led to shorts, improper deposition techniques, or impurities in the film.

Optimization of the smaller stencil mask creation process was successful: the etched mask had holes less than 0.1 mm on a side. Similar masks can thus be used for future conduction probe results; because of the significantly smaller size of the resulting metal pads, the number of defects in the SiO_2 film involved in the test electrode can be reduced, leading to better conduction probe results.

Acknowledgments:

Thanks to Prof. Allara and the Allara group, Tad Daniel, Mark Horn, and Shane Miller and the staff at the nanofab, and the REUs.

References:

[1] Yan, G.; Chan, P.C.H., Hsing, I.M.; et al. An improved TMAH Si-etching solution without attacking exposed aluminum. Sensors and Actuators A 89 (2001) 135-141.

[2] Wang, Z. Dissertation, Pennsylvania State University. 1994.

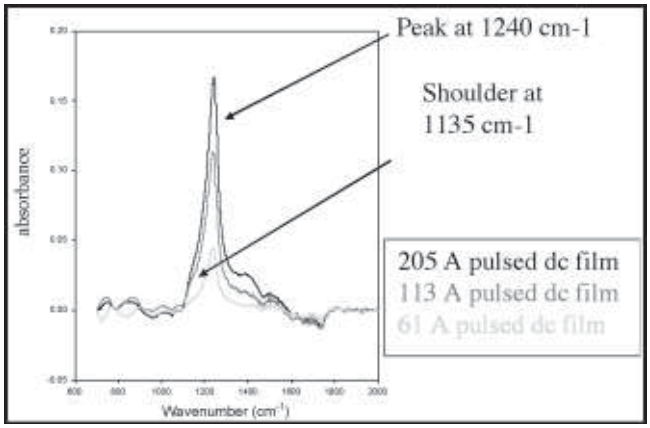

Figure 2: Representative FTIR spectra for sputtered SiO_2 films.

The Fabrication of Electrode Structures with Tailorable Nanometer Scale Gaps

Kelly Wright, Biomedical Engineering, Texas A&M University

Gregory S. McCarty, Engineering Science, The Pennsylvania State University

kwright@tamu.edu, gmccarty@engr.psu.edu

Abstract:

Nanometer scale gaps have been created between electrode structures using molecular rulers and traditional lithographic techniques.

In this work, we utilized the ability of alkanethiol monolayers to self assemble into molecularly precise films on metallic surfaces. Using alternating layers of mercaptohexadecanoic acid and copper ions, gaps from 4 to 40 nm could be created between microfabricated electrodes. The Ti/Au electrode structures were created using a photolithography lift-off process. The fabricated electrode structures were characterized and utilized to probe the electronic properties of nanostructured materials.

Introduction:

Current photolithographic techniques produce accurate features as small as 250 nm using a UV stepper. Other techniques, including electron beam lithography, have limitations below 100 nm [1]. Using the ability of alkanethiol monolayers to self assemble onto metallic surfaces, features as small as 4 nm can be created. The construction of nanometer scale features is extremely important to the world of advanced electronics [1], and more specifically, for the purpose of measuring the electrical properties of nanostructured materials. Measuring the electrical properties of nanostructured materials is necessary for determining their potential applications in molecular electronics [2]. This study shows that nanofabricated electrodes with separations of 4 to 40 nm can be constructed using a combination of lithographies. Additionally, the electronic properties of these structures were probed to determine their usefulness for evaluating nanostructured materials.

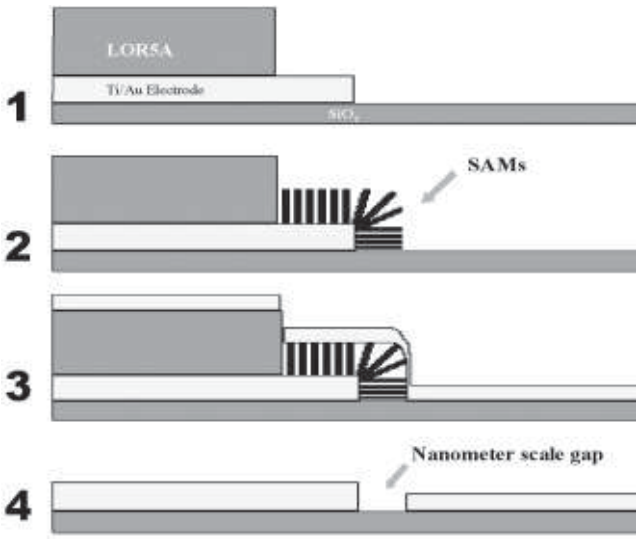

Figure 1: Fabrication of nanometer scale separation between electrodes.

Experimentation:

This study was performed on piranha-cleaned glass on which a pattern of single electrodes, consisting of 20 nm Ti and 30 nm Au, was deposited using a photolithography lift-off process. An overlapping electrode pattern was then applied using photolithography (shown as 1 in Figure 1).

At this point, self-assembling monolayers were deposited layer-by-layer in order to create a separation between the structures (2 in Figure 1). 1 mM 16-mercaptohexadecanoic acid was evaporated onto the wafer at 50°C from 1 to 4 hours. The glass was then immersed in a 1 mM solution of Copper (II) Perchlorate in deionized water. This immersion in Cu^{2+} ions was used to connect consecutive layers.

This procedure was repeated until the desired width of the gap was achieved, using the knowledge that the average thickness of each layer is 2 nm [1]. For our purposes, we repeated the process five times. Then 10 nm Ti and 20 nm Au were evaporated on top of the molecular resist (3 in Figure 1) and developed in CD-26 microposit developer. CD-26 performed the lift-off of the LOR5A and also contributed to the removal of the metal-organic layer (4 in Figure 1). Usually, further removal was needed, so we used ACT 935 heated to 60°C in five to ten minute intervals to strip the remaining overlapping tips.

When successful lift-off had been achieved, the structures were probed to characterize their electronic properties. Measurements of voltage and current were taken under varying conditions and with modifications to the electrodes.

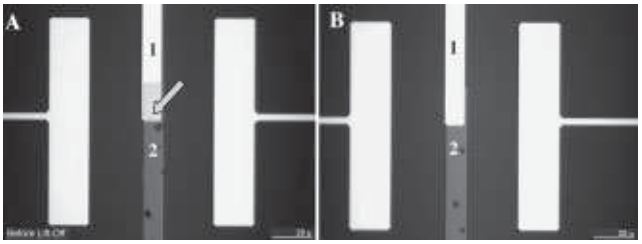

Figure 2: Images of the electrode tips (A) before lift-off and (B) after lift-off. The electrode labeled "1" was deposited first, and "2" was deposited on top. The arrow points to the overlapping area covered in alkanethiols that was stripped by ACT 935.

Results:

Preliminary results are encouraging. Lift-off of the organic-metal resist was problematic at first; placing the substrate in a 1mM solution of 16-mercapto-hexadecanoic acid in ethanol caused deterioration of the lift-off resist (LOR5A). Better results were achieved by evaporating the alkanethiol layers onto the substrate. While other studies reported sonicating the sample in 0.06 M HCl in 75% dimethylformamide to remove both the resist and the metal covering [1], we were concerned about maintaining the integrity of the electrode structure in such a solution. Therefore, we used ACT 935 to remove the overlapping metal-resist layer. Many of the electrode tips were never stripped from certain electrode patterns, signifying the importance of the electrode design of the lift-off process. It was found that large overlapping areas were more readily stripped than smaller ones.

Additionally, the electrodes gave excellent current and voltage readings for different types of nano-structured materials. The nanometer scale gap was shown to be a non-conducting pathway, allowing current leakage only on the order of picoamps, similar to measuring the probes in an open loop configuration (see Figure 3). Short-circuiting a single electrode gave current measurements of nearly 100 milliamps at approximately 0.5 volts, showing the electrode's ability to conduct well.

Furthermore, data showed that distinct measurements were achieved when the electrodes were probed in air, under deionized water, and under phosphate-buffered saline (see Figure 4). This shows that the electrodes are a promising candidate for measuring the electrical properties of nanostructured materials. Unfortunately, we were not able to limit conductions to the separation gap, and initial attempts to isolate the electrode tips using SAM-modification and protein-modification were unsuccessful. Future work includes plans to electrically isolate the electrode structure from the sample of interest.

Acknowledgments:

A special thanks goes to my mentor, Greg McCarty, for all his help. I would also like to thank Shane Miller for his relentless pursuit of vacuum integrity, as well as all of the staff at the MRI. To Mamie, Rose, Diane, Hector, and Matt—thanks for making this summer a memorable one.

References:

[1] A. Hatzor, P. S. Weiss. Science. 291, 1019 (2001).

[2] I. Amlani, A. M. Rawlett, L. A. Nagahara, R. K. Tsui. Appl. Phys. Lett. 80, 2761 (2002).

[3] S. D. Evans, A. Ulman, K. E. Goppert-Berarducci, J. L. Gerenser. J. Am. Chem. Soc. 113, 5866 (1991).

[4] A. Ulman. Chem. Rev. 96, 1533 (1996).

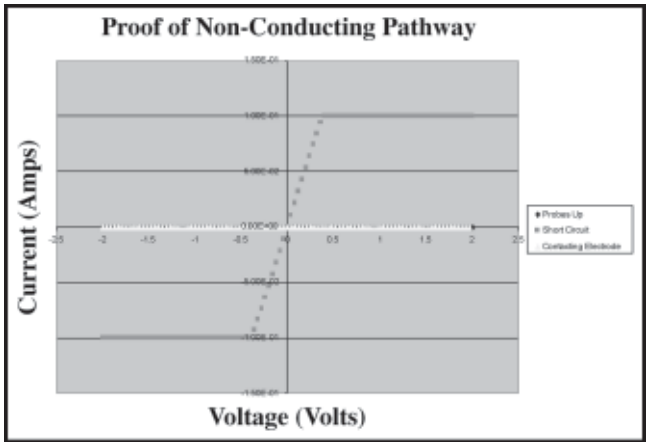

Figure 3, above: Graph showing that the nanoscale gap is a non-conducting pathway.

Figure 4, below: Graph showing differences in measurements of electrodes in air, deionized water, and phosphate buffered saline.

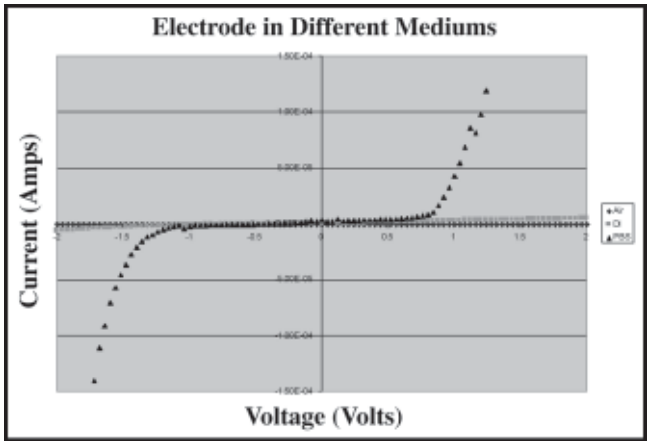

Stanford Nanofabrication Facility
Stanford University, Stanford, CA
http://snf.stanford.edu/

2002 SNF REU Interns

NNUN REU Intern	School Affiliation	Principal Investigator
From Left to Right:		
Dr. Yoshio Nishi	Stanford Nanofabrication Facility	NNUN Site Director
Mr. Michael Shearn II	Southern Methodist University	Shan Wang & Jason Jury
Mr. John Liu	UC Irvine	Hongjie Dai, Qian Wang & Ant Ural
Mr. Mark Elias	The Ohio State University	Piero Pianetta & Zhi Liu
Mr. Curtis Mead	University of Minnesota	Fabian Pease
Mr. Robert Caldwell	Boston College	Hongjie Dai, Qian Wang & Ant Ural
Ms. Schuyler Mudge	University of Washington	Jim Harris & Wonnill Ha
Ms. Amy Cosnowski	University of Michigan	Peter Griffin
Ms. Mahmooda Sultana	University of Southern California	Mike Deal & Yaocheng Liu
Mr. Scott Howard	University of Notre Dame	Fabian Pease
Ms. Eszter Horanyi	University of Colorado Boulder	Peter Griffin
Ms. Laura Zager	Swarthmore College	Jim Harris & Evan Thrush
Dr. Michael Deal	Stanford Nanofabrication Facility	REU Principal Investigator
Ms. Jane Edwards	Stanford Nanofabrication Facility	REU Coordinator
Mr. Robert Gagler	University of Colorado Boulder	Bruce Clemens

Carbon Nanotubes as Piezoresistors for a Pressure Sensor

Robert Caldwell, Physics, Boston College

Prof. Hongjie Dai, Qian Wang, Chemistry, Randy Grow,
Applied Physics, Stanford University
caldwera@bc.edu, hdai1@leland.stanford.edu

Abstract:

Current piezoresistors (materials whose electrical resistance changes with an induced stress) are normally made from highly doped silicon, resulting in a small patch of a chip that is highly sensitive to changes in acceleration, pressure and other basic states. One of the biggest problems with using silicon to make the piezoresistor is that its resistance is highly sensitive to changes in temperature, forcing companies to spend large amounts of money to compensate for this dependency.

Instead of using highly doped silicon, we will be growing carbon nanotubes, which also possess piezoresistor qualities, from catalyst islands located on the chip and use them as piezoresistors for a pressure sensor. The nanotube will lie on the edge of a membrane that will bulge outwards due to a decrease in pressure (there is a cavity under the membrane in the silicon that is at one atmosphere of pressure and this means that when the pressure outside the chip is lowered, the membrane will flex outwards), thus deforming the nanotube and changing its resistance.

We anticipate that due to the low temperature coefficient of the nanotubes, which is almost two orders of magnitude lower than in silicon, and increased sensitivity we will have made a pressure sensor that will be almost as easy to make, equally efficient and significantly cheaper than the ones currently available.

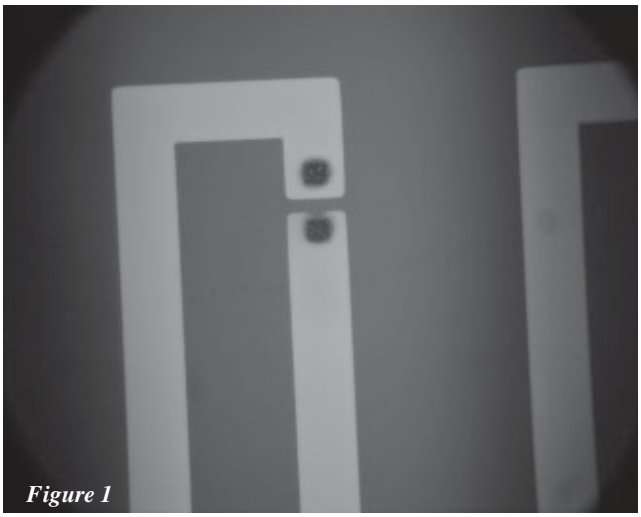

Figure 1

Introduction:

Carbon nanotubes, rolled sheets of graphite that can vary greatly in their electrical properties depending on their chirality, have been shown to exhibit piezoresistivity. Our goal is to manufacture, using standard silicon processing methods, chips of pressure sensors and then grow single walled nanotubes on them.

The pressure sensor will consist of a hollowed out portion of one silicon wafer bonded to another one to form a cavity that will be at one atmosphere of pressure. There will be a thin membrane, roughly 2 µm thick, made from either polysilicon and nitride or just pure nitride on which the nanotubes will be grown. The chips will then be placed in a vacuum chamber and when a vacuum is applied, the membrane will flex, creating a strain on the membrane and thus on the nanotube as well.

Calculations show that the membrane will exhibit a maximum strain at the edge and would therefore be the ideal place for the nanotube to lie. A piezoreisistor is a material that exhibits a change in its resistance when a strain is applied, so when the nanotube is strained and the membrane is flexed, we will measure the change in the current through the nanotube and from that, we can measure the change in the pressure.

Procedure:

We started with 300 µm silicon wafers and deposited on them 100-200 nm of oxide followed by roughly 2 µm of polysilicon. The polysilicon was removed from the backside of the wafers using dry etching techniques and a layer of nitride roughly 200 nm thick was added to both sides.

In a second batch of wafers, the electrodes and bonding pads were created using lift-off procedures.

The third batch of wafers did not have a polysilicon membrane, but rather a pure nitride one that was about 2 µm thick.

The next step was to pattern and etch the backside of the wafers and by this method, create a nitride mask for the KOH etch that would create the cavities for the pressure sensor. After the backside patterning was

complete, metal, in this case molybdenum, was sputtered onto the front of the wafers and it was then etched to create electrodes and bonding pads.

The design of the chip is such that each electrode pair would come to within 4 μm of each other and the catalyst for the nanotube growth would then sit in a shallow well near the edge of the electrodes, as seen in figure 1. The nanotubes would then grow out from the catalyst islands and span the gap between the electrodes, as shown by SEM in figure 2.

The final steps of the processing consisted of patterning the metal for the catalyst islands using PMMA as a mask for the dry etching and then using KOH to etch through the entire wafer from the backside. The nanotubes were then grown onto individual chips (there were about 52 chips per wafer) and the chip was then bonded to another piece of blank wafer using epoxy to form the cavity.

Results and Conclusions:

Preliminary tests show that we can measure the change in current due to the strain in the nanotube. In most cases, we noticed only a 10% or so change in the current, but in a few tests there was almost a 100% change (which very likely was the chip being blown out of contact with the probe station).

The setup to make these rough tests consisted of blowing gas onto the membrane from a very small distance and measure current versus time. There was a sharp change in the current from one value to another whenever the gas was turned on. When the chip was lightly hit, the membrane and the current values returned to their original positions, so the experiment proved to be highly reproducible. The membranes on the polysilicon chips were slightly bowed outwards due to the thin layer of nitride above the polysilicon.

SEM and AFM images have shown that we still need to play around with the growth conditions in order to achieve having just a single nanotube span the gap between the electrodes, but we have now seen that our pressure sensor works for the gas setup using the probe station.

One test conducted in the vacuum chamber had no change in the current when the chamber was pumped upon, indicating that there was probably something wrong with the chip itself or with the nanotubes.

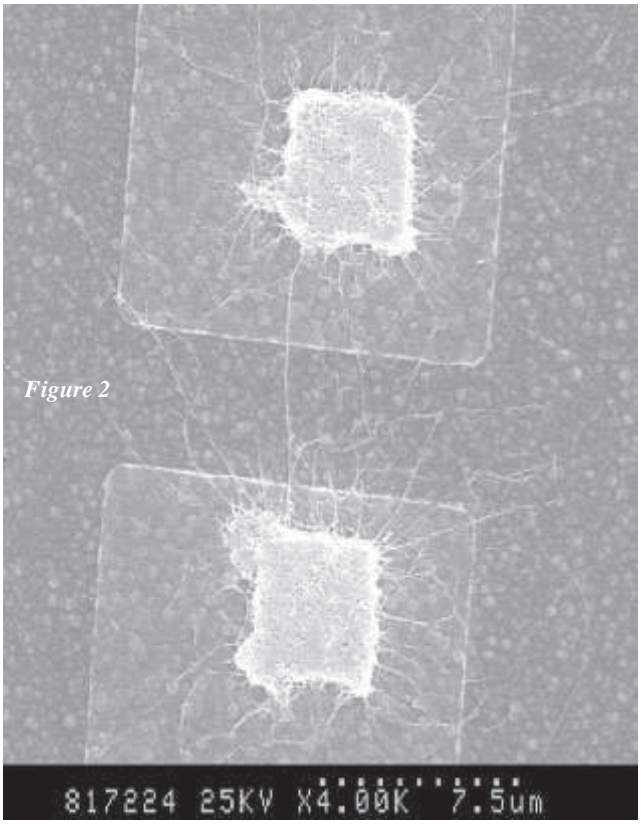

Figure 2

Pyrosequencing of DNA using Electrowetting on Dielectrics

Amy Cosnowski, Chemical Engineering, University of Michigan

Peter Griffin, Ali Agah, Department of Electrical Engineering, Stanford University

acosnows@engin.umich.edu, griffin@plumb.stanford.edu

Introduction:

With the completion of the Human Genome Project, the need for precise and efficient DNA sequencing has increased. One such method, pyrosequencing, has been shown to accurately sequence short segments of DNA [1]. Pyrosequencing is a process that uses enzymatic reactions to determine the sequence of DNA. A schematic of these reactions is located in figure 1. The process begins when the next base in the sequence interacts with DNA Polymerase. Polymerase binds the free base to the DNA strand, incorporating it into the sequence. PPi is formed as a byproduct of this reaction. Sulfurylase converts PPi into ATP, which is then converted into energy by luciferase. An enzyme found in lightening bugs, luciferase releases the energy of ATP in the form of light. These light signals are captured by a digital camera and sent to a computer, thereby allowing the DNA to be sequenced.

While the basic process of pyrosequencing is simple, performing the actual procedure is expensive and cumbersome. Currently, pyrosequencing is performed in rather large and costly machines. It is the hopes of my research group to miniaturize the process reducing the materials needed; thus, decreasing the cost. Initial steps

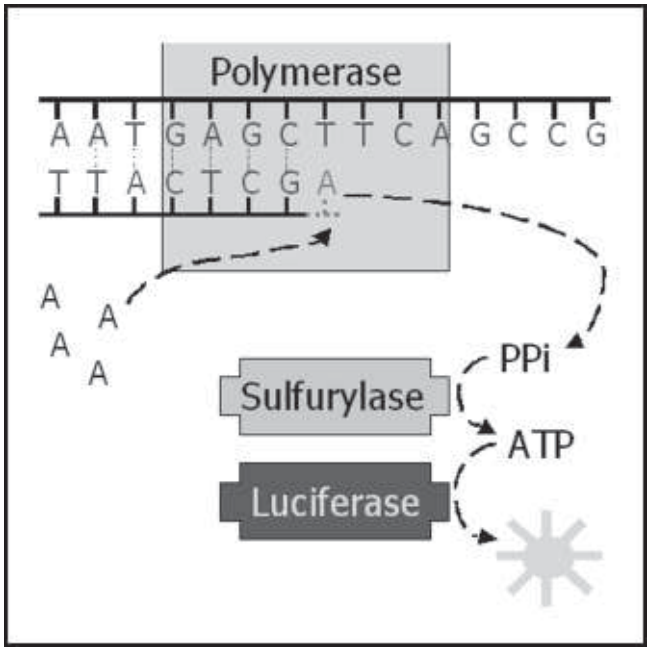

Figure 1: Pyrosequencing reaction steps.

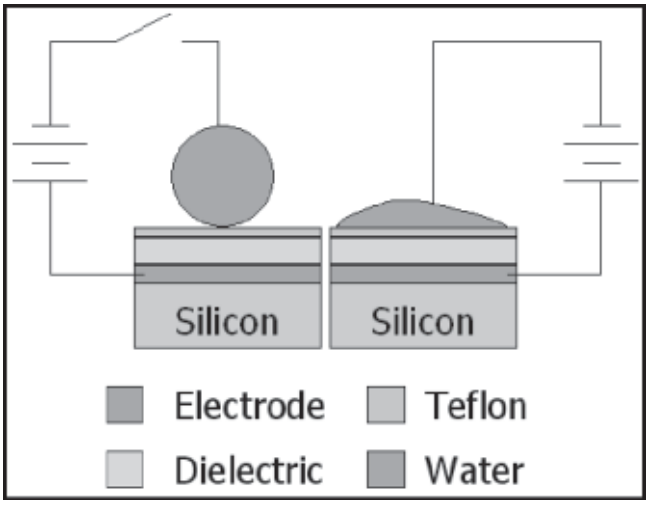

Figure 2: Electrowetting on dielectric device schematic.

taken to shrink the procedure, however, resulted in inaccurate DNA sequencing. When the process is performed on the macro scale, milliliters of the solutions are used, and mixing between the DNA and bases occurs due to turbulence. Shrinking the process down to microliters causes the solutions to become laminar. In a laminar flow regime, mixing between two liquids only occurs through diffusion at the liquid-liquid interface. For the reaction to happen, the free bases must diffuse through the entire solution to interact with the DNA. Since not all of the bases reach the DNA at the same time, sporadic light is produced causing the DNA to be incorrectly sequenced. To improve the mixing of the solutions, the use of electrowetting was proposed [2].

Electrowetting on dielectric (EWOD) is a process that uses changes in electric potential to affect the wetting properties of a liquid at a solid liquid interface. A typical EWOD device is diagramed in figure 2. A wafer is coated with a conducting material that acts as an electrode. The next layer acts as a dielectric and is usually composed of nitride. On top of this dielectric, a very thin coat of a hydrophobic material, such as Teflon, is deposited. When a liquid is placed on the chip, a droplet forms as the liquid minimizes surface area in contact with the hydrophobic layer. If an electric potential is applied between the electrode and the liquid, a capacitor forms across the dielectric [3]. The distribution of charge in the droplet causes the droplet to deform in order to minimize

Electrode Width	Electrode Shape
1.5 mm	Square
1 mm	Circle
0.75 mm	Triangle
0.5 mm	Resistor
0.25 mm	

Figure 3: Electrode specs for array chip.

the distance between the separated charges. When the electric potential is removed, the charge distribution disappears, and the liquid reforms into a droplet. If a series of electrodes are placed side-by-side, liquid will move from one electrode to the next as voltage is applied to each electrode in sequence [4]. Using this method, drops of DNA and bases could be merged and mixed on an EWOD device through droplet manipulation.

Procedure:

Two types of chips were designed using the mask-making program L-Edit. The first chips were fabricated using standard photolithography techniques and consisted of a silicon wafer with a large gold electrode covered with nitride. The other chips, which have yet to be fabricated, are designed with arrays of electrodes in various shapes and sizes. This chip will be used to determine the best size and shape of electrodes to transport liquid droplets. The size of the electrodes varies in width from 0.25 mm to 1.5 mm and the shape varies among those in figure 3. This chip will also aid in calculating the minimum voltage required to move assorted amounts of liquid.

Results and Conclusions:

On the silicon wafer, a drop of water was placed on top of the gold electrode. When an electric potential was applied between the droplet and the electrode, the drop did not change. However, when the drop was placed on the wafer in an area without the gold, applying a voltage of 20-40V caused the drop to deform, as shown in figure 4. The reason for this discrepancy rests with the nitride layer. The process used to deposit the nitride on the wafer did not provide an even coating. As a result, the nitride layer covering the gold was too thin to act as a dielectric. In areas were gold was not present, a capacitor formed, across the thicker nitride layer, between the water and the silicon, allowing EWOD to occur.

When the electric potential was removed from the deformed drops, the drops did not reform. This lack of reformation was due to the absence of a hydrophobic layer on top of the nitride. When the electric potential was removed there was no strong hydrophobic forces directing the droplet to reform; thus, the water remained flattened on the nitride layer.

While the droplet did not reform, this experiment did demonstrate our ability to create an EWOD device. With this knowledge, my research group will be able to fabricate the next chip which will move drops of water back and forth.

Acknowledgements:

I would like to thank my PI, Peter Griffin, and my mentor, Ali Agah, for their guidance and assistance in this project. Special thanks goes to Jane Edwards, Mike Deal, and the SNF staff for making my research experience beneficial and enjoyable.

References:

[1] Ronaghi, M. Genome Research. www.genome.org/cgi/ doi/10.1101/gr.150601. July 2, 2002.

[2] Pollack, M.G.; Shenderov, A.D.; Fair, R.B. Lab Chip. 2002, 2, 96.

[3] Decamps, C.; De Conick, J.; Langmuir. 2000, 16, 10150.

[4] Washizu, Masao. IEEE. 1998, 34, 732.

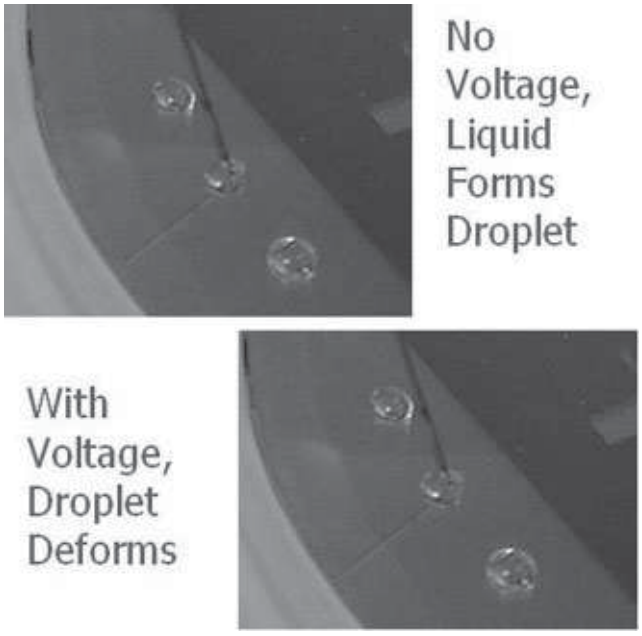

Figure 4: Droplet deformation with applied potential.

Simulation and Fabrication of Vertical Metal-Semiconductor-Metal Sub-Wavelength Aperture Photodetectors

Mark Elias, Materials Science and Engineering, The Ohio State University

Piero Pianetta, Dominik Schmidt, Electrical Engineering, Stanford University

elias.22@osu.edu, pianetta@slac.stanford.edu

Abstract:

In a Metal-Semiconductor-Metal (MSM) Photodetector, incoming photons create an electron-hole pair in a resistive silicon film placed between two electrical contacts that serve both to apply an electrical field and collect the resulting current. The photo-generated electrons experience a large electric field, which quickly sweeps them to the electrodes. In addition, the top electrode will be replaced with a series of sub-wavelength apertures in order to low-pass (wavelength) filter the incoming light and provide color selectivity.

Introduction:

A photodetector is a device used to transform electromagnetic waves into electrical signals that can be read out using electronic devices. In order to provide color sensitivity, the electronic output of the detector should preserve color information impinging upon the detector.

It is the intention of this paper to demonstrate a system that can be implemented in a standard CMOS process. The color separation method uses waveguides as low-pass filters that allow short light wavelengths through while blocking longer ones. To accomplish this, one must make a spatially distributed array of detectors, each designed to respond to a particular color.

Procedure:

The detector fabrication began with a low resistivity, p-type Si wafer that was ion implanted with BF_2 at a dosage of 10^{15} cm^{-2} and 32 keV. The doped wafer was then annealed in a nitrogen atmosphere at 950°C for 60 minutes. These steps turned the Si wafer into a conductive substrate, which will serve as the current collector.

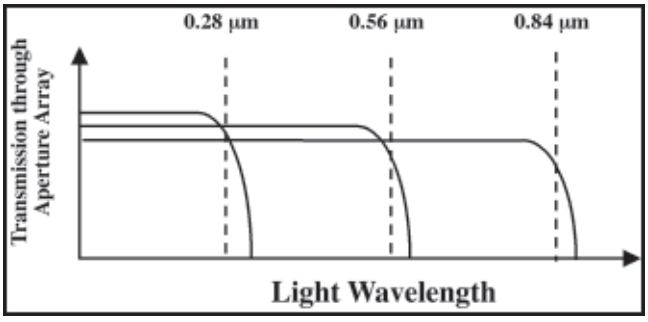

Figure 1. Predicted metal filter characteristics.

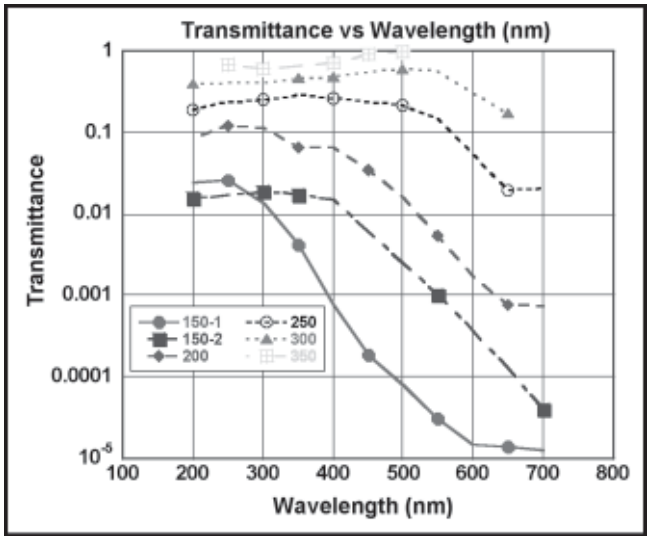

Figure 2. Simulated filter characteristics.

The MSM layers were deposited on the conductive substrate using various techniques which included the following: sputtering, electron beam evaporation, and PECVD. In each form of deposition, all three layers were deposited sequentially in order to avoid any oxidation formed by removal of the wafer from the vacuum chamber. The details behind each of the three forms of deposition go beyond the scope of this paper. First, a 0.5 μm film of Ti was deposited, then 1.0 μm Si, and finally 0.4 μm Al.

Once the MSM layers were deposited, a 0.25 μm layer of Zep 520-12 resist was spun on top of the Al layer. Test exposures were run on the Hitachi Electron Beam Lithography equipment in order to determine the proper dosage for the features being written, which ranged from 0.1 to 0.5 μm. This was the last step accomplished in the fabrication process, due to the demise of the e-beam writer.

Simulations of our design were run using a program called TEMPEST, which stands for "Time-domain Electromagnetic Massively Parallel Evaluation of Scattering from Topography.

The computer program solves Maxwell's equations:

$$\nabla \cdot E = \rho/\varepsilon_0 \qquad \nabla \times E = -\partial B/\partial t$$

$$\nabla \cdot B = 0 \qquad \nabla \times B = \mu_0 J + \mu_0 \varepsilon_0 \partial E/\partial t$$

using a time-domain finite-difference algorithm, where the electric and magnetic field nodes are spatially and temporally staggered over the three-dimensional topography of interest.

The topography used in the simulations was a simplified version of the intended design. Rather than simulate light passing through an array of apertures, simulations were done in 1.0 μm x 1.0 μm x 1.0 μm fields containing just one square aperture of the desired size. This method saved much computation time, and still produced valid data representative of our device.

TEMPEST produces an output consisting of the electric and magnetic field amplitudes that propagate through the aperture which are then analyzed using Matlab to produce the corresponding energy density.

Results and Conclusions:

In order to obtain an intuitive appreciation for the TEMPEST results, it is instructive to note that the relationship between the critical wavelength cutoff and the waveguide width is:

$$\lambda_{crit} = \frac{2a}{\sqrt{1-\frac{2\ln(10)}{3\pi}}}$$

where *a* is the waveguide width. From this equation, one can see that the critical wavelength is about 2.8 times the aperture size. A typical representation of transmission versus wavelength is displayed in Figure 1, which shows what would be expected for 0.1, 0.2 and 0.3 μm apertures. As can be seen from the figure, color differentiation may be achieved by subtracting the signals from adjacent holes. The TEMPEST simulations required one six-hour calculation for each wavelength and eleven wavelengths were needed for a typical transmission curve. The simulation results for aperture sizes of 0.15, 0.20, 0.25, 0.30 and 0.35 μm are shown in Figure 2. The noise in the curves comes from convergence errors due to the particular error tolerance used to reduce the computation time. However, the curves do show a high wavelength cut off consistent with the equation for the critical wavelength.

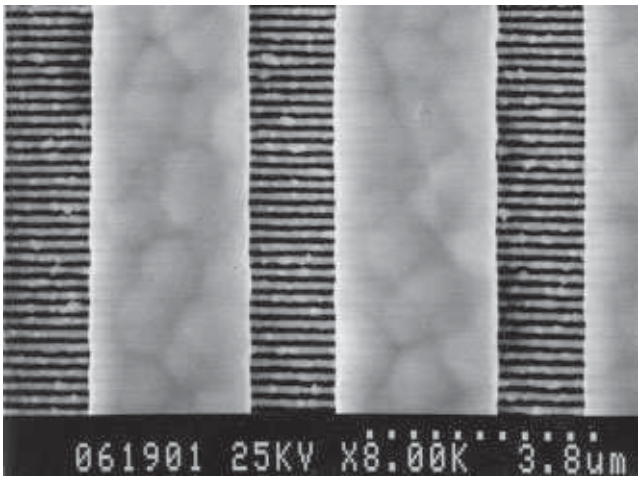

Figure 3. Diffraction Grating.

Since the unavailability of the e-beam lithography system limited our fabrication process, a test using a diffraction grating and PIN diode was done to simulate the vertical MSM PD. The diffraction grating, shown in Figure 3, had 0.1 μm openings, a size comparable to our intended design. The data from this test can be found in Figure 4. Note that the observed cut-off of 240 nm is in reasonable agreement with the value obtained from the critical wavelength equation. This gives confidence that the TEMPEST model will predict the behavior of the devices being fabricated.

Future Work:

The study of very thin absorption layers will be explored to improve the high-speed performance of the device. The thickness of the resistive Si film will play a key role in the efficiency of the device. By intuition, a Si film that is too thin will not fully absorb the incoming photons, while one too thick will allow for the electron-hole pairs to recombine before reaching the metal contacts. In both cases, a lesser photocurrent signal will be produced from the device.

Acknowledgements:

I would like to thank the NSF, Professor Pianetta and Dominik Schmidt for their support with this project.

References:

[1] D. Schmidt, Ph.D. Thesis, Stanford University (to be published).

[2] "Optical properties of polyvalent metals in the solid and liquid state: aluminum", J. Phys.: Condens. Matter 6 (1994) pp 2459-2474, Bernd Huttner.

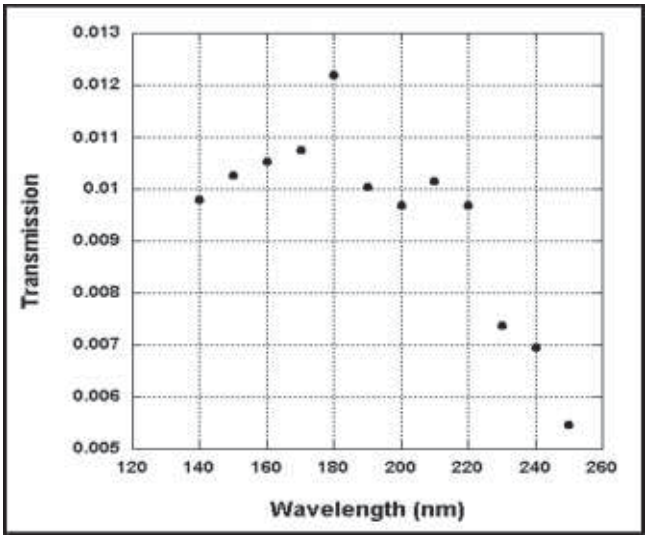

Figure 4. Transmission through 0.1 μm openings.

Patterned Multilayers for the Formation of Sub-Lithographic Features

Robert Gagler, Chemical Physics, University of Colorado at Boulder

Bruce M. Clemens, Aditi Chandra, Brennan Peterson, MSE, Stanford University

robert.gagler@colorado.edu, clemens@soe.stanford.edu

Abstract:

The current level of optical lithographic techniques for producing nanoscale structures is reaching a fundamental limit of roughly 200 nm. In order to explore new methods of producing structures smaller than this limit, we attempted a novel approach for creating chemically patterned surfaces for producing gold wires of roughly 10-100 nm in size.

Our method consisted of depositing a multilayer film (~10 nm up to 100 nm) of alternating amorphous silicon and amorphous gold/silicon alloy layers onto a silicon wafer. The structure was pattern-etched and then annealed to induce segregation of the gold from the Si. It was expected that surface energy considerations should drive the gold to the exposed edge of the multilayer, resulting in gold nanowires. In this work, we varied anneal temperature and thickness in order to investigate this process. Results were analyzed using SEM and TEM.

Introduction and Theory:

The underlying theory behind this work is related to surface energy considerations of the Au/Si system. This system has undergone extensive study by the professional and academic community. It is known that the Au/Si system undergoes segregation at elevated temperatures that depend on the particular alloy composition of the system [1]. Our intent in this work was two fold. First, we wanted to use a standard optical lithography process in combination with multilayer thin-film deposition to create sub-lithographic chemically patterned surface features using standard lithographic techniques. Second, we wanted to take advantage of the segregation characteristics of the Au/Si system to form self-assembling gold nanoscale wires on these sub-lithographic surface features.

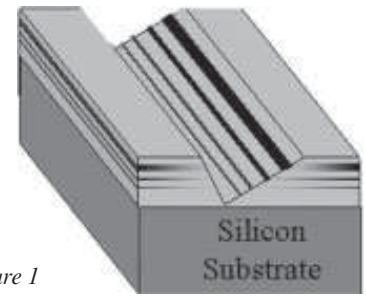

Figure 1

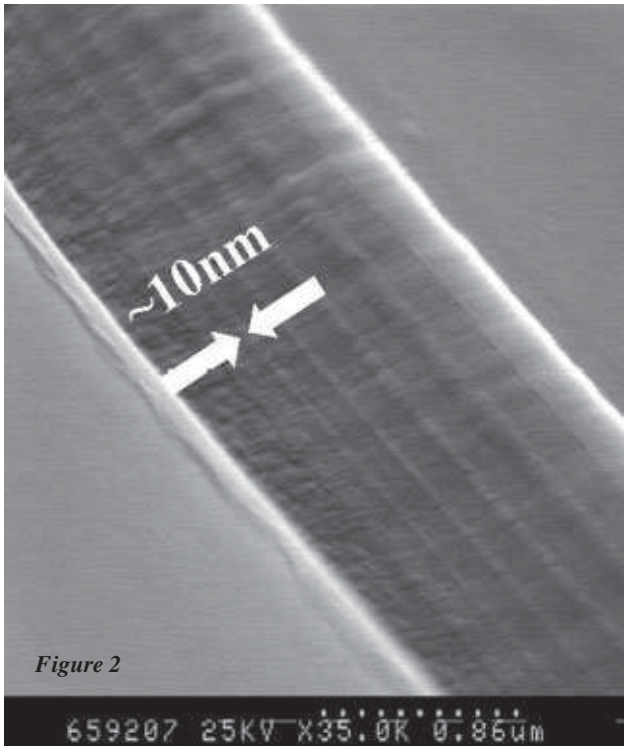

Figure 2

Procedure:

The first step in our process was to deposit a multilayer stack of alternating amorphous Silicon and Au_{25}/Si_{75} alloy layers on top of a silicon substrate using sputter deposition techniques. Using sputter deposition, we were able to adjust the film thickness to high precision (from a few angstroms up to hundreds of nanometers). In our work, however, we concentrated on film thicknesses in the range of 10 nm to 100 nm.

Following the multilayer deposition, we used standard lithographic masking techniques in combination with an angled ion etch to produce 1.5 μm wide grooves in the surface of the multilayer film. A schematic representation of the grooved multilayer surface is shown in Figure 1. In this figure, the dark horizontal lines represent Au/Si alloy layers (there are four layers, 10 nm, 25 nm, 50 nm and 100 nm) while the lighter gray areas represent amorphous Si layers (100 nm each). The exposed surfaces within the etched groove represent the sublithographic surface features that we were attempting to make.

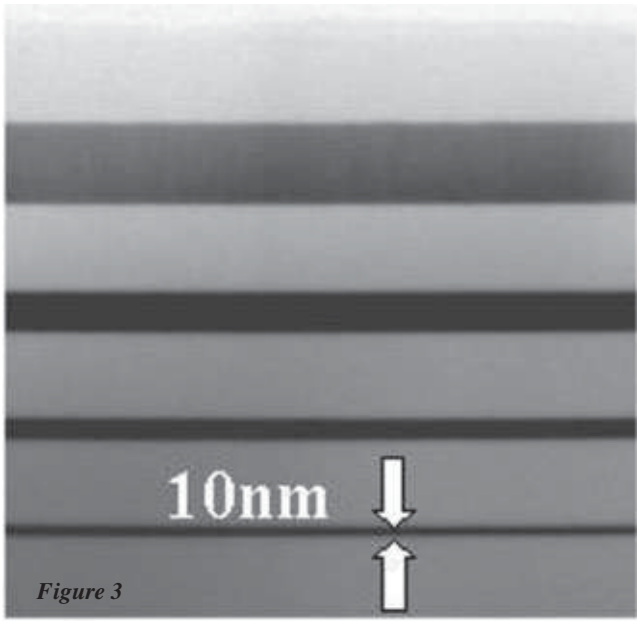

Figure 3

Following etching, the samples were annealed at 250°C for 30 minutes at atmosphere to promote segregation of the gold from the silicon. Figure 1 also attempts to convey the segregation process by which the formation of gold nano-wires was expected to proceed. Within the groove, the dark bands represent pure gold that has segregated from the alloy layer immediately behind it (represented by the fading of dark color behind these dark bands). This annealing step concludes our proposed process.

Results:

Following etching, SEM images were taken of the prepared surface grooves. This imaging revealed that we had in fact achieved our first goal of producing a chemically patterned surface with sub-lithographic scale patterning (the actual image is not shown here, but is represented in figure 1.)

Following etched sample imaging, the sample was annealed and imaged again to look for the formation of gold surface features on top of the chemically patterned surfaces. Figure 2 is a (35,000X) SEM image of one of the many patterned grooves on the surface of the multilayer film (identical orientation to figure 1). Visible within the groove are four bumps on the surface, the smallest of which is ~10 nm wide. These bumps were not present prior to annealing at 250°C. While SEM imaging did reveal that we had in fact produced surface features similar to what we were looking for, the composition of these features had to be determined by other means.

Following SEM analysis, two cross-sectional TEM samples were prepared to qualitatively determine whether the observed surface features were actually gold or not. One TEM image was taken of the sample prior to annealing (Figure 3) and one image was taken of the post-annealed sample (Figure 4). In figure 3, the dark horizontal bands correspond to Au_{25}/Si_{75} alloy layers while the light bands correspond to amorphous silicon layers. In the post-annealed image (Figure 4), we found that, rather than segregating to the surface, the gold preferentially segregated into the amorphous silicon. This result was unexpected and indicated that the surface features observed in figure 2 were not composed of gold, as we had suspected.

Conclusions:

TEM imaging of the post-annealed surface features led us to conclude that segregation of gold from the gold/silicon alloy to the exposed surface of that alloy was not preferential to segregation into the surrounding amorphous silicon, and that the observed surface features were believed to be an oxide formation. However, we did in fact create a chemically patterned surface with feature resolution well beyond the limit of current optical lithography (~10 nm). This process may be useful for producing surface features for controlling and observing chemical reactions along a nano-scale interface.

Future Work:

Additional investigation for the formation of features on these chemically patterned surfaces will be pursued. In particular, Au/Pt multilayers will be grown and etched, followed by a deposition of Co. Preferential dissociation and bonding may result in the formation of magnetic Co wires.

References:

[1] Andrée Rolland, Christophe Poisson, François M. d'Heurle and Ahmed Charaï, Stability of Interfaces in Gold-Silicon System Regarding Equilibrium Segregation. Microscopy Microanalysis and Microstructures Vol. 8, 1997.

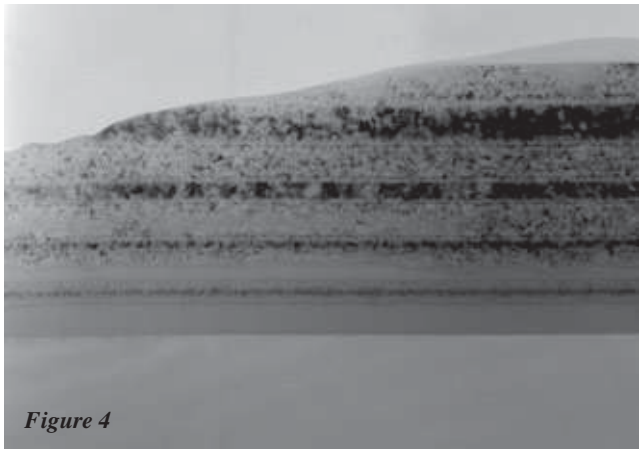
Figure 4

Teflon Coatings for Biochips

Eszter Horanyi, Engineering Physics, University of Colorado, Boulder

Peter Griffin, Ali Agah, Electrical Engineering, Stanford University

horanyie@colorado.edu, griffin@stanford.edu

Abstract:

There has been an increasing demand for hydrophobic thin films to act as a protective coating on biochips. In this project, different deposition conditions were used to deposit Teflon-like films. The films were then tested for their thickness, refractive index, and contact angle. The goal was to create a very thin film resembling bulk Teflon with an extremely hydrophobic surface that could be used for lab-on-a-chip applications.

Introduction:

The need for hydrophobic thin films has increased as biochips become a reality. Biochips can be employed to miniaturize chemical reactions commonly found in a biology lab, including genome sequencing. This would decrease the amount of solution needed for each reaction, and allow many reactions to be run side by side in a small amount of space.

To be hydrophobic, a surface must have a significantly lower surface tension that the liquid. One of the best known hydrophobic materials is bulk Teflon which a surface tension of 18 dynes/cm while water has one of 73 dynes/cm [1]. The goal was to create a Teflon like surface using plasma polymerized deposition with a fluorocarbon precursor. Depending on the deposition conditions, a Teflon like film with long -CF_2- chains could be deposited as long as the precursor gas had a carbon to fluorine ratio of at least 1:2. The ideal film was as thin as possible while still maintaining the desired hydrophobicity [2].

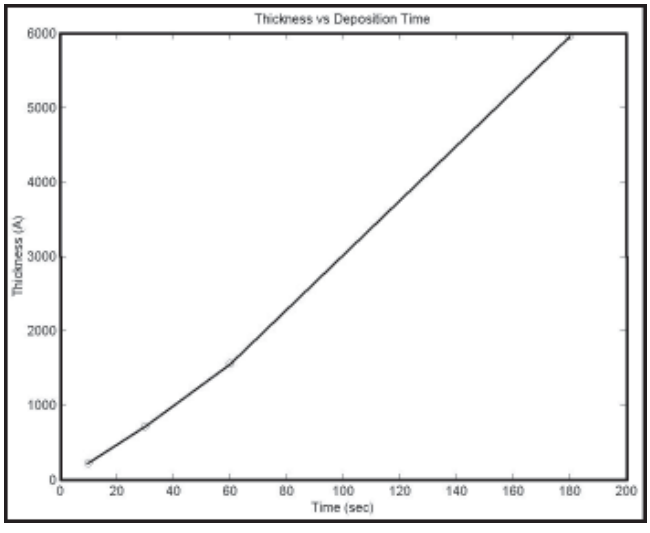

Figure 1: Graph of thickness versus deposition time.

Procedure:

A plasma etcher was used to polymerize a fluorocarbon source gas and perform the depositions. This etcher used a C_4F_8 source gas. Several different deposition variables could be controlled with this machine including deposition time, coil power, platen power, and flow rate. Film quality was determined by refractive index and contact angle measurements. An ellipsometer was used to measure the refractive index. The goal was to create a film that had the same characteristics as bulk Teflon, with a refractive index of 1.29 and a contact angle of 120 degrees.

Results and Discussion:

The deposition rate of the film varied widely depending on the conditions. It was seen that the deposition rate was constant for deposition times up to three minutes under identical conditions as seen by Figure 1.

Coil power had the greatest influence on the deposition rate. When the coil power was low, the deposition rate was controlled primarily by the availability of fresh monomer. When the coil power was

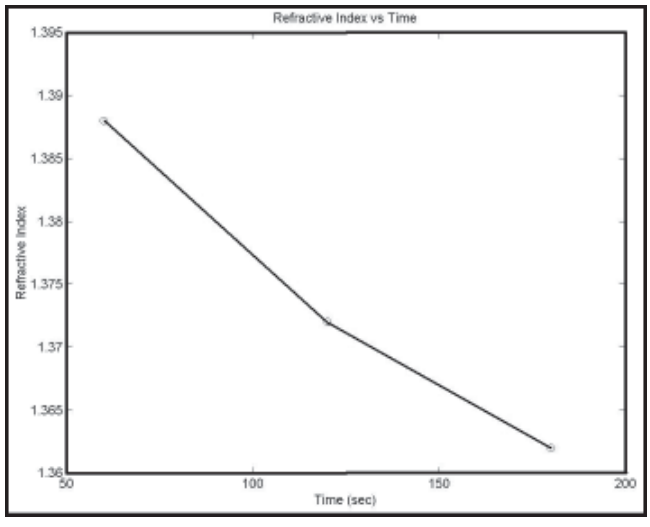

Figure 2: Graph of refractive index versus deposition time.

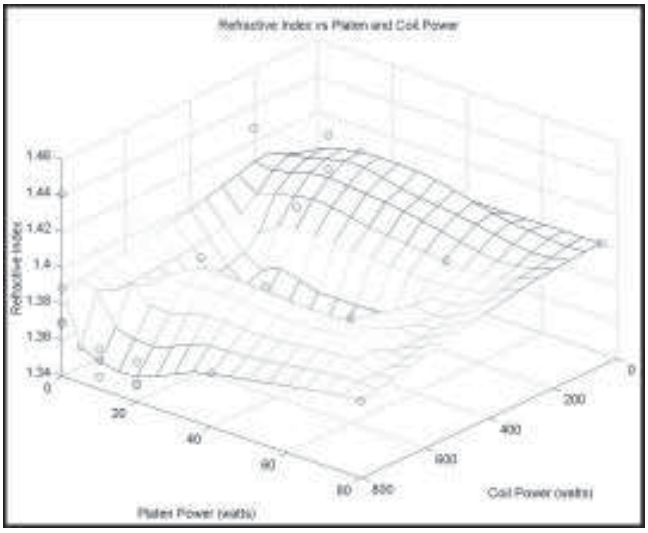

Figure 3: Graph of refractive index versus coil and platen power.

very high, the deposition rate was controlled by rate of formation of polymer precursors. Very high coil power also caused an increase in the deposition of neutral species that did not get a chance to become ionized and polymerize with the rest of the gas. The deposition of neutral species was unfavorable because they would not become incorporated into the long -CF_2- chains that were desired [3].

Flow rates caused a difference in the deposition rate. At low flow rates under low power conditions, the supply of fresh monomer was limited and the deposition rate decreased. Figure 2 shows the relationship between coil power and platen power.

Platen power affected the deposition rate in two ways. The ions created by the platen power bombarded the surface of the wafer and the surface of the growing film and created active sites which allowed for film growth [4]. High ion bombardment could cause etching both of the silicon wafer and the deposited film, both of which were undesirable [5].

While the refractive index of a film was not a good indicator of its hydrophobicity, it was a good tool for examining whether films differed in their composition.

The thickness of the film had a major effect on the refractive index, as did the deposition time. When the deposition time was cut for certain deposition conditions, the refractive index of the thinner films rose drastically. Figure 2 shows the relationship of the refractive index of the films to the time of the deposition.

Platen power also affected the films. At low platen power, very little polymerization occurred. These films had a high refractive index. When the platen power was very high, the films were constantly bombarded by ions, and cross-linking occurred even once the films were deposited [6]. This also led to a higher refractive index.

Figure 3 illustrates the relationship between refractive index and coil and platen power.

Contact Angle: The hydrophobicity of a surface was dependent on the surface tension of film. The goal was to create a film that has a very low surface tension compared to water. Figure 4 illustrates the contact angle achieved on the Teflon-like film.

While the refractive index of a film was indicative of many film properties, it was not able to predict the hydrophobicity of a film. It appeared that regardless of the refractive index, the contact angle of most fluorocarbon films deposited hovered around 108 degrees.

The thin films with low refractive indices were the ones that were deposited at a low flow rate, a medium coil power, and a medium amount of platen power. It took the right combinations of all three variables to create a film that resembled bulk Teflon.

Acknowledgements:

I'd like to thank Peter Griffin for his guidance in the project, Nancy Latta and the entire SNF staff, and NSF for funding the project.

References:

[1] Rudie, Brian. "Hydrophilicity and Hydrophobicity", http://www.osmonics.com, August 16 2002.

[2] P.F Man, B.P Gogoi, and C.H. Mastrangelo, "Elimination of Post-Release Adhesion in Microstructures Using Thin Conformal Fluorocarbon Films," IEEE, pp. 55, 1996.

[3] Ibid., pp55.

[4] A.J. Bariya, Deposition Kinetics and Characteristics of Fluorocarbon Plasma Polymer Films and Their Role in Dry Etching. Ph. D Thesis, Stanford University, CA, 1990.

[5] Ibid.

[6] G. W. McLauglin, Microfluidic and Biosensor Applications of Fluoropolymer Films, Ph. D Thesis, Stanford University, California, May 2001.

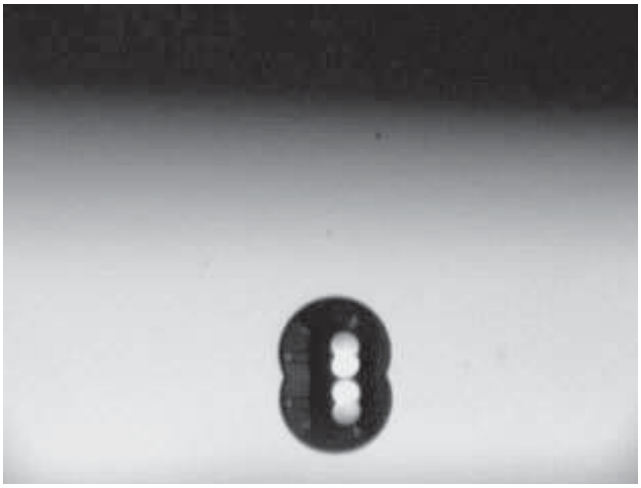

Figure 4: A drop of water on a Teflon coated silicon wafer with its reflection.

Transient Induced Conductivity and Energy Dissipation in Electron Beam Lithography

Scott Sheridan Howard, Electrical Engineering, University of Notre Dame

Dr. R. Fabian Pease, Electrical Engineering, Min Bai, Applied Physics, Stanford University

showard@nd.edu, pease@cis.stanford.edu

Abstract/Introduction:

Electron beam induced conductivity (EBIC) can account for charge leakage from a resist to the substrate during electron beam lithography. E-beam lithography charging models will have to account for such leakage in order to properly understand positional errors caused by charging during e-beam lithography. The EBIC region also closely follow the energy dissipation region of the e-beam, which will be studied by mapping out the region of secondary electron generation from e-beam energy dissipation. Metal-oxide-semiconductor test structures will be fabricated to measure this transient conductivity by measuring the current through the region when biased. The design of the test structures will be guided by Monte Carlo modeling of electron-solid interactions.

Due to the time constraints of the summer, only dissipation profiles in oxide could be studied. A polymethyl methacrylate (PMMA) process has been developed using this procedure and measurement technique.

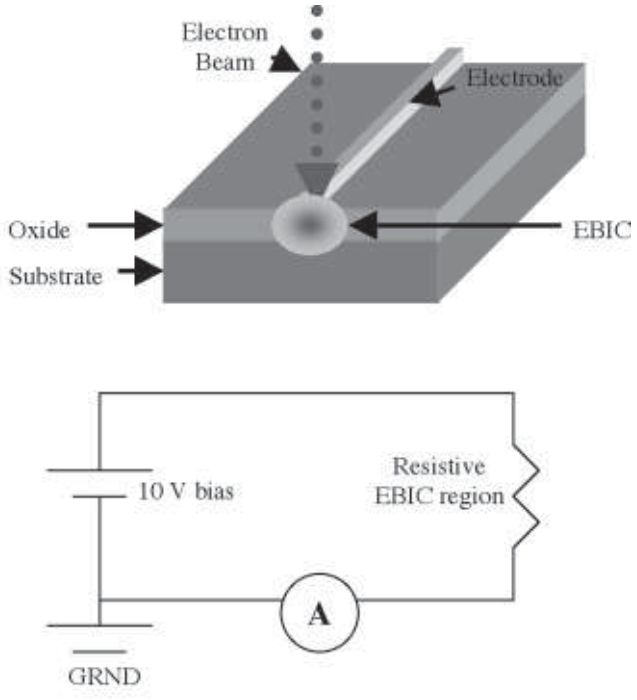

Figure 1: Diagram of MOS test structure.

Procedure:

307Å thick Ti electrode fingers were deposited onto 2 µm thick silicon dioxide grown on a Si substrate. The electrode was biased at $^{-}$10 V with the substrate grounded and connected to an oscilloscope to measure current. An e-beam was spot exposed on the oxide surface through the center of an electrode finger. (See figure 1.) Current was then measured between the electrode and the substrate. EBIC current was found by subtracting out the unbiased beam contribution of the measured substrate current from the $^{-}$10 V biased combined EBIC and beam current measured through the substrate.

To find the energy dissipation profile, different width electrodes ranging from 1 to 20 µm were deposited, and the EBIC current of each was analyzed.

Results Discussion:

EBIC is follows the following relationships:

$I = V/R = V/(\rho L/A) = (A\sigma V)/L$

$\sigma = L*I/(A*V)$

in these experiments:

$A = w*l$

$L = d$

$\sigma = d*I/(w*l*V)$

$I = (w*l*\sigma*V)/d$

(I = measured current from electrode to substrate, R = resistance in oxide, V = bias voltage $^{-}$10 V, ρ = resistivity in EBIC region, L = depth of EBIC region, A = lateral cross sectional area of EBIC region, σ = EBIC, w = electrode width, d = oxide thickness 2µm, l = lateral length of EBIC region constant for each beam energy.)

By keeping bias voltage constant and increasing the width of the electrode, an increase in current is expected until the entire EBIC region lies under the electrode, at which point the current saturates. (See figure 2.) At widths above the saturation point, increasing electrode width will not increase the total current measured since the cross-sectional area of the EBIC current path remains constant.

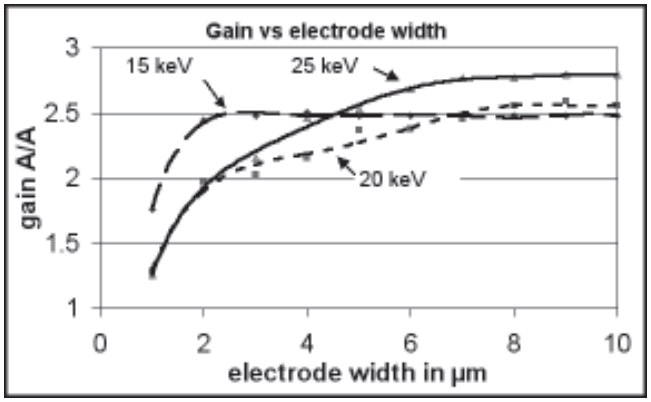

Figure 2: Current gain (EBIC current at -10 V bias)/ (beam current) as a function of electrode width.

As the electrode width increases to the saturation point, current will increase at a decreasing rate since the EBIC effect decreases as distance from the exposed spot increases. By analyzing the rate at which the EBIC effect decreases, the energy dissipation profile can be obtained. (See figure 3.)

To find the percent of total energy that is dissipated between the edge of width 1 and the edge of width 2, the percentage of the total number of carriers generated between widths 1 and 2 must be found. The number of carriers generated is proportional to conductivity which can be calculated by measuring the current and cross-sectional area of the current.

In these experiments, the cross sectional area under the larger electrode that does not lie under the smaller electrode is constant as electrode width increases incrementally by 1 µm. So conductivity is proportional to the current that flows through that region:

$$E_{12} \propto N_{12}$$
$$\sigma = q(\mu_p * N_v + \mu_e * N_c) \propto q*\mu*N$$
$$N_{12} \propto \sigma_{12}$$
$$\sigma_{12} = (I_2 - I_1)*L/(V*A_{12})$$
$$\sigma_{12} \propto I_2 - I_1$$
$$E_{12} \propto N_{12} \propto \sigma_{12} \propto I_2 - I_1$$

(E_{12} = Energy dissipated between electrode widths 1 and 2 , N_{12} = carriers created between widths 1 and 2, $\sigma_{12} = \sigma$ between widths 1 and 2, I_1 = current that flows through electrode of width 1, I_2 = current that flows through electrode of width 2, L = d = 2 µm constant, V = -10 V bias constant, A_{12} = area between widths 1 and 2 = 1 µm x a constant dependant on electron beam excitation energy.)

Finding the ratios of current in each of the areas between electrodes gives us the ratios of energy dissipation in each of those areas. (See figure 4.)

The ratios of currents at different distances from the exposed spot give us the ratios of energy beam dissipation. The probability density function of electron energy dissipation can be determined from the e-beam dissipation ratios. This probability density function follows a Gaussian distribution with standard deviations of 0.929, 0.678, and 0.524 for the 25 keV, 20 keV, and 15 keV beam energies respectively.

These are consistent with Monte Carlo electron-solid interaction models which predict a 1 µm beam widening in silicon dioxide per 5 keV beam energy.

Conclusion:

The EBIC and energy dissipation profile in e-beam lithography have been mapped out. This data will be incorporated into models that will calculate resist charging during lithography which will improve e-beam technology by reducing positional errors due to charging.

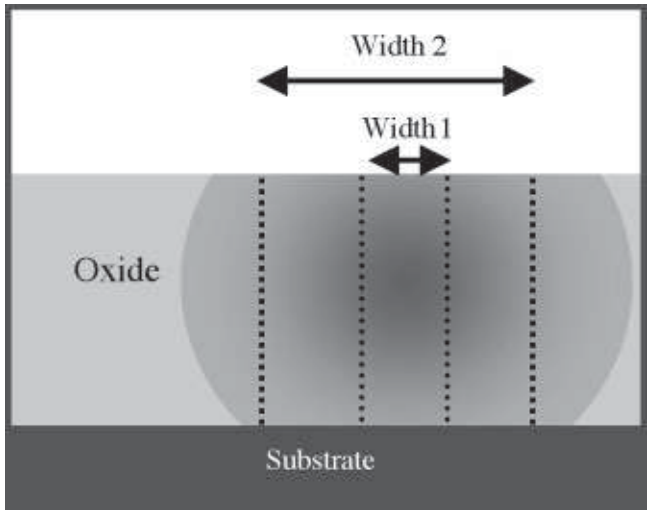

Figure 3, above: Cross section of EBIC region. Width 1 and 2 represent two different width electrodes. The doted lines show area under each of the two electrodes in which EBIC current is measured.

Figure 4, below: Probability of electron energy dissipation as a function of distance from exposed spot.

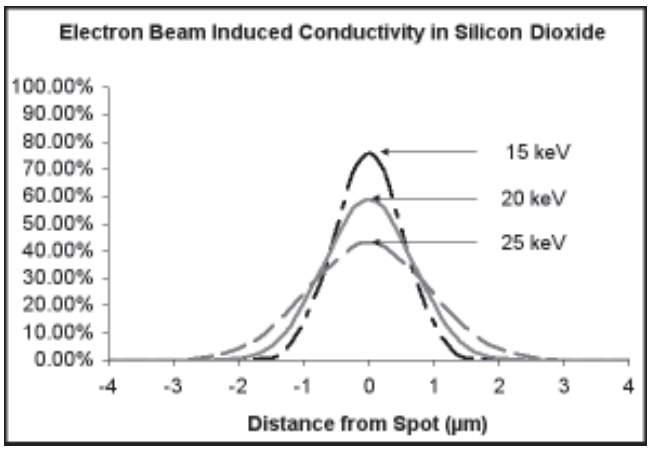

Design, Fabrication, and Testing of Piezoresistive Pressure Sensors Using Carbon Nanotubes

John Liu, Computer Engineering, University of California at Irvine

Dr. Hongjie Dai, Chemistry, Randy Grow, Applied Physics, Stanford University

jwliu@uci.edu, hdai1@stanford.edu

Abstract:

Single-walled carbon nanotubes (SWNTs) have been shown to exhibit the piezoresistive effect, in which the electrical resistance of the material changes under mechanical deformation. Therefore, piezoresistive pressure sensors can be designed and built by mechanically deforming SWNTs as electrical wires. We performed back side etching on four-inch wafers and created suspended square polysilicon membranes on the front sides. SWNTs were grown at the centers and the edges' midpoints on each membrane. Pressure was applied uniformly on the membranes and the resistance change in the SWNTs was observed.

Introduction:

Traditional silicon piezoresistive pressure sensors are highly temperature-dependent. One alternative material that has also been shown to exhibit the piezoresistive effect is the singled-walled carbon nanotube (SWNT) [1], which is a single graphene sheet rolled into a cylinder. We grew SWNTs on suspended polysilicon membranes. Air pressure was applied uniformly to press down on the membranes, causing the tightly attached SWNTs to deform. The current passing through the SWNTs was measured with respect to continuous time.

Theory:

Timoshenko's equations for large deflection of clamped square plates [2] were used for the design of membrane:

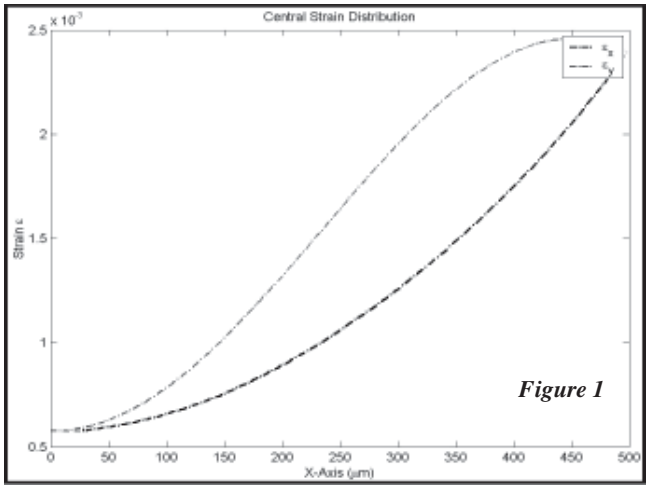

Figure 1

$$\omega_0 = 0.802a(qa/Eh)^{(1/3)}$$

$$\varepsilon = 0.462(\omega_0/a)^{(1/2)}$$

$$\sigma = 0.396((q^2)(E)(a^2)/(h^2))^{(1/3)}$$

where ω_0 is the deflection at the center of the membrane, a is half of the side length, q is the pressure applied, E is the Young's modulus, h is the thickness, ε is the strain at the center, and σ is the tensile stress. We know the Young's modulus and yield strength of polysilicon, and the applied pressure is 1 atm and the strain should be approximately 0.1% for good pressure sensors. Solving for the dimensions of the membrane, we obtained two designs, 100 μm x 100 μm and 1000 μm x 1000 μm.

A MATLAB program that simulates the strain at various points as a function of their distances from the center of a membrane [3] was employed. As figure 1 shows, the strain of the 1000 μm x 1000 μm membrane peaks near the midpoints of the edges. For the 100 μm x 100 μm membrane, the strain peaks at the midpoints on the edges.

Procedure:

A 3-mask process will be presented here. Double-side-polished R-prime silicon wafers having a mean thickness of 374 μm were used as our substrates. A layer of 0.2 μm thick oxide, 2 μm thick polysilicon, and 0.2 μm thick nitride were deposited on both sides of a substrate, consecutively. The back side nitride was patterned by photolithography and etched.

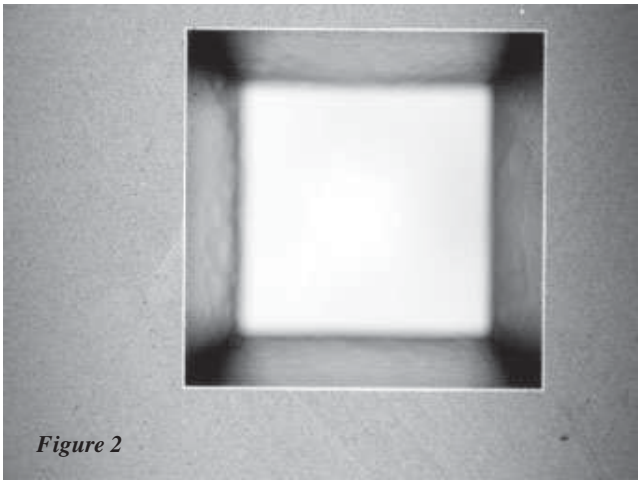

Figure 2

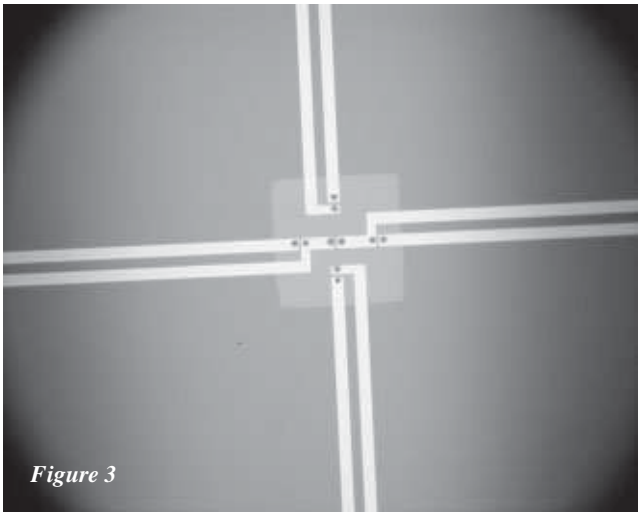

Figure 3

Next, the backside polysilicon was plasma etched. The backside oxide was etched using HF (hydrogen chloride). At this point, the silicon substrate was not yet etched, as the fragile membrane created would likely be broken during the subsequent process steps.

A layer of molybdenum was then deposited on the front side of the substrate, followed by its patterning and lift-off to form the metal electrodes. The catalyst was deposited over the metal electrodes, patterned using PMMA (polymethylmethacrylate), and etched, creating catalyst islands from which the SWNTs would grow. Another layer of PMMA was coated on the front side to protect the catalyst islands and metal electrodes before we proceeded to further backside etching.

Backside etching was performed on the silicon substrate using KOH (potassium hydroxide). The silicon crystalline structure caused KOH to etch through the substrate anisotropically, creating a trapezoidal cavity as the vertical etching rate is much greater than the lateral etching rate. After removing the front side oxide, a suspended square polysilicon membrane was created (figure 2). The protective layer of PMMA was then lifted off by acetone. Figure 3 shows the front side of our design at this point. Each individual device was separated for growth of SWNTs. Wire bonding was done after the growth.

Probing each device was performed to determine the connection between each pair of metal electrodes. The SWNT could be either metal or semiconductor, or there could be no connection at all. The devices that showed semiconductor connection at the probe station were taken to the AFM (atomic force microscopy) for further confirmation. Figure 4 shows the AFM image of a SWNT connection between two metal electrodes.

Each working device was properly set up in a sealed gas chamber with an internal breadboard and external cable connections to the multi-scope. Air was pumped into the chamber and pressure was applied to the membrane. The scope was set to display the current as the function of continuous ongoing time.

Results and Conclusions:

When air pressure deformed the SWNTs, a decrease in current on the multi-scope was observed. This is an indication of an increase in resistance. Moreover, when the gas was pumped out and the membrane was restored its original condition, the current rose back to the same level. This showed that the process is reversible.

Further investigations on the potential of SWNTs as piezoresistive pressure sensors can be carried out with our designs. Other important factors to be characterized include the gauge factor, temperature dependence, noise factor, etc. The buckling of the membranes, the positions of the devices on the membranes, and the growth condition of SWNTs are some areas to be improved.

Acknowledgements:

I would like to thank Professor Hongjie Dai for being supportive and inspiring, my mentor Randy Grow for being instructive, my partner Robert Caldwell, Qian Wang and other cordial Dai lab members. I would also like to thank Dr. Michael Deal and Jane Edwards for their coordination at the SNF site, and NSF for funding such an enriching summer experience.

References:

[1] T. Tombler, C. Zhou, L. Alexeyev, J. Kong, H. Dai, L. Liu, C. Jayanthi, M. Tang, S. Wu, "Reversible nanotube electro-mechanical characteristics under local probe manipulation," Nature 405 (2000) 769.

[2] S. P. Timoshenko and S. Woinowsky-Krieger, Theory of Plates and Shells, 2nd ed. New York: McGraw-Hill, 1970.

[3] L. Lin. (1998), Simulation Program for Piezoresistive Pressure Sensors. [Online]. Available HTTP: http://www.me.berkeley.edu/~lwlin

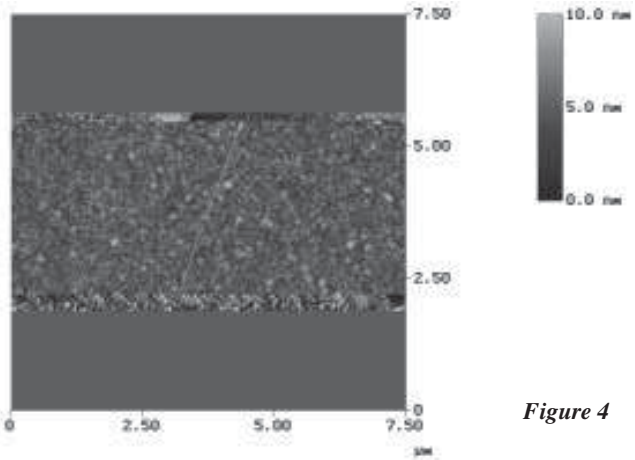

Figure 4

Controlled Thinning of AlGaAs\GaAs Photocathode Structure

Curtis Mead, Electrical Engineering, University of Minnesota-Twin Cities

R. Fabian W. Pease, Rafael Aldana, Electrical Engineering, Stanford University

mead0062@tc.umn.edu, pease@cis.stanford.edu

Abstract:

Bulk GaAs material is selectively removed by a controlled wet chemical etching process, creating $Al_{0.3}Ga_{0.7}As$\GaAs photocathode membranes. Two different etchants are employed; 1 sulfuric acid: 8 hydrogen peroxide: 1 water, and 10 citric acid : 1 hydrogen peroxide.

Measurements are made using an optical microscope periodically throughout the fast etching cycle (sulfuric acid and hydrogen peroxide). When the GaAs layer was down to 30 µm, further etching was done with a slower, more selective etchant (citric acid and hydrogen peroxide). During the slow etching cycle, the intensity of transmitted light (800nm) through the photocathode membrane is used as an indication of when the entire GaAs substrate had been etched through.

Approach:

A controlled process to create GaAs membranes is important for the creation of high efficiency transmission-mode photocathodes. Wet chemical etching has been shown to be successful in creating "windows" of AlGaAs on GaAs substrates [1]. Additionally, the process may be controlled with the use of a light source (800 nm) and photodetector.

The photocathode structures consist of a 3 µm layer of $Al_{0.3}Ga_{0.7}As$ and 100 nm layer of GaAs on the surface of a GaAs substrate. To use the photocathodes in transmission mode, the bulk GaAs under the active area must be removed. Etching of the GaAs is done with a 10:1 mixture of citric acid (50% by weight) and hydrogen peroxide (30%) and also with an 1:8:1 mixture of sulfuric acid, hydrogen peroxide and water. The citric acid mixture etches more slowly than the sulfuric acid mixture but is expected to have higher selectivity and result in a smoother surface.

In the GaAs membrane creation process, the GaAs substrate containing the photocathode is mounted top down on a glass slide. Then, it is surrounded on the edges with black wax, leaving a 2-3 mm opening on the underside of the GaAs substrate. This whole structure is put into the sulfuric acid etching solution. The GaAs substrate is removed after 60 minutes and the amount etched is determined using an optical microscope. The additional etch time required is calculated by averaging the etch rate over the first 60 minutes and then dividing the amount left to etch by the average etch rate. The sample is placed into the etching solution again for the amount of time that will result in leaving about 30 µm of GaAs substrate material. Then, the slow etch cylce is started.

A photodetector is placed inline with the GaAs substrate, sitting in the citric acid etchant, and a filtered arc lamp beam (figure 1). The photodetector and light from the arc lamp are employed in order to recognize when the entire GaAs substrate has been successfully removed. The light intensity seen by the photodetector is recorded during etching. Monitoring the intensity of the light will give an indication of when the etching process has entirely removed the bulk GaAs material.

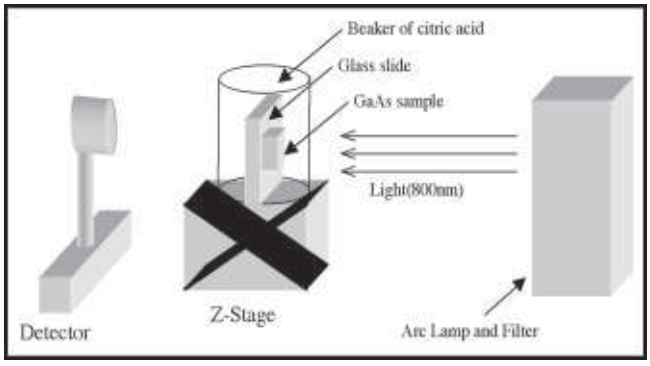

Figure 1. Slow citric acid etch.

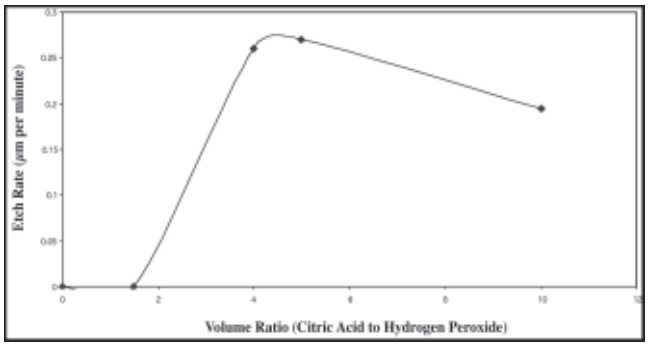

Figure 2. Etch Rates: Citric acid (50% by weight) and hydrogen peroxide (30%).

GaAs is opaque to 800nm light but $Al_{0.3}Ga_{0.7}As$ has a bandgap much larger than 800 nm and is transparent to this wavelength. The citric acid mixture used should etch preferentially etch GaAs faster than $Al_xGa_{1-x}As$ where x is less than about 40%. A selectivity ratio of 95 has been shown for a 10 to 1 solution of citric acid to hydrogen peroxide [2].

Results:

The sulfuric acid solution can etch an entire 600 µm wafer in eighty to ninety minutes if mixed properly and stirred. Unfortunately, initial etch rates vary from 11 µm/min to 7 µm/min. The cause of this variation has not been positively determined but it may result from small volume ratio variations or differences in mixing procedures. The sample being etched must be monitored carefully so that it is not over etched. Also, etch rate decreases over time. This may be attributed to decreasing hydrogen peroxide ratios over the entire etch period.

The citric acid mixtures etched well without stirring at volume ratios greater than 4 parts citric acid to 1 part hydrogen peroxide. Etching was not apparent with lower volume ratios (figure 2).

Controlling the etch by using transmitted intensity of 800 nm light through the sample has been shown to work conceptually. The process was able to controllably etch through an entire GaAs substrate. No actual photocathode samples have been run through the process yet.

Conclusion:

Creation and testing of this GaAs membrane making process will allow successful and repeatable construction of transmission photocathodes.

The process presented has been shown to work conceptually on dummy samples. Etching profiles can be examined to determine when the GaAs is mostly removed during the fast etch cycle. Then a slower etching solution can be used in conjuction with a light source and photodiode to precisely etch the last 30 µm. Eventually, automation is possible by using the photodiode to have the process stop once enough light is transmitted through the $Al_{0.3}Ga_{0.7}As$/GaAs membrane.

References:

[1] LePore, J. Appl. Phys. 51(12).

[2] R. A. Logan and F. K. Reinhart, J. Appl. Phys. 44, 4172 (1973).

Design and Fabrication of an AlGaAs Oxidation System

Schuyler Mudge, Physics, University of Washington - Seattle

James S. Harris, Evan Thrush, Electrical Engineering, Stanford University

smudge@u.washington.edu, harris@snowmass.stanford.edu

Abstract:

One of the critical steps of producing a vertical cavity surface emitting laser (VCSEL) is the processing of the current aperture. This current aperture is processed through the selective oxidation of aluminum gallium arsenide (AlGaAs) (a VCSEL cross-section is seen in Figure 1). Oxidation of the current aperture in a conventional oxidation furnace is unstable and unpredictable, as there is no method in which you can consistently and accurately control the oxide thickness.

The goal of this project was to optimize the selective oxidation of VCSELs by making it more accurate, stable, and predictable without the need for calibrating the oxidation speed. This was done by building a furnace with a glass viewport and a microscope hooked up to a viewing screen. This enables real-time viewing of the oxidation process and eliminates the need for calibration.

Background:

VCSELs are a new technology in semiconductor lasers in which the beam is emitted normal to the surface of the wafer. One of the reasons for optimizing the processing of VCSELs is the cost of production is less than the older edge-emitting lasers (EEL). EEL beams are emitted parallel to the surface of the wafer so they must be cleaved out of the wafer. This is why processing is more expensive for EELs than VCSELs which are emitted normal to the surface.

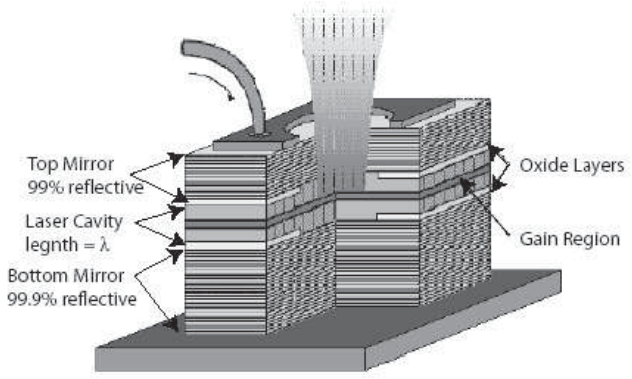

Figure 1: A cross-section of a VCSEL showing the oxide layers.

VCSELs also have a smaller divergence angle than EELs (Figure 2). VCSELs produce tighter focused beams, which allows for easier coupling to optical fibers. Figure 2 shows the higher VCSEL vs. EEL density. Production of VCSELs in the tens of thousands per wafer is highly feasible. VCSELs are also circularly symmetric, whereas EELs are highly asymmetrical. VCSELs make 2-dimentional arrays possible due to their symmetry.

One of the more challenging parts in the production of the VCSEL is making the current aperture. Desired apertures are 5 μm in diameter. Due to the desired accuracy, it is necessary to be able to have control over the oxidization. Conventional furnaces must run at least two days to achieve steady state due to the need to achieve water absorption equilibrium with the graphite lining prior to oxidizing in a controlled process. Changes in the shape, size, and spacing of the VCSEL, also makes it complicated to accurately calibrate the oxidation of the aperture in a conventional furnace.

Process:

The oxidation furnace was designed to include a temperature controller, light source, imaging system, chemical environment, and ventilation system. The oxidation rate is a slow and visible 2 μm/hr at around 400°C. With an imaging system, there is no need for accurate calibration, as you can view in real time the progress of the oxidation front.

A white light source with an infrared filter is used to illuminate the sample. The reflected light is fed to a CCD camera onto a viewing screen. The band gap of GaAs is 870 nm, so in order to more easily view the difference between the oxidized and unoxidized regions of the VCSEL, a filter of at least 750 nm was needed. The chemical environment included a nitrogen bubbler fed through boiling water. The chamber of the furnace was vented so the water will not condense on the glass viewport and block out the imaging system.

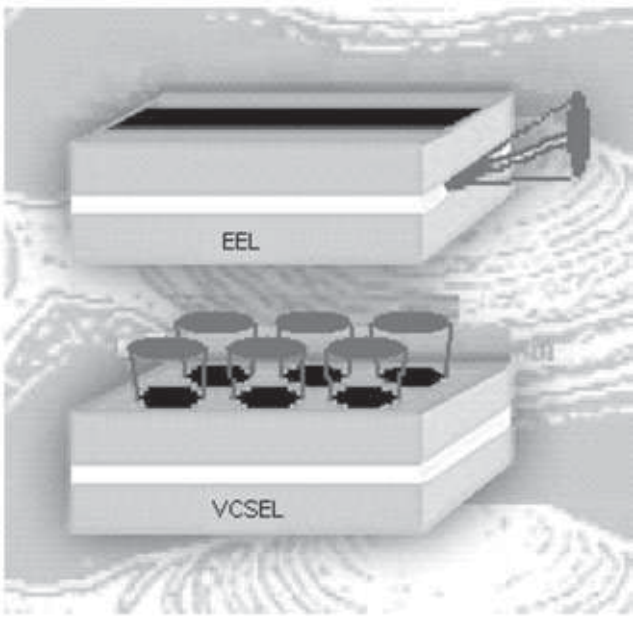

Figure 2: Comparison of a traditional edge-emitting laser (EEL) and a VCSEL.

Results:

The majority of the time was spent designing, procuring parts, building, and solving start up issues. Only one week of system testing was possible.

During the first test run of the system (with no samples or nitrogen system running) the MACOR ring supporting the graphite chuck cracked at 360°C while ramping at 1000C/hr. Later test runs were of the completed system, including samples.

The first two runs were both substantially over oxidized. In the third run, the sample was heated up to 400°C for 10 minutes. This showed a small, although insignificant, amount of oxidation. The heater cracked and broke while the furnace was ramping up during the fourth run. This run was planned for 10 minutes at 410°C. It was expected to produce a good oxidation thickness.

Conclusion:

VCSELs greatly improve on the weakest points of EELs. This motivates the need for consistent results in the oxidation processing. The furnace shows the capability to increase the control over the oxidation reaction. The system controls then allow small features to be defined more precisely than a conventional furnace.

Future work on the oxidation furnace should include a new design for a chuck since the MACOR supporting the graphite chuck cracked during test runs. Furthermore, new heater designs that can withstand higher temperatures and currents need to be researched. This system could also use heating insulation to keep the outside of the chamber from getting too hot and damaging the sensitive optical equipment.

Acknowledgements:

I would like to thank the NSF for the funds that made this program possible and the NNUN for putting together this wonderful program. Also, I would like to thank Professor James S. Harris and my mentor Evan Thrush for their help and support throughout this program. Much thanks to Wistey, James Conway, and the staff at SNF for taking time to help me out and answer my questions. Thank you, Laura Zager, for being such a wonderful partner on this project. To the rest of the Stanford REU students, I had a fabulous time, thank you for the memories and your support.

Susceptibility Analysis of Patterned Magnetic Thin Films

Michael Shearn II, EE/Physics/Mathematics, Southern Methodist University

Dr. Shan Wang, MSE, Jason Jury, Electrical Engineering, Stanford University

mshearn@mail.smu.edu, sxwang@stanford.edu

Abstract:

The aim of this investigation is to fabricate and characterize magnetic thin films patterned into rectangles with dimensions in the 3-10 μm range. These films were produced using standard photolithographic techniques at the Stanford Nanofabrication Facility.

The magnetic domains were visualized using magnetic force microscopy; vibrating sample magnetometer measurements were also taken to characterize the patterned film. These measurements are supplemented with numerical simulations to investigate the accuracy of existing models. Graphs of measured and modeled values are qualitatively similar but differ numerically by about a factor of two. This disparity is attributed to imperfections in the fabricated devices and uncertainty in material parameters.

Introduction:

Ferromagnetic materials are in widespread use as transducers and field sensors in hard disk drives. These materials in particular are useful because of their ease of magnetization, or equivalently, their high susceptibility. This susceptibility is related to the formation of magnetic domains, or areas where all the individual atomic dipoles are aligned. Magnetic moments in these domains tend to act together, allowing a much greater response to applied fields. These materials also often display an easy axis where, all other things being equal, the dipoles tend to lie along.

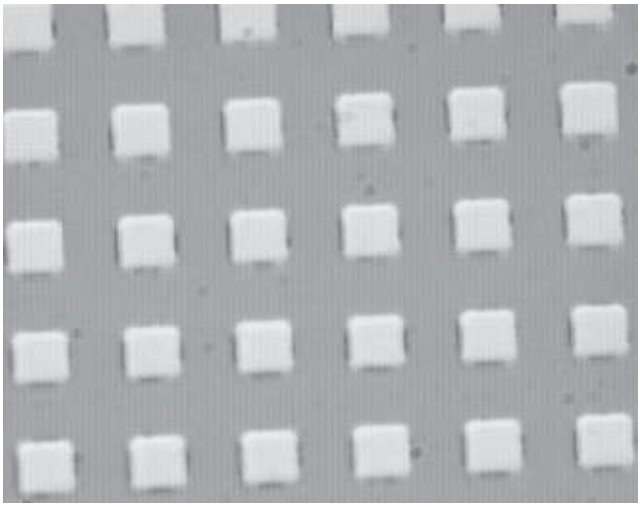

Figure 1: Optical image of array of 5μm squares of CoZrTaTb spaced 5 μm apart.

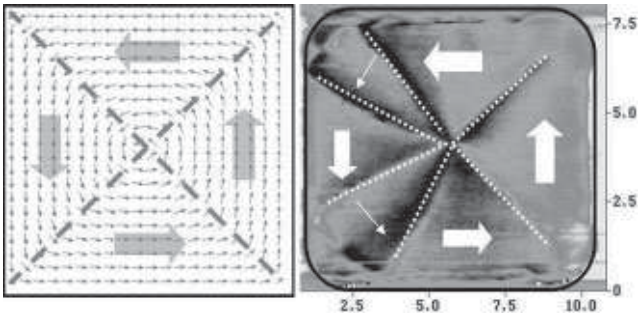

Figure 2: Ideal "four-domain" pattern for a square magnetic film and MFM image of actual film with "tulip" pattern.

By patterning magnetic materials, we can make higher resolution sensors because of the reduced area it measures. However, patterning the material tends to reduce the sensitivity to applied fields and alter the magnetic domain patterns. The relationship between susceptibility and domain patterns has not been fully understood; this work hopes to explain the connection.

Experimental Procedure & Device Modeling:

To investigate the susceptibility over a range of sizes, we patterned rectangles of varying dimensions using the material CoZrTaTb with a thickness of 400 nm. Using standard photolithography techniques and etching, we patterned areas of magnetic material with lengths and widths between 3-10 μm with the easy axis along one of these dimensions. To measure these devices, we fabricated large arrays of rectangles for a detectable signal. We arranged each type of rectangle into an array measuring 1 cm^2, containing thousands of individual devices. Figure 1 illustrates a small part of one array.

Following the fabrication of the devices, we tested their magnetic properties in a variety of ways. We first used a magnetic force microscope (MFM) to investigate the formation of domain patterns.

Next, we used a vibrating sample magnetometer (VSM) to get the magnetization versus applied magnetic field. This helped us to determine the susceptibility and the saturating field, which is the magnetic field needed to align all of the moments in the material along the axis of the field. Some preliminary measurements were also taken on a network analyzer to see the susceptibility over a range of frequencies. Additional imaging with scanning electron microscopy (SEM) was also completed.

In addition to making these patterned films, we engaged in modeling of these devices. Using simple arguments involving the geometry of the films and energies due to a variety of sources, we were able to make predictions about the domain patterns we would observe as well as the susceptibility and resonant frequency of these devices. Figure 1 shows an example of a calculated domain configuration called a "four-domain" pattern.

Results and Conclusions:

MFM imaging of the sample showed a domain pattern close to what was predicted through modeling. We expect a "four-domain" model shown in Figure 2; the adjacent MFM image shows that the sample is mostly in the expected configuration. Additionally, there is a "tulip" pattern in the top and bottom left corners of the sample. We believe that this is due to imperfections in the film and would not appear for a perfectly square piece.

Figure 3 shows the saturating field for square devices as a function of side length and direction of applied field. We see that there is a slight gap between the measured curves due to the direction of the applied field. If we are magnetizing along the easy axis, the sample will have a lower saturating fields than if we magnetized along the hard axis. When simulating

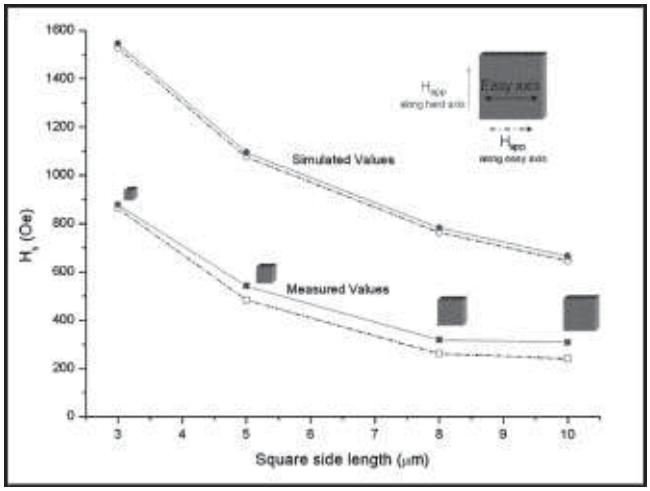

Figure 3: Graph of simulated and measured saturating fields for 400 nm thick squares of CoZrTaTb.

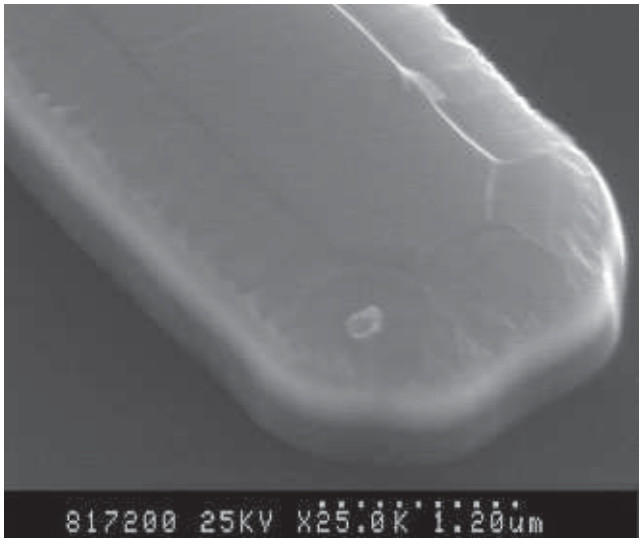

Figure 4: SEM image of rounded edges on an 8 μm by 3 μm "rectangular" pattern CoZrTaTb film. Sample still has sloped layer of photoresist on top.

these devices, we produce a curve of similar shape. However, the simulated fields are off by roughly a factor of two. We attribute this discrepancy to any number of factors, including rounding of corners in the devices, interactions between the devices, possible variation in thickness, the formation of "tulip" patterns due to defects in the devices, and uncertainty in material parameters. We see in Figure 4 that the rounding can be significant and may be enough to cause a noticeable drop in the susceptibility.

When measuring the samples in the network analyzer, we observed no resonant frequencies below 3 GHz, the frequency limit of the current equipment. This agrees with our calculated frequencies of resonance which are all greater than 3 GHz for the geometries of our devices. However, more testing is needed to determine the validity of the actual values of the resonant frequency.

Future research should investigate the multiple possible sources of model discrepancy and try to improve agreement between model and experiment. Additionally, resonant frequency measurements should be made using alternative methods to further test the model.

Acknowledgements:

Thanks to the National Science Foundation, Stanford University & Nanofabrication Facility, Principal Investigator Professor Shan X. Wang, my mentor Jason Jury, the entire Wang group, Professor Michael Deal, Jane Edwards, and all of the REU professors, staff, and students for making this possible.

Study of Stress Effects on Crystallization of Amorphous Silicon Pillars

Mahmooda Sultana, Chemical Engineering, University of Southern California

James Plummer, Michael Deal, Yaocheng Liu, Electrical Engineering, Stanford University

msultanausc@yahoo.com, plummer@ee.stanford.edu

Abstract:

Crystallization of amorphous silicon at low temperature is a technique that may be used to make 3-D integrated circuits and heterogeneous integration. One of the methods for low-temperature crystallization is to deposit a metal on the amorphous silicon and anneal. The metal works like a seeding material and allows silicon to crystallize at a lower temperature. However, the crystallization yield may vary depending on the amount of stress on the amorphous Si pillars.

In this project, we studied the nickel-induced crystallization process by varying the size of pillar transistors and the thickness of sidewall oxide, which varies the stress on silicon pillars. The results indicate that less stress yields more crystallization.

Introduction:

Today's world uses two-dimensional integrated circuits (ICs) where the devices are fabricated in a single layer. In three-dimensional ICs, devices are fabricated in more than one layer on the same substrate. The successful realization of 3-D ICs will significantly improve the chip performance [1].

Heterogeneous integration is also becoming more and more desirable for various applications. However, both 3-D ICs and heterogeneous integration require a single crystal of a semiconductor material on top of the dielectric film.

Figure 1: Silicon Pillar

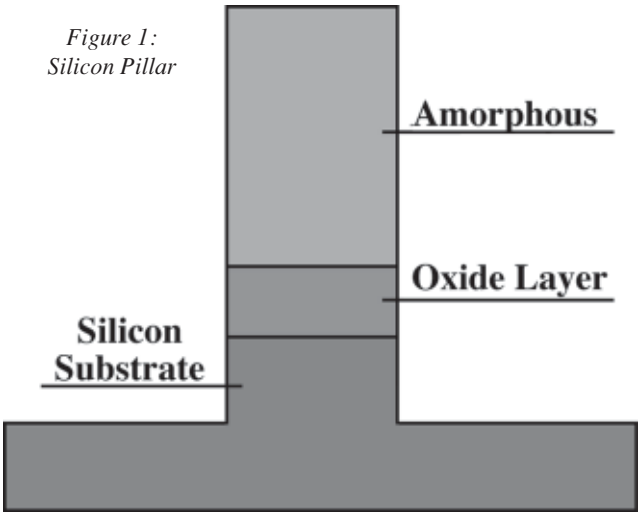

Since single crystals cannot be deposited on the top of the dielectric material, amorphous semiconductor material is deposited first and then crystallized.

The crystallization temperature needs to be below 500°C. Otherwise, the metal in the bottom layers will melt. It normally takes several hours at around 800°C to crystallization amorphous silicon. To reduce this temperature, metal-induced crystallization is used. In this process, a metal is added on top of amorphous silicon and annealed. The metal forms a silicide and passes along the amorphous silicon layer, while crystallizing it. Nickel has been used in our experiments because nickel reacts with silicon to form nickel disilicide, which has almost the same lattice constant as silicon and produces comparatively better quality of crystal [2].

Silicon pillars are surrounded by an oxide spacer to prevent any contact between nickel and silicon on the side. This prevents any crystallization from the side resulting in a single grain and with controlled orientation from the top. During annealing, the amorphous silicon expands and thus encounters compressive stress due to the sidewall-oxide. This stress increases as the thickness of the oxide increases and as the width of the pillars decreases. We studied how this stress affects crystallization yield.

Procedure:

Standard electron-beam-lithography is used to make 0.15, 0.18, 0.25 and 0.40 μm widths of amorphous pillars in each sample (Figure 1).

An oxide layer is deposited at 300°C to cover the pillar completely, and a vertical plasma etch is used to etch the oxide away from the top of the pillars. Next, nickel is sputtered on the top of the pillars. Then, the oxide sidewalls of three samples are etched with 50:1 HF for 20, 40 and 180 seconds. This step is performed to get different oxide thickness around the pillars of different samples, which produces different amount of stress on them. These three samples are annealed at 450°C for 15 hours.

After annealing, any trace of unreacted nickel from the top and the sides is etched away using aqua regia. The remaining oxide sidewall from each sample is

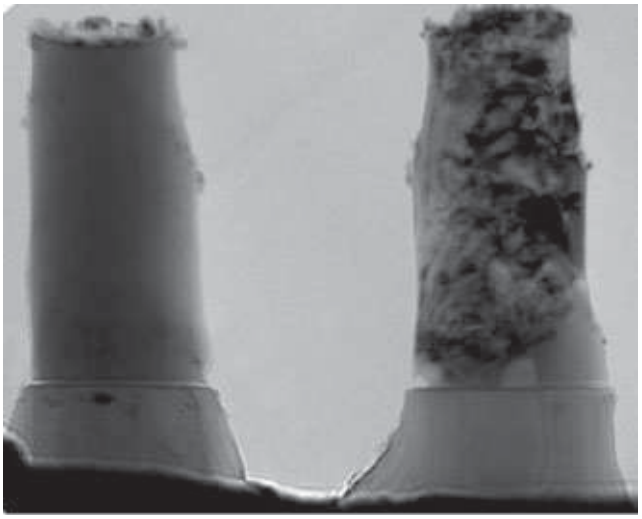

Figure 2: TEM image of pillars (the amorphous pillar is on the left and crystallized pillar is on the right).

then etched off. Finally, crystallization is analyzed with transmission electron microscopy (TEM).

In a similar procedure described above, three more sets of two samples are processed. The only difference is that oxide sidewalls of the two of each set are etched for 0 and 4 minutes before anneal and then different sets are annealed at the same temperature as before (450°C) but for a varied time: 10, 5 and 1 hour. The after-anneal steps are the same as before.

Results and Conclusions:

Due to time constraint and equipment problems, only the three samples with 15 hour anneal have been analyzed for crystallization with TEM (Figure 2).

The percentage of crystallization for each combination of pillars is calculated in Figure 3.

The graph shows that for small pillars, the percentage of crystallization increases as the oxide thickness decreases. This indicates that crystallization increases as the stress on the pillars decreases. However, as the pillar width increases, there is less effect on crystallization due to varied oxide thickness. In fact, for the largest size (0.4 μm), the oxide thickness seems to have little or no effect on crystallization. This is because, as the size increases, the pillars can better accommodate the stress from the oxide.

For the pillars with the thickest oxide, as the width increases, the percentage of crystallization also increases. That means, as the stress decreases, the percentage of crystallization increases, which is consistent with the result mentioned before for varied oxide thickness. Again, for the oxide-free or stress-free pillars, the size seems to play little or no effect on crystallization, which is similar to that mentioned earlier.

Summary:

In our experiments, the effect of stress on nickel-induced crystallization of silicon pillars is studied. Amorphous silicon pillars of different widths are fabricated and an oxide layer that produces stress on each pillar is deposited around them. The oxide layer is varied for different samples to produce different amount of stress on the pillars. It is observed that pillars with a thinner oxide layer have more crystallization than pillars with a thicker oxide. Also, the crystallization yield is greater for wider pillars that have lesser stress per volume unit than narrower pillars.

Therefore, it is found from our experiments that higher compressive stress causes less crystallization. This is important in understanding and optimizing the crystallization process used in fabricating 3-D ICs.

References:

[1] K. C. Saraswat, K. Banerjee, A. R. Joshi, P. Kalavade, P. Kapur and S. J. Souri, "3-D ICs: Motivation, Performance Analysis, and Technology," 197th Meeting of the Electrochem. Soc., Toronto, May 2000.

[2] S. Y. Yoon, S. J. Park, K. H. Kim and J. Jang, J. Appl. Phys. 87, January 2000, p. 609 - 611.

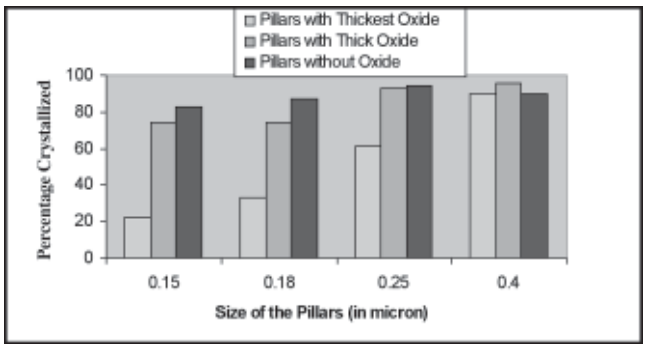

Figure 3: Percentage of crystallization for pillars with different combinations of pillar width and oxide thickness.

Design and Characterization of a AlGaAs Oxidation Furnace with Real-Time Monitoring Capability

Laura Zager, Engineering and Mathematics, Swarthmore College

James Harris, Evan Thrush, Electrical Engineering, Stanford University

lzager1@swarthmore.edu, harris@snow.stanford.edu

Abstract:

A crucial step in the fabrication of vertical cavity surface-emitting lasers (VCSELs) is the oxidation of an AlGaAs layer to serve as a current aperture for the laser beam. Existing oxidation furnaces require the use of test specimens to roughly calibrate the rate of oxidation, and provide poor control over the process.

In order to more carefully control the oxidation of the AlGaAs layer, a novel furnace has been designed and constructed with a glass viewport and imaging system to provide real-time optical monitoring of the VCSEL oxidation. It is anticipated that the system will achieve an oxidation resolution of 1 μm. This performance is much better than is currently achievable in standard oxidation furnaces.

Introduction:

Vertical cavity surface-emitting lasers (VCSELs) are a promising advance in semiconductor laser technology. VCSELs emit normal to the surface of the wafer, allowing for tighter packing density and the ability to test before cleaving.

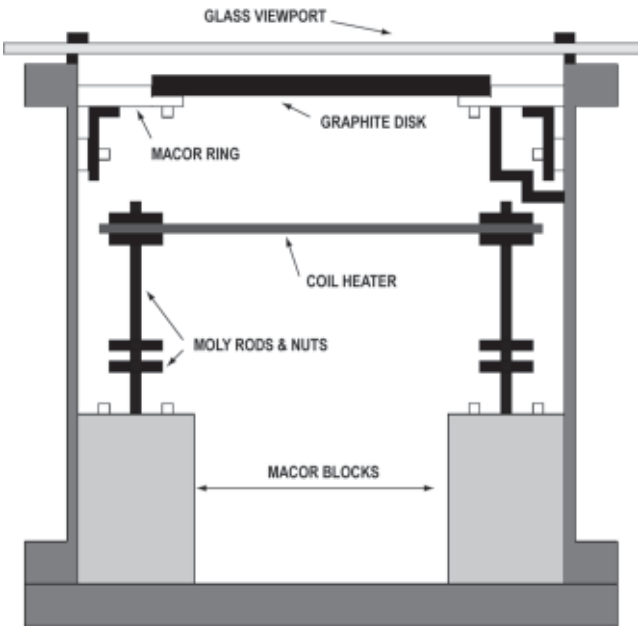

Figure 1. Furnace chamber.

A crucial step in the fabrication of VCSELs is the oxidation of an AlGaAs layer that serves as both a current aperture and an optical aperture for the beam. Each VCSEL on a wafer is mesa-etched, then heated in a 400°C environment of nitrogen saturated with water vapor to oxidize the AlGaAs layer from the outside in. The current in the VCSEL is confined to the unoxidized region at the center.

In order to fabricate a successful VCSEL, the size of the current aperture must be controlled within 1 μm. This precision is difficult to achieve with existing oxidation furnaces which require the use of test specimens to roughly calibrate the rate of oxidation and provide poor control over the process.

To improve the oxidation process, a novel furnace has been designed and constructed with a glass viewport and imaging system to provide real-time optical monitoring of the VCSEL oxidation.

This report will discuss the four subsystems of the furnace — the mechanical, gas delivery, electrical, and imaging systems — and present the results of an initial round of performance tests.

Mechanical System:

The mechanical system is the main body of the furnace, including the chamber, wafer shelf and viewport. A diagram of the system is given in Figure 1.

The furnace chamber is a stainless steel cylinder that is 5 $^1/_2$" in diameter. Two blocks of MACOR, a machinable ceramic, are mounted at the bottom of the cylinder. The MACOR blocks support two Mo rods, which are used to mount and serve as electrical contacts to the heater. The heater is a ceramic coil with a resistance of ~ 10 Ohms.

The wafer shelf consists of a ring of MACOR that serves as a thermal insulator which supports a graphite disk in a groove at the center of the ring - the wafers to be oxidized are placed in the center of the graphite.

The viewport consists of a sheet of Firelite ceramic glass that rests on a Viton o-ring. Additional o-rings and a copper ring rest on top of the glass and the entire apparatus is clamped to the lip of the chamber.

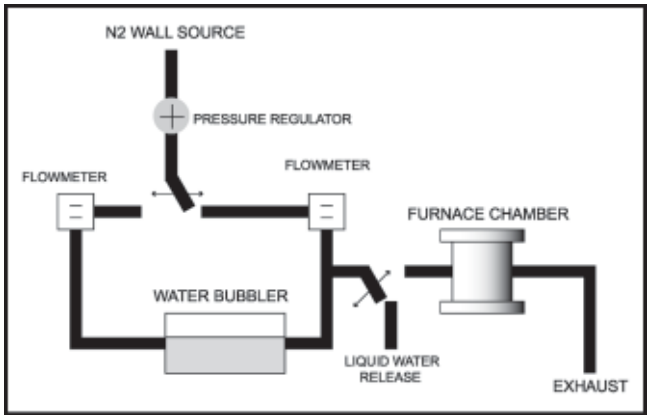

Figure 2. Gas delivery system.

Gas Delivery System:

A schematic of the vapor delivery system is given in Figure 2. Nitrogen from a wall source is passed through a regulator at approximately 1 scfh, then through to a bubbler or straight to the chamber. At the bubbler, the nitrogen is sent through a heated water bath, transporting vapor to the chamber. A slight vacuum in the chamber prevents condensation from forming on the viewport. The gas delivery system also includes heating tape to maintain the temperature of the vapor as it travels to the chamber, an extra valve to clear the line of liquid water, and a trap at the outlet to separate the liquid from the gas.

Electrical System:

The electrical system consists of the power supply to the furnace and the temperature controller — a schematic is given in Figure 3. An Omega process controller reads the temperature within the furnace chamber by monitoring a thermocouple mounted on the graphite disk, compares it to a pre-set temperature, then opens or closes a solid-state relay that turns power to the heater coil off or on.

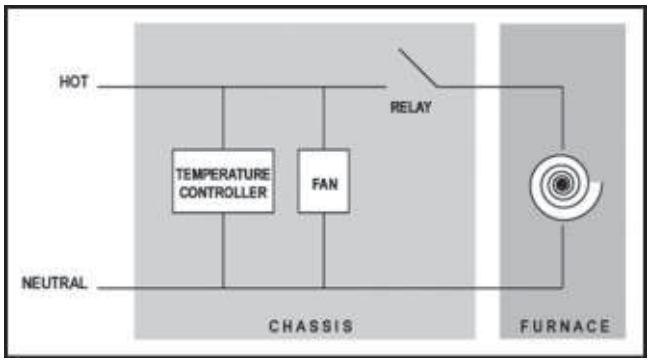

Figure 3. Electrical system.

Imaging System:

Researchers have reported that a maximum difference in reflectivity between oxidized and unoxidized regions is achieved at infrared wavelengths. The sample in the furnace chamber is illuminated by a white light source—the reflected light passes through a 20x objective, a filter that removes the below-IR components ($\lambda \leq 695$ nm), a second stage of magnification and into a CCD camera. The camera sends an analog output to a television screen. We are able to image features as small as 3 μm with this system, and use vibration isolation to further improve the resolution.

Results:

Preliminary qualitative results indicate that oxidation was achieved running the furnace at 400°C for ten minutes. Running the system at 425°C caused delamination of the mesa oxidation layer, presenting an upper limit for the operating temperature. At this point, monitoring the oxidation as it occurs presents the most significant challenge. The CCD camera is less sensitive to IR light than shorter wavelength light, so the images are not crisp and the oxidation front is hard to distinguish. Unfortunately, one of the calibration tests damaged the heater coil beyond immediate repair—testing will continue once a new heater is received. We hope to fully characterize the system's oxidation performance as well as improve the resolution and quality of the imaging system.

Acknowledgments:

I'd like to thank our mentor, Evan Thrush, for his excellent preparation and ideas. Dave Reed of Oepic provided us with valuable advice. Mark Wistey, Xian Liu and the rest of the Harris group were helpful. Thanks also to the Stanford Nanofabrication Facility, Prof. James Harris of the Electrical Engineering Department, and the National Science Foundation.

Nanotech at UCSB

University of California, Santa Barbara, Santa Barbara, CA
http://www.nanotech.ucsb.edu/default.html

2002 UCSB REU Interns

NNUN REU Intern	School Affiliation	Principal Investigator
From Left to Right:		
Ms. Celia See-Ah Chan	Cornell University	Samir Mitragotri
Ms. Kelly McGroddy	University of Pennsylvania	Pierre Petroff
Ms. Krista Ehrenclou	UCSB Nanotech	REU Mentor
Mr. Michael Adler	SUNY Stony Brook	Vojislav Srdanov
Ms. Janelle Crane	UC Santa Cruz	Helen Hansma
Mr. Thomas Graziano	Cornell University	David Awschalom
Ms. Jennifer Park	University of Colorado Boulder	Jacob Israelachvili
Mr. Hani Aldhafari	Contra Costa College	Jim Speck
Ms. Kristen Van Horn	Harvey Mudd College	Jim Speck

Electron Paramagnetic Resonance of Photochromic Sodalite

Michael Adler, Physics, Stony Brook University

Vojislav Srdanov, IQUEST, University of California at Santa Barbara

mantis_bog@yahoo.com, srdanov@chem.ucsb.edu

Introduction:

Sodalite is a nanoporous mineral whose molecules consist of a cage-like structure of alternating AlO_4 and SiO_4 tetrahedra that form the cage. The aluminum and silicon atoms reside at the vertices of the cage [1]. Of the many varieties of sodalite that exist, this paper deals with dry-salt free sodium sodalite. This simply means that the inside of the cage contains no salt and has three sodium atoms within. (See Figure 1.)

In zeolites, which are structurally similar to sodalite, it is possible to create ionic centers with the use of butyl-lithium, a known electron donor [2]. This is believed to occur because the butyl-lithium enters the large zeolite cages, where it is broken down by the huge electric fields present within.

When attempting this procedure with Sodalite nothing happens. This is probably because the sodalite cage is too small to admit the butyl-lithium. After the sample had been exposed to light for a long period of time though, it was noticed that it had taken on a bluish hue, an indication that Na_4^{+3} centers had formed in the sodalite [3]. Obviously this reaction can go forward in sodalite, but light is needed for it to occur.

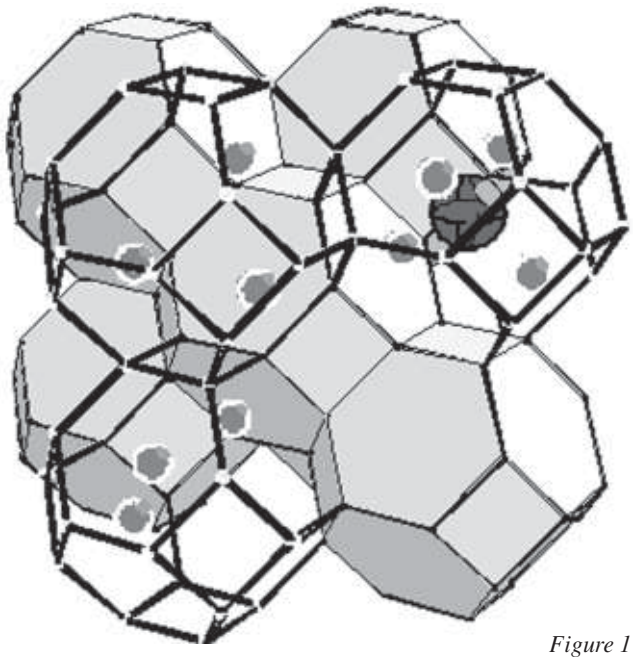

Figure 1

These Na_4^{+3} centers behave just like F-centers which are simply an unpaired electron occupying an empty space (point defect) in an ionic lattice.

Experimental Procedure:

To analyze this reaction, a Bruker Electron Spin Resonance (ESR) Spectrometer is used to detect the extra electron present in the cage due to the formation of the center.

ESR spectrometry is a technique used to analyze materials that contain an electron with unpaired spin. A magnetic field is applied to the material, and microwave absorbance is recorded. When $h\nu=g\mu B_0$, resonance occurs and a maximum in microwave absorption is detected. To get reliable readings from the spectrometer, potassium electrosodalite is used as an internal standard. Due to its low g value of 1.9985 (most materials have a g value slightly greater than 2), its signal is shifted to higher fields with respect to other materials. This internal standard is needed because the ESR absorption is going to differ slightly from reading to reading due to differences in the tuning of the microwave radiation. Therefore an unknown signal can be compared to that of the known signal from the KES.

20 mg of KES was placed in an EPR tube, along with sodalite and butyl lithium and sealed under vacuum in a glove box. The KES was diluted with potassium bromide, which gives no EPR signal, to the point when a comparable signal with that of the Sodium butyl lithium mixture was obtained. This sample was then subjected alternately for two minutes to 20 mW of 488 nm and 514 nm laser light from an argon-ion laser, and the ESR signals taken after each exposure.

Results and Discussion:

Figure 2 shows a stacked data plot of the EPR spectrum taken after each thirty-minute exposure to the laser light. The increasing signal clearly shows the formation of these centers. Figure 3 shows intensity vs. time data plot for the EPR signals.

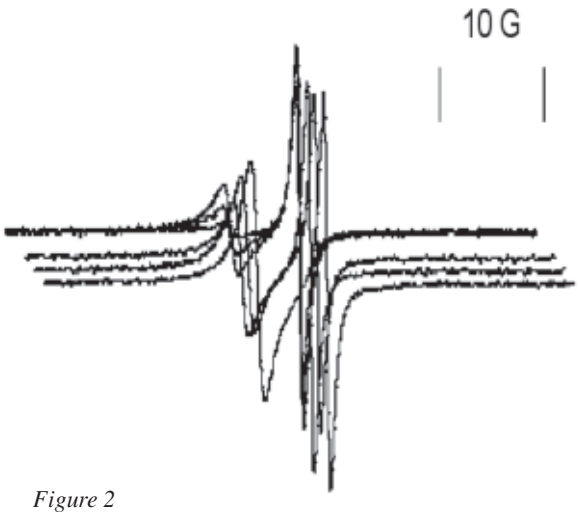

Figure 2

The intervals of no slope occur after exposure to the 514 nm green laser light, while the intervals with apparent slope occur after the sample was exposed to the 488 nm blue laser light.

Apparently, this reaction needs light to occur. In particular blue light of 488 nm is instrumental, as the longer wavelengths did not promote the formation of these centers. We believe that this reaction occurs because the blue light disassociates the butyl lithium into Li^+ and a butyl anion. The anion then donates an electron to a surface sodium ion, which enters the cage soon after to form the Na_4^{3+} center.

Further low temperature EPR readings are needed to identify the butyl half of the butyl free radical. We will also look for octane using mass spectrometry.

Acknowledgements:

This research was funded by the National Science Foundation and the Petroleum Research fund.

I would like to thank Vojislav Srdanov and Ljiljana Damjanovic for their invaluable insight and assistance in the laboratory, as well as the NNUN: especially Liu Yen Kramer and Al Flinck.

References:

[1] Srdanov, V; MOnnier, A; Stucky, G; Metiu, H, J Chem Phys. 1994, 6944-6952.

[2] Yoon, K.B.; Kochi, J.K. J Chem Soc Comm. 1988, 510-511.

[3] Mayer, J.; Srdanov, V.I., unpublished work.

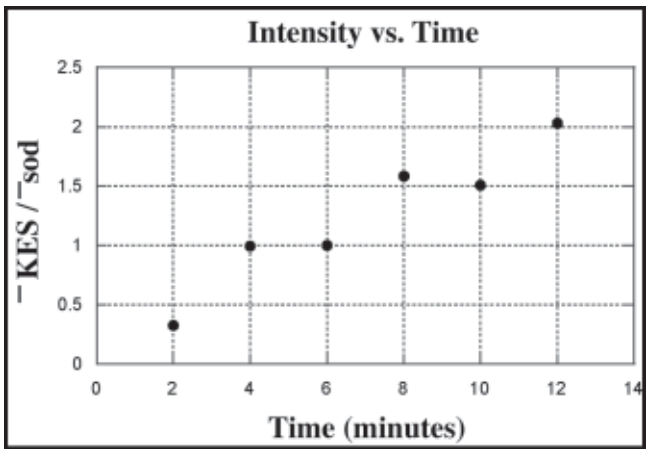

Figure 3

Characterization of MBE Grown Field Effect Transistor Structures Grown on SiC Substrate with AFM & Hall Mobility

Hani Aldhafari, EECS, UC Berkeley

Dr. James Speck, Mel McLaurin, Materials Science Dept., UCSB

haldhafari@yahoo.com, speck@mrl.ucsb.edu

Abstract:

The research group builds Field Effect Transistor (FET) structures by growing layers of AlGaN on (0001) GaN, which are both grown on a (6H) SiC substrate. The growth process is done using plasma assisted Molecular Beam Epitaxy (MBE). The charge carrier mobility in the grown heterostructure FETs is subject to halting mechanisms, namely: dislocations, impurities, and interface roughness. The goal of the group is to drop the interference of these mechanisms and to obtain the highest mobility possible for the 2D electron gas.

To achieve our goals, the grown FET structures are subjected to three tests to monitor the progress of our samples: X-ray, AFM, and the Hall Mobility Test. The group modified the growth process in several ways and monitored the progress of the samples and tried to find the growth conditions that work to further smoothen the surface and increase the mobility of our charges.

Introduction:

Group III Nitrides in general are known to have a great potential in the making of high power Field Effect Transistors (FETs). The research group grew FETs that were, in principal, different in two ways from the conventional FETs grown by industry labs today. The FET structures were made with GaN instead of GaAs and were grown with Molecular Beam Epitaxy (MBE) instead of the conventional Metal Organic Chemical Vapor Deposition (MOCVD).

Two major reasons compel us to look for other alternatives to GaAs. Arsenic is poisonous and thus dangerous to the environment and we try to replace it with Nitrogen which is much more environment friendly. In addition, GaN has more promising features than GaAs when it comes to the making of high power FET structures.

One more difference we added to our research is the fact that we try to use MBE to grow our FETs instead of using the conventional MOCVD technique used in industry today. MBE is known to have an incredibly slower growth rate than MOCVD but the deposition on the surface is much easily controlled.

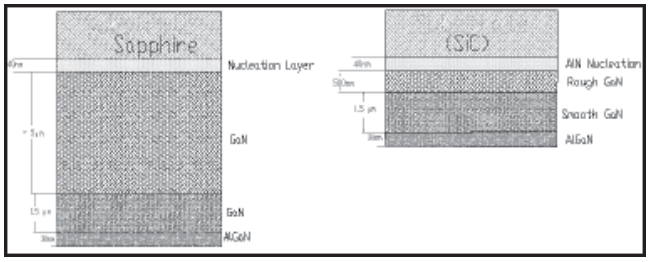

Figure 1: MOCVD grown (left) vs. MBE grown (right).

Several reasons compel us to change our growth method: 1st, a phenomenon called parallel conduction is more severe when using the MOCVD growth technique; 2nd, growing using MOCVD requires an extra amount of GaN as shown in Figure 1.

Procedure:

Simply, the group grew numerous samples of AlGaN/GaN FETs and characterized the samples in the following order: X-ray diffraction, AFM, and finally Hall Mobility measurements. A SiC substrate is etched using HCl to remove junk from the surface and to get rid of the oxidation layer that formed during the exposure of the substrate to air. Then the sample is placed inside the MBE chamber and the temperature is cranked up to around 800°C to remove any remaining junk on the surface. Then the growth process begins by growing a 40 nm AlN nucleation layer.

Next, two layers of GaN are laid on top with different smoothness' and finally the sandwich is completed with a material with a wider bandgap than GaN, AlGaN. Variation in the amount of the rough GaN layer and its roughness is the procedure used by the group to change the surface morphology of our FET structures.

Results:

During the past two months, the group was successful in improving FET structures in several ways. The group figured effective ways to decrease the number of dislocations, which included roughening the rough GaN and increasing its amount it by a certain

percentage. Thus, we were able to heavily decrease the number of pits and were finally able to get decent readings for the mobility of our FETs.

Although pits were replaced by Ga droplets (which we want to minimize to consume only 1% of the surface) and the mobility was still not even comparable to the GaAs FETs', getting any mobility off such a heavily rough surface was a great success in itself.

As shown in Figure 2, the pits extend through the AlGaN/Gan interface and thus scatter the 2D electrons and would hamper a large percentage of the mobile 2D electron-gas that forms at the interface of the AlGaN/GaN layers. The group was able to accomplish 55% of the task in six weeks while the funders of our project gave us six months to achieve a mobility of 1400 cm/volt * sec.

In general, the group is very close to achieving its goal and future research is currently being prepared to further improve the quality of our FET structures.

Conclusion:

There are several conclusions that the group was able to draw from our first six weeks of experimentation with GaN grown with MBE. Perhaps the most important conclusion we were able to draw out of this experiment was that the growth diagram of GaN (Figure 3) no longer predicts the growth of AlGaN.

In addition, we were able to figure that the concentration of Al in our AlGaN is partly responsible for the pitting on the surface, which was not predicted by the growth diagram. These conclusions lead us to consider two approaches for the future research:

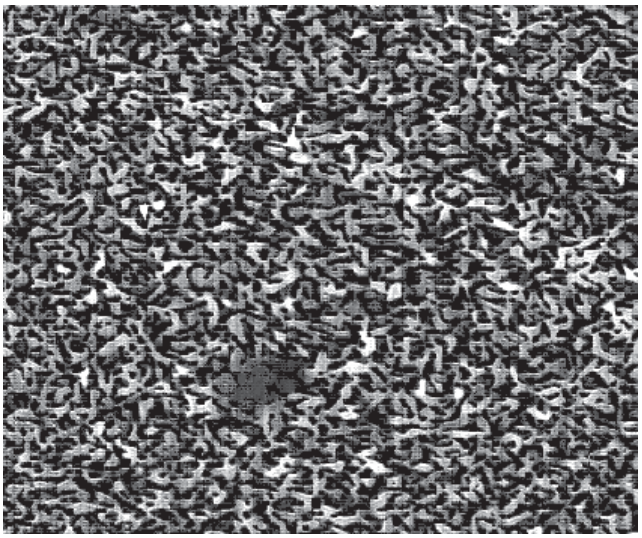

Figure 2: An early sample of GaN (AlGaN layer).

1st, the group considers growing FETs and varying the amounts of Al and monitoring the progress of the surface as the concentration of Al varies. In addition, the group also considers composing a new growth diagram that can guide us in the future to grow better FETs.

Acknowledgements:

Thanks to my advisor Mel McLaurin for his patience. In addition, great thanks to Liu Kramer, Al Flinck, and Krista Ehrenclou from the UCSB program and Melanie-Claire Mallison at Cornell for their hard work during the summer to ensure us a pleasant summer.

References:

[1] Kittel, Charles. Introduction to Solid State Physics. Seventh Edition. New York: John Wiley and Sons, Inc., 1996.

[2] Pierret, Robert F. Semiconductor Device Fundamentals: with Computer-Based. USA: Addison-Wesley Publishing Company, Inc., 1996

[3] O. Brandt, R. Muralidharan, K.-J. Friedland, K. H. Ploog. "(Al,Ga)N/GaN field-effect transistor structures grown on 4H-SiC(0001) by plasma-assisted molecular beam Epitaxy" August, 2 2002. <http://www.pdi-berlin.de/jabe99/part2/4041.pdf>.

[4] X. Z. Dang, P. M. Asbeck, and E. T. Yua. "Measurement of drift mobility in AlGaN/GaN heterostructure field-effect transistor." 25 April 1999. August 10, 2002. <http://kesey.ucsd.edu/group/pdfpubs/apl_jun99.pdf.>.

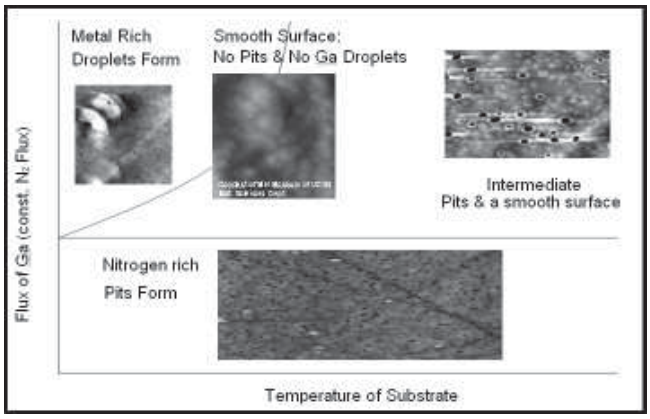

Figure 3: Growth diagram of GaN.

Investigation of Small Diameter Jet Injection

Celia Chan, Biological Engineering, Cornell University

Samir Mitragotri, Joy Schramm, Chemical Engineering, UCSB

cc266@cornell.edu, samir@engineering.ucsb.edu

Abstract:

Pressure-driven jets have been used for intradermal delivery of a variety of drugs. In spite of their introduction into clinical medicine, variability and occasional bruising have limited their widespread acceptance. Traditional jet injectors typically produce a 152 μm diameter jet that travels at 150 m/s. Previous research on microneedles has shown that penetration of microneedles to about 20 μm into the dermis is painless to the patient [1].

We report on the proposed use of a micro-scale diameter jet to deliver drugs intradermally that may achieve similar painless penetration. Our experiments involve the use of 30 μm diameter nozzles. To assess the penetration of the jets, injections have been made into polyacrylamide gels and human skin. To quantify the amount of delivery by the 30 μm jet, radiolabeled mannitol has been injected into human skin. The fluid penetrates into the dermis 0.9 mm with the 30 μm diameter jet as opposed to 6 mm, the entire thickness of the dermis, with a 152 μm diameter jet.

With the introduction of a small diameter jet, we hope to devise a jet injector incorporating an array of microjets that will eliminate the discomfort in a conventional jet injection.

Materials and Methods:

The model jet injector used for our experiment was Vitajet 3 from Bioject Inc. To create a smaller diameter jet, sapphire orifices of 30 μm in diameter were placed at the inside of the nozzle. A dynamic pressure transducer (Dynasen Inc., Goleta) was inserted into the nozzle to measure the pressure during the injection. A high-speed camera image (Kodak Ektapro 4500, 18000 fps) of the microjet was captured to verify the formation of the microjet.

Figure 1: Cross-section of human skin after a 30 μm diameter microjet injection with Sulforhodamine B dye.

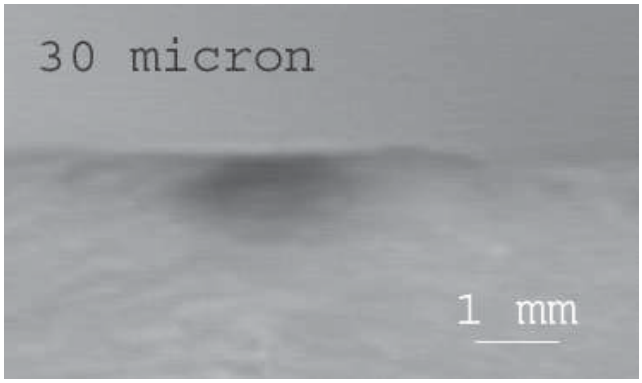

Figure 2: Processed image of 30 μm diameter microjet dye injection using Adobe Photoshop. Lines of constant intensity of Sulforhodamine B dye imaged to measure the penetration and dispersion of microjet.

Polyacrylamide gel was used as a preliminary model for measuring the penetration of the jet. The clear gel allows us to observe and measure the penetration of a microjet easily. A greater percentage of acrylamide results in an increase in Young's modulus of the gel. The Young's modulus of 40% acrylamide gel most resembles the Young's modulus of human skin (~1 MPa).

Thirty μm diameter microjets were ejected toward polyacrylamide gels with acrylamide percentages (mass/volume) from 8% to 40% acrylamide for measuring the penetration of the jet and to help predict the delivery into human skin.

Sulforhodamine B dye (0.069 mL) was injected into human skin in order to observe the penetration and dispersion of the microjet. A digital image of the cross-sectioned skin was captured immediately after the injection. The penetration and dispersion was analyzed by measuring areas of high constant intensity using Adobe Photoshop.

To measure the amount of delivery into skin by the microjet, radiolabeled mannitol (0.098 mL) was ejected toward human skin. After injection the top of the skin was wiped with distilled water to reduce false readings from radiolabeled mannitol remaining on top of the skin. Then the skin was dissolved with a skin solubalizer (Solvable, Packard Inc.) and liquid scintillation analysis was performed. The amount of mannitol detected in skin after injection indicated the amount of delivery.

Results and Conclusions:

From our experiments we conclude that a 30 µm microjet can penetrate into human skin. Figures 1 and 2 are one cross-section of human skin from a Sulforhodamine B dye injection with a 30 µm diameter microjet. When processed with Adobe Photoshop (Figure 2), we determined that the total penetration and dispersion depth of a 30 µm microjet is 0.9 mm in depth in human skin. This is considerably less than a traditional 152 µm jet with a total penetration of 6 mm (Figure 3).

Since the 30 µm jet penetrates less into the dermis, it has less chance of causing pain to the patient. The results from radioactive mannitol injections indicate the amount of delivery with the 30 µm jet is 0.0074 ml (0.96 vol%) in one injection at an average velocity of 130 m/s. With this amount of delivery an array of 27 microjets may be sufficient to delivery a significant insulin dosage (0.02 ml).

Acknowledgments:

Joy Schramm, Samir Mitragotri, NNUN

References:

[1] S Kaushik, A Hord, D Denson, D McAllister, S Smitra, M Allen, and M. Prausnitz, "Lack of Pain Associated with MicrofabricatedMicroneedles" Anesth Analg 2001; 92: 502-4.

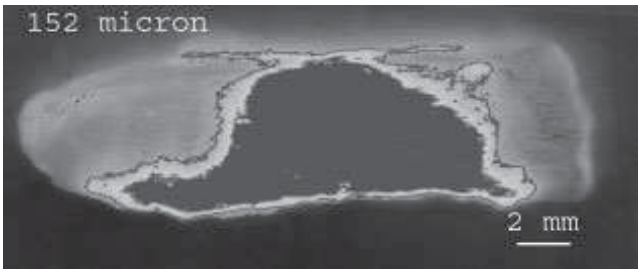

Figure 3: Processed image of 152 µm diameter jet injection with Sulforhodamine B dye using Adobe Photoshop.

Atomic Force Microscopy and Force Spectroscopy on Wheat Glutenins

Janelle Crane, Biochemistry and Molecular Biology, UC Santa Cruz

Prof. Helen Hansma, Dr. Emin Oroudjev, Physics, University of California, Santa Barbara

jmcrane@cats.ucsc.edu, hhansma@physics.ucsb.edu

Abstract:

High molecular weight (HMW) glutenin is thought to be one of the key protein groups that create high viscoelasticity in wheat gluten. If the predicted structure of HMW glutenin can be verified, synthetic analogs can then be produced for use in food and non-food applications. Also, this research may provide insight on the relationship between glutenin's structure and its mechanical properties for use in altering those properties.

In this experiment, HMW glutenin was isolated from crude gluten and imaged with the Atomic Force Microscope (AFM) to verify the state and the amount of sample on a surface. The Molecular Force Probe (MFP) was used to obtain force curves by pulling on single glutenin molecules and their matrixes.

The preliminary analysis indicates that the HMW glutenin force curves do not match the typical curves found when pulling on proteins consisting only of polypeptide backbone chains.

Introduction:

Gluten consists of two groups of proteins known as gliadins and glutenins, of which the latter includes the longer high-molecular weight (HMW) glutenins and the shorter low-molecular weight (LMW) glutenins.

Some researchers argue that the viscoelastic properties of gluten are mainly due to the disulfide bridges created between the HMW glutenins' end domains and the matrixes formed with other gluten proteins. Others argue that the unique β-spiral structure (Figure 1) in the central domain of glutenin is also a contributor.

The hypothetical β-spiral structure contains frequent and relatively uniformly spaced β-turns held together by hydrogen bonds. The arrangement and abundance of a significant number of "sacrificial" hydrogen bonds might contribute to the elasticity of glutenins.

This research may provide substantial evidence on the accuracy of the β-spiral model and the possible contribution of the β-spiral structure to gluten's viscoelasticity.

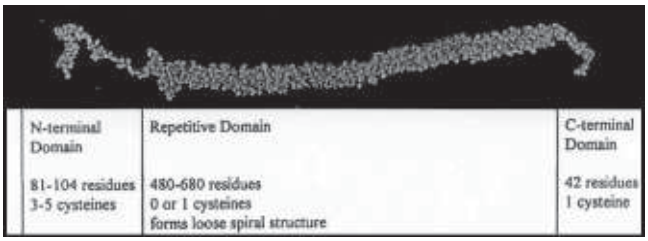

Figure 1. Predicted structure of HMW glutenin. (Shewry [3])

Presently, this paper details the preliminary data collected from the first isolation procedure, AFM images, and forces curves taken from MFP.

Procedure:

The HMW glutenin semi-purification and isolation procedure was adapted from a procedure used by Van Dijk [3]. Crude gluten was extracted with buffers and alcohols to remove starches, fatty acids, and gliadins. The resulting pellets were pressure dried, but this process rendered the pellets too hard to resuspend. Using sonification, small fragments of the pellet were obtained and continued through the protocol. However, a second procedure was also conducted following the same steps, but excluding the pressure-drying and sonification steps.

Next, the pellets were resuspended and precipitated several times in a solution containing a reducing agent that breaks disulfide bonds in order to create a stock solution with single-molecule glutenins.

Results and Conclusions:

AFM images were taken of the first procedure sample using stock, 1/10, 1/100, and 1/1000 dilutions. The AFM image (Figure 2) shows distinctive elevated regions of the sample, which may be individual or groups of HMW glutenins. Due to possible sonification protein structure damage, more AFM images should be taken from a second procedure sample to more accurately analyze the results of the isolation.

The MFP is similar to the AFM, except that instead of scanning a sample, the nanoscale probe is used to

measure the amount of force required to pull on and break different domains of proteins (evident as force peaks in Figure 3). Only five of 200 pulls could be easily analyzed from the second procedure due to variation between pulls.

A single molecule interaction (which is optimal for analysis) is usually seen at the end of a pull as a smooth and clean force curve and peak, absent of other protein breakage peaks (Figure 3). A computer fits a curve to the graph using a worm-like chain model with four different parameters: contour length (length of protein backbone), persistence length (flexibility of protein backbone), zero deflection, and surface position.

If the protein has no strong secondary structure, then persistence length should be fixed between 0.4-0.8 nm (values found experimentally by pulling on various proteins). Zero force (zero deflection) and surface position can be found from the experimental force curves and fixed for the analysis. Thus, the worm-like chain model can be fit into the experimental force curves by fixing persistence length, zero force and surface position and letting contour length vary.

The force curves analyzed in this experiment were more shallow in comparison to the worm-like chain fit curve indicating that there are probably extra structures (such as the β-spiral structure) which are breaking (Figure 3).

However, more research is needed not only to verify the purity of isolated HMW glutenins, but also, to obtain enough pulls to statistically validate a claim that HMW glutenin force curves are different from the worm-like chain model. If a consistent difference can be found and analyzed, the results could be used to validate and elaborate our knowledge on the secondary structure of HMW glutenin as well as improve our understanding of the relationship between protein structural organization and its mechanical properties.

Acknowledgments:

Emin Oroudjev, Helen Hansma, NNUN, NSF.

References:

[1] Maningat, C.C., DeMeritt Jr., G.K., Chinnaswamy, R., and Bassi, S.D. Properties and applications of texturized wheat gluten. Cereal Foods World. 44:650, 1999.

[2] Lens, J.P., Mulder, W. J., and Kolster, P. Modification of wheat gluten.

[3] Shewry, P.R., Tatham, A.S., and Lazzeri, P. Biotechnology of Wheat Quality. J Sci Food Agriculture. 73:397, 1997.

[4] Van Dijk, A.A., De Boef, E., Bekkers, A., Van Wijk, L.L., Van Swienten, E., Hamer, R.J., and Robillard, G.T. Structure characterization of the central repetitive domain of high molecular weight gluten proteins. Protein Science. 6:649, 1997.

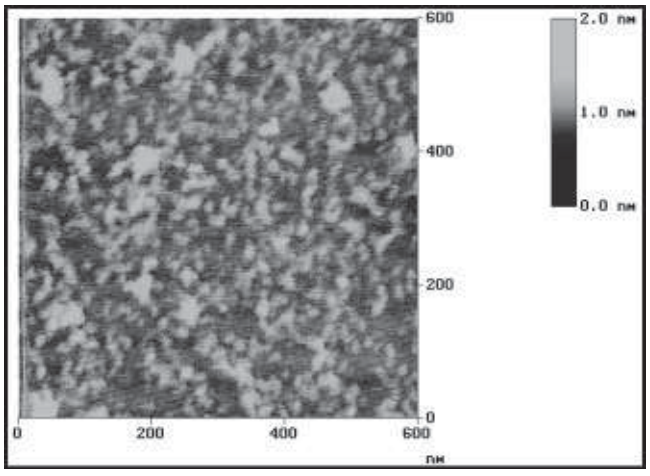

Figure 2. AFM image of 1/1000 diluted first procedure glutenin sample.

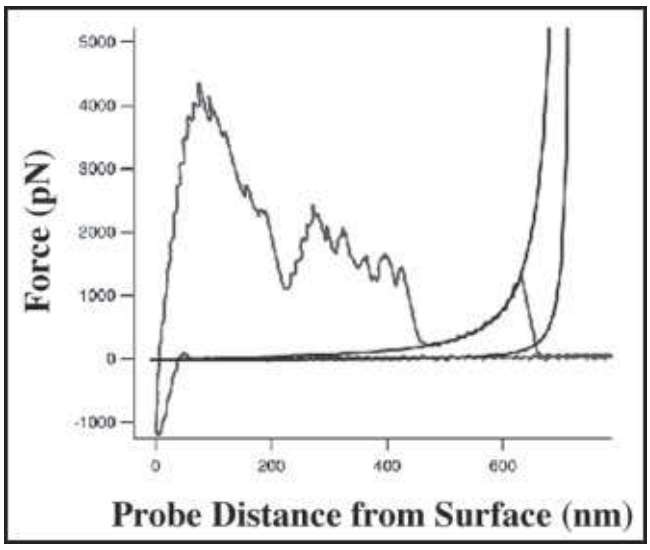

Figure 3. MFP force curve obtained from pulling on an undiluted sample of HMW glutenin. The curve on the left is the experimental fit; the curve on the right is the worm-like chain model fit.

Electron Spin Coherence in Silicon

Thomas Graziano, ECE, Cornell University

Dr. David Awschalom, Vanessa Sih, Physics, UCSB

tmg23@cornell.edu, awsch@lotemp.physics.ucsb.edu

Introduction:

Precession is the periodic circular motion of a rotating body's axis due to an external torque. In a common demonstration, a spinning flywheel is fixed along one side of its axis of rotation. Gravity applies a torque to the spinning wheel, causing the wheel to rotate about the fixed end of its axle (Figure 1b).

Electrons, negatively charged subatomic particles, possess a quantum mechanical property known as spin; the two spin states are known simply as "up" and "down". We can think of the electrons semi-classically as charged spheres spinning either counterclockwise or clockwise. Using the right hand rule convention, we denote the direction of an electron's rotation with a spin vector S bar (Figure 1a).

A magnetic field causes the electron spins to precess like gravity causes the flywheel to precess (due to the Zeeman energy splitting of spin-up and spin-down states along the direction of that magnetic field). The spin vector rotates in the plane perpendicular to the direction of the magnetic field; the precession frequency is directly proportional to the applied magnetic field and dependent upon the material (Figure 2).

If we just subject a sample to a magnetic field, the electron spins precess incoherently. In other words, each electron's spin vector is pointing in a random direction; there's no long-range order to the precession (Figure 3a). The net spin magnetization is zero since the sum of the electron spin vectors is zero.

Figure 1.

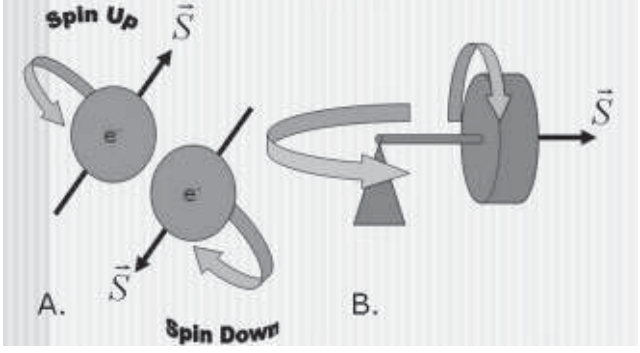

Experimental Procedure:

Ideally, we want all of our electrons to precess coherently with aligned electron spin vectors (Figure 3b); if we have groups of electrons precessing coherently, then we can effectively probe the system without disturbing the net coherence.

We can spin-polarize the conduction band electrons (get them all to point in the same direction) with a finely tuned circularly-polarized light beam. After we shine this light on our sample, the bulk of the spin vectors in our sample's conduction band electrons point in the same direction. But when we turn off our pumping light beam, the electron spin polarization eventually decays due to spin scattering and other effects. In other words, the electron spins eventually stop "pointing" in the same direction after a period of time. If we simultaneously apply a magnetic field with the tuned circularly-polarized light beam, the electron spin precession is coherent (Figure 3b).

We can probe electron spin precession in Gallium Arsenide (GaAs) samples using a technique called time resolved Faraday rotation (TRFR). Shining a linearly polarized probe pulse onto the sample will rotate its polarization by an angle proportional to the direction that the majority of spin vectors are pointing, i.e. the net magnetization of the system (Figure 4). The experiment results in a decaying sinusoid of the polarization angle versus time. Each oscillation of the sine wave represents one precession rotation of the spin vectors; the decay of the sine wave represents the rate of decoherence (how quickly the spin vectors stop pointing in the same direction).

Figure 2.

$$\omega = \frac{g\mu_B \vec{B}}{\hbar} = \frac{\Delta E}{\hbar}$$

ω- precession angular frequency

g- "g" factor

μ_B-Bohr magneton

ħ-Plank's Constant/2π

ΔE- Zeeman energy gap

Results and Discussion:

Unfortunately, we have problems measuring this coherence when we use silicon samples. Direct bandgap materials—such as GaAs—release energy as radiation in electron recombination; the wavelength of this light is determined by the energy gap traversed by the electron.

However in indirect bandgap materials—such as Si, Ge, and GaP—recombination requires the emission of both photons (light) and phonons (mechanical waves in the crystal). Thus, optical transitions are more complicated in indirect bandgap semiconductors than direct semiconductors; so the effectiveness of time-resolved Faraday techniques for probing silicon is questionable.

But experiments involving the hyperfine interaction between electrons and nuclei have shown that electrons do indeed precess in silicon. In fact, the coherence time in silicon is much larger than that in GaAs (hours compared to nanoseconds). It's just a matter of effectively probing the silicon.

We fabricated several silicon Hall bars to perform low temperatures carrier concentration measurements. Coherence times are very dependent upon doping levels in GaAs, so this type of measurement is commonly performed before electron spin precession experiments. By doping the samples n-type, there will always be electrons in the conduction band; so even after recombination, electrons will still be precessing in the conduction band. After three fabrication runs, none of the Hall bar samples worked in the cryostat; at lower temperatures the bar resistances became too high.

Rather than preparing a fourth batch of Hall bars, my mentor and I decided to move on. For the past few weeks, we have been setting up optics to probe porous silicon samples from the Koch group in Germany. Due to a higher degree of electron spatial confinement in porous silicon, the uncertainty principle tells us that the k-space curves for silicon (or energy vs. momentum space curves) must broaden. Therefore, porous silicon behaves more like a direct bandgap material; transitions without phonon emission are allowed in porous silicon. So there is hope that these samples can be probed effectively.

We hope that electron spin coherence in silicon could eventually be utilized in the construction of an affordable quantum-computing device.

Acknowledgements:

National Nanofabrication User's Network (NNUN), National Science Foundation (NSF), University of California Santa Barbara, Defense Advanced Research Projects Agency (DARPA), Vanessa Sih & The Awschalom Group, Melanie-Claire Mallison, Liu-Yen Kramer, Al Flinck, Krista Ehrenclou, Richard Shealy, and my fellow interns.

References:

[1] Awschalom, D. D., and J.M. Kikkawa. "Electron Spin and Optical Coherence in Semiconductors," Physics Today, Volume 52, No. 6, p. 33 (1999).

[2] USCB Research Site. May 2002. http://www.iquest.ucsb.edu/sites/Awsch/index.html

[3] Young, Hugh D., and Roger A. Freedman. University Physics, 9th Edition. Addison-Wesley Publishing Company, Inc. (c)1996. p. 314-317, 890-892.

[4] Koch, F. et al. "Polarization phenomena in the optical properties of porous silicon," Journal of Luminescence 70 (1996).

Figure 3.

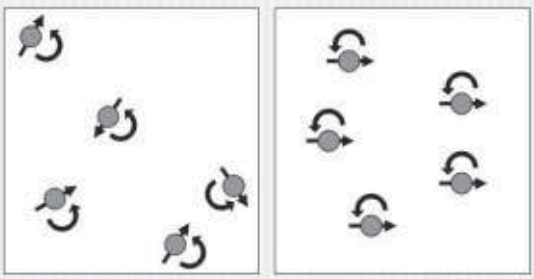

Figure 4.

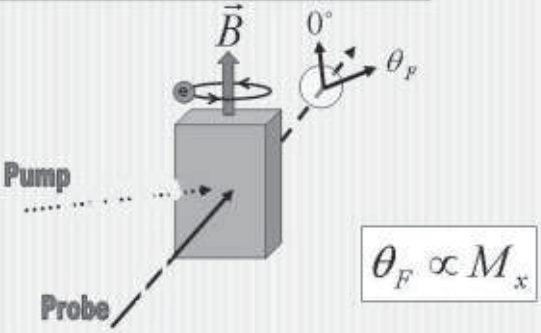

Preparation of Silicon Carbide Substrates using Hydrogen Etching for Epitaxial Growth of Nitride Heterostructures

Kelly McGroddy, Materials Science and Engineering, University of Pennsylvania
Pierre M. Petroff, Materials Department, Jay S. Brown, University of California Santa Barbara
kellymcg@seas.upenn.edu, jsbrown@engineering.ucsb.edu

Abstract:

Hydrogen etching of silicon carbide has been studied to achieve smooth surfaces for use as substrates for epitaxial growth of aluminum gallium nitride heterostructures. Atomic force microscopy shows that scratches found on commercially available silicon carbide are eliminated and atomic scale stepped surfaces are obtained. Etching is carried out on (0001) oriented 6H silicon carbide at temperatures of 1500-1700°C under 5% hydrogen, 95% argon. Obtained results depend on etching temperature and time, gas flow, and post-etch cooling rate. The steps that result are 15±2Å in height, which corresponds to the height of the 6H silicon carbide lattice in the <0001> directions. The step widths are several hundred nm.

Introduction:

Nitride heterostructures are of great technological importance due to their wide band gaps and thermal stability. These qualities make nitride heterostructures promising for optoelectronic devices such as lasers, light emitting diodes and optical storage devices.

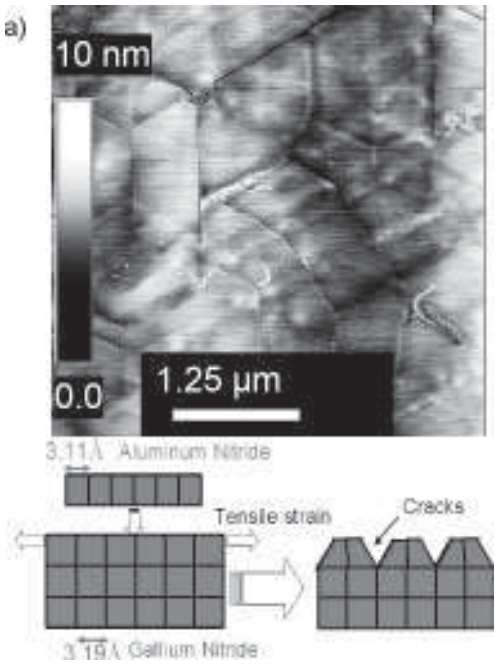

Figure 1. a) AFM of cracked AlN film. b) Epitaxial lattice mismatch.

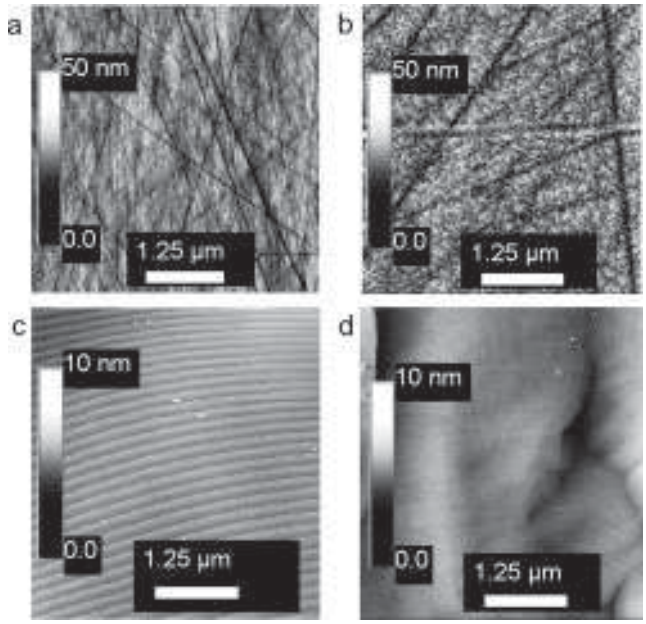

Figure 2. Comparison of SiC before (a) and after (c) etching. (b&d) AlN films on these surfaces.

Typical nitride structures are created by depositing thin layers of alternating wide and narrow band gap material, such as AlN and GaN, by molecular beam epitaxy (MBE). Films grown by MBE are built one atomic layer at a time such that the lattice structure of the substrate continues into the deposited layer. Epitaxy requires the substrate and growth materials to have similar lattice parameters in the growth plane. AlN films grown on GaN typically exhibit cracking due to the tensile strain on AlN from the 2.6% lattice mismatch between GaN and AlN (Figure 1).

SiC has been demonstrated to be a superior substrate for crack-free AlN growth because of its in-plane lattice match to AlN, which results in a 1% compressive strain in AlN. In addition, SiC is both electrically and thermally conductive making it useful for devices. SiC substrates can be purchased commercially; however, the surfaces of these substrates have large scratches and defects from polishing (Figure 2a) which results in highly defective AlN films (Figure 2b). Relatively high temperature hydrogen etching of the SiC can eliminate these scratched layers to obtain atomically smooth surfaces

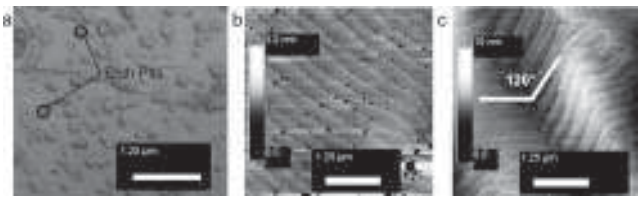

Figure 3. a) Redeposition and etch pits. b) Etch pits. c) Facets.

[1,2] (Figure 2c) on which smooth AlN films can be grown (Figure 2d). Figure 2c shows the atomic scale stepped structure that results from the energetic stability of particular lattice planes. The focus of this research is on the development of the SiC etching process to further understand the etching mechanisms.

Experimental Procedure:

CREE supplied 6H (0001) oriented SiC wafers with nominally no miscut are used [3]. Etching is carried out in an HTM tube furnace in which the gas flow through the system can be switched between purified Ar and process gas which consists of 95% Ar and 5% H_2. All samples are heated at 8°C/min to 1200°C followed by a 5°C/min ramp to the maximum etch temperature. Etch times range from 10-60 minutes at temperatures from 1575°C to 1625°C. Process gas flow rates of 5-30 SCFH are used with the gas flowing either only at the etching temperature or also during heating and/or cooling. Cooling rates vary from greater than 10°C/min (uncontrolled) to 2°C/min.

Results and Discussion:

In preliminary experiments, several detrimental features are observed. The most prevalent of these is redeposition (Figure 3a) which is reduced by increasing the gas flow and increasing the etch temperature. Redeposition is attributed to rapid post-etch cooling rates and the lack of gas flow during cooling. This most likely occurs as a result of different etching mechanisms at high and low temperatures.

We conclude that at higher temperatures, hydrogen reacts preferentially with carbon resulting in gaseous hydrocarbons and liquid silicon [4]. Upon rapid cooling, the liquid silicon crystallizes on the surface. At lower temperatures, however, hydrogen reacts with the excess silicon removing it from the surface. Therefore, to remove the silicon from the surface, the sample must be cooled slowly under flowing gas.

Etch pits (Figure 3a and 3b) are present on many samples and their density increases with increasing etch time and gas flow. Extensive faceting as shown in Figure 3c also sacrifices surface quality. High quality surfaces with no redeposition and minimal etch pits have been achieved by flowing gas at 15 SCFH above 1000°C, a maximum etch temperature of 1600°C for 10 minutes and a cooling rate of 2°C/min. Under these conditions a very smooth surface with long, straight steps is obtained (Figure 4).

The resulting step structures are typically about 15Å in height (Figure 4), the height of the 6H SiC in the [0001] direction. Most steps face toward $<10\bar{1}0>$ which corresponds to the most energetically favorable etch directions [1]. Facets are present when etching occurs on multiple planes. The facets typically form angles of 120° corresponding to the angle between planes in the $\{10\bar{1}0\}$ family (Figure 3c). The facets arise from the degree and direction of miscut. If the miscut is toward $<10\bar{1}0>$ the post-etching surface should be smoother with fewer facets since only one preferential etch direction would be exposed [1].

Conclusion:

Successful etching of SiC resulting in atomically smooth stepped surfaces has been achieved. Smooth, crack free AlN has been grown epitaxially on these surfaces with improved surface qualities. Further work is needed to determine the nature of the various etching mechanisms and the role of miscut.

References:

[1] V. Ramachandran, M.F. Brady, A.R. Smith, R.M. Feenstra, and D.W. Greve, J. of Electronic Materials 27 (4) (1997) 308.

[2] Z.Y. Xie, C.H. Wei, L.Y. Li, Q.M. Yu, J.H. Edgar, Journal of Crystal Growth 217 (2000) 115.

[3] SiC Product Specifications <http://www.cree.com/ftp/pub/sicctlg_read_new.pdf>

[4] Qizhen Xue, Q. K. Xue, Y. Hasegawa,k I. S. T. Tsong, and T. Sakurai, Applied Physics Letters 74 (17) (1999) 2468.

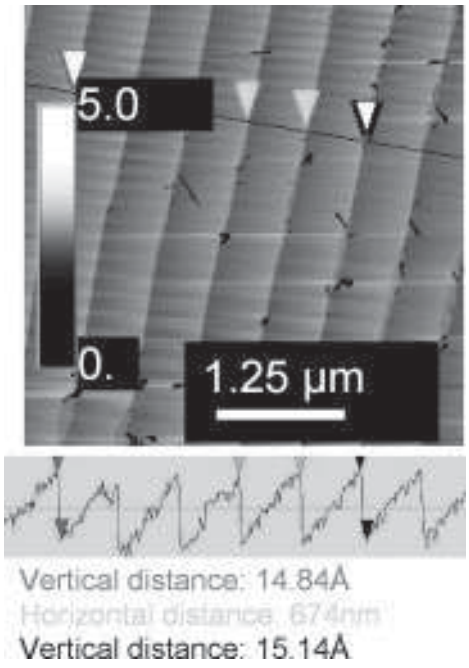

Figure 4. AFM height profile showing step height & width.

The Contribution to Refractive Index of a Functional Group Phase

Jennifer S. Park, Chemical Engineering, University of Colorado at Boulder

Dr. Jacob Israelachvili, Dr. Rafael Tadmor, Dept. of Chemical Engineering, UCSB

Jennifer.Park@colorado.edu, Jacob@engineering.ucsb.edu

Abstract:

In solvated surfactant-coated surfaces, there appears to be a discrepancy between measured and calculated van der Waals attraction, in which the measured attraction is always considerably larger than the calculated one. It has been shown in one case that the difference can be ascertained to the orderly placement of functional groups within the surfactant layer by considering a layer of identical functional groups as a distinct phase with its distinct refractive index [surface forces are a function of the r.i.].

In this study, we have devised a simple method for calculating the refractive index of any such functional group phase. The orderly arrangement of functional group is pertinent because the refractive index is also dependent on neighboring atoms. Our calculation takes this into account, and thus the same functional group may have somewhat different refractive indices for different molecules.

Introduction:

Understanding better the effect of functional groups on the refractive index could possibly explain the discrepancy between calculated and measured van der Waals forces between surfactant-coated surfaces [1].

Surface energy (() (called surface tension when referring to a liquid) is related to van der Waals interaction [2].

$$(1)\ \frac{A}{12\pi D_0^{\,2}} = 2\gamma \qquad (2)\ A \cong \frac{3h\nu_e(n_1^{\,2}-n_2^{\,2})}{16\sqrt{2}(n_1^{\,2}+n_3^{\,2})^{3/2}}$$

The representative equations are as shown where A is the Hamaker constant describing the magnitude of van der Waals attraction, D_0 is the distance of separation between two surfaces, h is Planck's constant, ν_e is frequency and n is the refractive index. Therefore we can conclude that the surface energy (γ) is related to the refractive index (n).

Method:

Essentially we treat the functional group as a separate dense phase from the rest of the molecule and calculate the refractive index of this dense functional group phase using ubiquitously catalogued, measured refractive index data. The method was tested using refractive index data of hydrocarbon chains measured at 20°C and 589 nm. This calculation may be useful in system where there are layers of functional groups such as, but not limited to: -OH, -COOH, C=O, -Br, C=C.

In order to do this, we must make a comparison of the refractive index of a hydrocarbon chain (h.c.) that contains the functional group to an h.c. chain with identical structure except that it does not contain the functional group. We cannot assume that the contribution of the functional group is merely the difference between the refractive indices of the two hydrocarbon chains previously mentioned.

For example, the contribution of an end-group -OH to refractive index of a structure composed of one -OH and a hydrocarbon chain with an infinite number of carbons, would be negligible. One must take into consideration the concentration of the functional group with respect to the rest of the molecule. The 'rest of the molecule' is defined as a phase of -CH_2-'s.

With the functional group denoted as (ϕ), the expression can be written as:

$$(3)\ \frac{n2-n1}{\left(\frac{f}{N}\right)} = n\phi$$

Equation (3) is given, where n2 is the refractive index of the hydrocarbon chain with the functional group, n1 is the refractive index of the hydrocarbon chain without the functional group, (f/N) is the ratio of the number of functional group over the total number of carbons, and nϕ is the contribution to the refractive index of a hypothetical dense phase composed just of the functional group.

The phase of -OH for which we are interested in calculating the refractive index ($n\phi$), can be symbolized by —OH —OH —OH —OH —OH —OH —OH -OH-. The phase without the -OH (n1) can be written as $CH_3CH_2CH_2CH2CH_2CH_2CH_2CH_2CH_3$, and the phase with the -OH (n2) can be written as, $CH_3CH_2CH_2CH_2CH_2CH_2CH_2CH_2CH_2$-OH, where ϕ is the -OH group. The refractive index of nonane (C_9) is 1.4050 and that of 1-nonanol is 1.4330.

If we take the difference of refractive index of nonane (n1) from nonene (n2) and divide it by (f/N) which in this case is (1/9), we obtain $n\phi = 0.252$.

In comparison, if we do the same calculation for varying lengths of carbon chains we get a near constant value. For 5, 6, 7, 8, 10, 11 carbons we get 0.255, 0.258, 0.259, 0.248, 0.26, 0.253 respectively.

The constant value shows that even for varying lengths of hydrocarbon chains, you still get the same contribution to refractive index of a functional group phase.

Conclusion:

The model proposed involves a very simple mathematical relation. The parameters needed in the equation are data that is extensively catalogued and can easily be found. The powerful benefit to our method over more mathematically complex regression analysis is that our method does not define a single, generalized value for the contribution of a functional group. Since the value of the contribution to refractive index of a functional group can change depending on its orbitallic environment, we have rather derived a relation that can be applied to any specific system.

Acknowledgments:

Thank you to Rafi Tadmor, Jacob Israelachvili, the Israelachvili group, UCSB, NNUN, my family and friends.

References:

[1] Klein, J. and Tadmor, R., J. of Colloid and Interface Science 247, 321-326 (2002)

[2] Israelachvili, J. N., "Intermolecular and Surface Forces." Academic Press, London, 1992.

[3] Born, M. and Wolf, E., "Principles of Optics", 6th Ed., Pergamon Press, Oxford, 1980.

[4] Van Krevelen, D. W. "Properties of Polymers: Their Estimation and Correlation with Chemical Structure"; Elsevier: Amsterdam, 1997.

[5] Jenekhe, S. A. and Yang, C. J., Chem. Mater. 7, 1276-1285 (1995).

The Effects of Doping on the Lateral Oxidation of AlAsSb

Kristen Van Horn, Engineering, Harvey Mudd College

James Speck, Aaron Maxwell Andrews, Materials, University of California, Santa Barbara

kristen_vanhorn@hmc.edu, speck@mrl.ucsb.edu

Abstract:

For semiconductors fabricated from III-V compounds, the oxidation interlayer is usually composed of an aluminum-containing alloy, such as aluminum arsenide antimonide (AlAsSb). However, during oxidation, antimony segregates from the AlAsSb layer and precipitates to the interfaces between the oxide and the semiconducting layers. The precipitated antimony inhibits further processing of the sample.

Testing the published theory that n-type doping of the AlAsSb layer would decrease the antimony segregation, samples of AlAsSb grown on gallium arsenide (GaAs) substrates were doped with silicon (Si) or tellurium (Te). The samples underwent wet lateral oxidation in a vapor mixture of water and methanol. The temperature of the furnace and the concentration of the water:methanol solution were varied. Optical microscopy and high resolution x-ray diffraction were used to characterize the oxidation and antimony segregation.

Results show that neither Si nor Te doping effectively suppressed antimony segregation.

Introduction:

Oxidation layers in semiconductors have multiple uses. They can act as an insulator between the semiconducting layers or can be used to create apertures for laser applications. This project, however, is concerned with laterally oxidizing the oxidation layer for use in lattice-engineered layers [1].

This concept is based on the fact that most semiconductors have a lattice mismatch with each other. When this mismatch exists between the substrate and the layers, the layers are strained during growth, either tensilely or compressively, increasing the defect density in the semiconductor, which adversely affects material quality. If an oxidation layer is grown between the substrate and compressively strained layers, lateral oxidation of the interlayers enhances relaxation of the strained layers. This allows the growth of layers, which have a large lattice mismatch with the substrate, onto the relaxed layers.

The growth of gallium antimonide (GaSb) on indium phosphide (InP) substrates is currently hindered by the large mismatch between the two lattices. Using AlAsSb as the oxidation interlayer, it was hoped that lattice-engineered layers could be created.

A barrier encountered in this research was the segregation of antimony (Sb) metal during oxidation, which precipitates at the oxidation layer interfaces. Not only is this Sb metal layer conductive which is detrimental to the semiconductor's performance, it causes deformation of the layers above it, making the surface morphology too rough for growth [2]. And due to the weak bond between the Sb layer and the oxide layer, further processing could damage the semiconductor.

A published theory claimed that doping the AlAsSb with an n-type dopant, and oxidizing with a water:methanol solution instead of pure water, would suppress the Sb segregation [3]. This project examined the effects of doping on the Sb segregation, as well as its effects on the strain relaxation of the capping layer and the oxidation rate.

Experimental Procedure:

The samples investigated in this project were fabricated using molecular beam epitaxy (MBE). They consisted of a strained InGaAs layer grown on a doped AlAsSb oxidation layer on a GaAs substrate. The n-type dopant used was either silicon (Si) or tellurium (Te). Thicknesses of the layers used were 500Å InGaAs and 500Å doped AlAsSb.

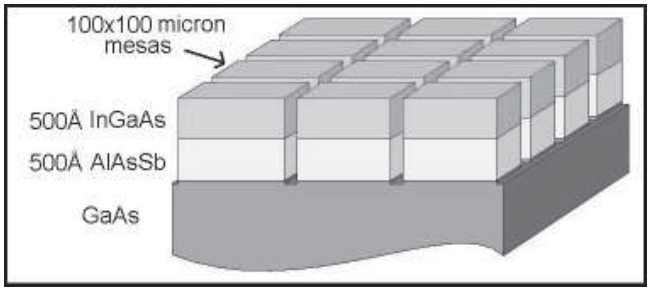

Figure 1: Heterostructure of samples with 100x100 μm etched mesas.

Photolithography and reactive ion etching were used to pattern 100 x 100 μm mesas into the surface, enabling lateral oxidation of the samples. The resulting structure is depicted in Figure 1.

The samples were oxidized in a furnace and exposed to steam generated by bubbling N_2 through a water:methanol mixture maintained at 70°C. The oxidation temperatures of 375 and 400°C were used and the oxidation time was chosen so as to partially oxidize the mesas. The water:methanol ratios tested were 1:0, 3:1, 1:1, and 1:3.

High resolution x-ray diffraction was used to determine the degree of strain relaxation in the InGaAs capping layer, and calibrated optical microscopy was used to measure the extent of oxidation and to characterize the Sb precipitation.

Results and Conclusions:

Figure 2 shows the results of lateral oxidation of the 100 x 100 μm mesas at 400°C. The dark band along the edge is the oxidized region, while the light area in the center is the unoxidized portion of the mesa. The white bumps in the oxidized region are the result of Sb precipitation at the oxide layer/capping layer interface. In both the Si-doped and Te-doped samples, the Sb segregation does not decrease with increasing methanol concentration. In fact, at higher concentrations the precipitation is worse, creating "fingers" along the surface and clumping at the edges.

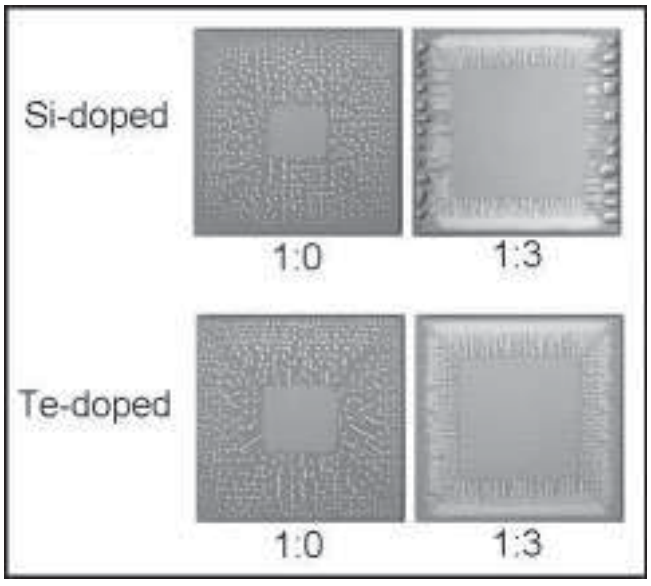

Figure 2: Top view of mesas oxidized at 400°C with 1:0 and 1:3 water:methanol ratios.

On comparison, the Te-doped samples exhibited slightly faster oxidation rates and a lesser extent of Sb precipitation than the Si-doped samples.

Results of the x-ray diffraction analysis are summarized in Table 1. These results indicate that even with the large extent of Sb precipitation, enhanced relaxation did occur in the InGaAs capping layer for both doped samples. But, given the results of the optical microscopy, the conclusion is that neither Si nor Te doping of the AlAsSb layer effectively suppresses Sb segregation during oxidation.

References:

[1] S.K. Mathis, K.H. A. Lau, A.M. Andrews, E.M. Hall et al. Lateral oxidation kinetics of AlAsSb and related alloys lattice matched to InP. J. Appl. Phys. 89, 2458 (2001)

[2] O. Blum, M.J. Hafich, J.F. Klem, K.Baucom, and A. Allerman. Wet thermal oxidation of AlAsSb against As/Sb ratio. Electronics Letters, 33, 12 (1997).

[3] A. Salesse, R. Hanfoug, Y.Rouillard, F. Genty, G. Almuneau, L. Chusseau, A. Baranov, C. Ailbert, J. Kieffer, E. Lebeau, J.M. Luck. Wet oxidation of AlAsSb alloys catalyzed by methanol. Applied Surface Science 161 (2000) 426-433.

Sample	Dopant	Ox. Temp. (°C)	Ox. Time (minutes)	Water: Methanol	Initial % Relaxation	Final % Relaxation
a	Si	375	180	3:1	80.6	93.4
b	Si	375	180	1:3	80.6	93.5
c	Te	375	180	3:1	80.4	88.6
d	Te	375	180	1:3	80.4	88.8

Table 1: Strain relaxation results from x-ray diffraction analysis.

Thank you all for a great summer!

keep in touch!

The 2002 NNUN Research Experience for Undergraduates Program

Index of Interns and Principal Investigators